Beam diffraction effects in guided-wave transmission of fluid embedded elastic plate. Influence of receiver distance and finite aperture.

by
Simen Midtbø

Master of Science
Thesis in Acoustics

Department of Physics and Technology
University of Bergen

June 2018

Preface

This thesis is a piece of a long-term research project by the acoustics group at the University of Bergen (UoB), which is the study of diffraction and dispersion effects associated with guided ultrasonic waves (GUW). The study was performed under the supervision of Per Lunde and co-supervisors Magne Aanes and Magne Vestrheim.

Thank you Per, Magne V. and Magne A., for your guidance and for your creative perspectives. Your immense knowledge and analytic minds have been greatly appreciated, and you've taught me valuable skills and given me an experience which will stand the test of time.

I would also like to give a special thanks to Magne A. for your patience when teaching me the experimental setup, and for your time spent discussing results and general relevant topics in the thesis.

Finally, a thanks to my family and friends who supported me throughout the year, and a thanks to Grunde Waag who sent me his data so I could compare with his results.

Summary

For the past decades, plate transmission effects have been extensively studied with the incentive of applying the knowledge in GUW methods in the industry. With these studies, multiple anomalous effects have been identified, such as increase of on-axis pressure after transmission, downshift of frequency compared to plane-wave theory, and narrowing of transmitted beam. These effects are associated with leaky Lamb modes when the plate is immersed with a significant fluid loading. The studies on these effects have in general been performed with a point receiver, though in applications in the industry, the receiver is always of a finite order.

An Angular Spectrum Method (ASM) model is developed for the study of plate transmission effects with a finite receiver. The model is based on a model by Anderson and Martin, who derived a plate transmission model using baffled pistons as source and receiver. They used the boundary condition that the normal particle velocity on the piston source surface is constant, and used this to derive an expression for the transmitted pressure on the surface of a finite receiver. Both of these models are compared with a third model derived by Orofino and Pedersen who developed a plate reflection model with baffled pistons as source and receiver, but with constant pressure on the piston source surface. They used this to derive an expression for the reflected normal particle velocity on the surface of a finite receiver. Their model is converted to a plate transmission case, as Waag did, and some comparisons with his work are also performed. Orofino and Pedersen/Waag excluded evanescent waves in the model, which may cause errors in the nearfield where the evanescent waves may be of an significant order. Therefore, the effect when excluding or including evanescent waves is investigated, along with the differences of boundary conditions.

The developed model is used to study the influence of finite receiver in

comparison with a point receiver, with a focus on the anomalous effects associated with leaky Lamb modes. Additionally, Waag stated that the frequency downshift is minimal when increasing the distance between the source and plate, and plate and receiver, when the distances are equal. There were not done any further inquisition to why. Therefore, the model developed is also used to investigate the effects and frequency downshift when the receiver is far from the plate, with and without finite receiver.

Contents

Chapter 1

Introduction

1.1 Background and motivation

Guided ultrasonic waves (GUW) in plate and pipelike structures have been a topic of study since the beginning of the 20th century, with Lamb [1], [2], and Rayleigh [3] introducing the dispersion equations for plates in vacuum, before Reissner [4] and Osbourne and Hart [5] developed the equations for transmission and reflection of sound interacting with plates immersed in fluid. Since then, the increasing knowledge of the effects concerning GUW have lead to the development of numerous methods that apply this knowledge in practical applications [6]. Examples include the detection of defects or cracks in structures, non-invasive measurement of flow, flow-assurance and integrity measurements (such as early detection of hydrate growth in oil and gas pipelines), material characterization, thickness and corrosion measurements of pipelines, and structural health monitoring (e.g. the monitoring of sand erosion within pipelines). With the non-invasive nature of GUW comes advantages, which include the monitoring of flow without any mechanical disturbance, the accessibility of GUW technology, i.e., a large number of transmitter and receiver technologies are available for GUW excitation, and the advantage that a single probe can be used to monitor a large area, also for hidden and coated structures, etc. However, the interaction of sound between fluids and structures are complex due to, e.g., interference effects, dispersive effects, diffraction effects, and as a consequence, the general analysis and interpretation of the behavior of sound. It therefore requires mathematical and numerical modeling tools which are able to include all aspects of propagation

and interaction of sound with structures. This often involves a model capable of calculating the generation, reflection and transmission, propagation, and the receiving of sound within a measurement system. In non-contact immersion methods, this system may consist of a source radiating towards a fluid-immersed plate with a receiver, and some of the more recent methods of modeling this system include the Gaussian beam method, e.g., [7], the Finite Element Method (FEM), e.g., [8], [9], [10], the Distributed Point Source Method (DPSM), e.g., [11], [12], and the Angular Spectrum Method (ASM), e.g., [13], [14], [15], [16], [17], [18], [19]. The Gaussian beam method approximates the sound field emitted by an uniformly vibrating planar piston mounted in a rigid baffle of infinite extent ("baffled piston model"), with a single main lobe without sidelobes. The DPSM also approximates a baffled piston generated sound field, but with a piston surface consisting of many point sources vibrating in phase. The sound field created by the superposition of the point sources is then used as an approximation of the sound field. This method agrees with analytically calculated theory in the farfield, but there are discrepancies in the nearfield [20]. The FEM can take a real transducer into account, characterized by means of material constants and dimensions. It can then simulate the real generated pressure and many of the parameters associated with the transducer, thus give a quantitative description of the measurement system. However, this approach is computationally demanding and therefore not necessarily ideal for parametric studies and generic analysis. The ASM decomposes the sound field emitted by the transmitter into infinitely many plane waves. This allows for plane-wave theory to be applied, i.e., the use of plane-wave transmission/reflection coefficient for the plate, and propagation with a plane-wave phase-shift from one distance to another. The transmitter is usually approximated by a circular baffled piston, e.g. [14], [15], [18], [19], [21], and the method include sidelobes and nearfield generated by the baffled piston.

With the study of plate transmission and reflection, several deviations from plane-wave theory, i.e., diffraction and dispersion phenomena, have been observed and studied when a normally incident beam interacts with a plate, [13], [18], [19], [22], [23], [24], [25], [26], [27], [28], [29]. In 1982, Johnson and Devaney [13] studied reflections from a plate, with a distance of 60 mm between the plate and receiver, and discovered that the frequency of maximum reflection deviated from plane-wave theory. They modeled their system using ASM with a finite receiver and predicted the frequency downshift, which they compared

with measurements. In 2003 Holland and Chimenti [22] reported of a Lamb wave resonance that had a unusual efficient transmission of airborne waves. This occurred at the zero group velocity (ZGV) when exciting the thickness-extensional (TE) symmetric Lamb mode in the plate. They argued that this was due to diffraction of the incident wave, which can be approximated as infinitely many plane waves with individual incident angles, which therefore has the potential to excite the same Lamb mode at different angles. They also stated that at the ZGV-point, the Lamb waves does not propagate in the plane of the plate, but radiates back into the air. In 2005, Gibson and Popovics [23] used the FEM to link an empirically determined correction factor, which had been used to correct for the mentioned frequency downshift in impact echo (IE) methods, to the ZGV mode of the symmetrical TE Lamb mode. They compared the results with measurements with good agreement.

Similar effects have also been discovered with the studies of a plate immersed in water, i.e., effects associated with leaky Lamb modes. These effects include a frequency downshift in comparison with plane wave theory, an increase of on-axis transmitted pressure, and a narrowing of the transmitted beam. In 2008, Lohne et al. [24] identified these three effects with measurements. In 2011 [18], Lohne et al. developed an ASM model based on a farfield solution [30] of the baffled piston model, which confirmed the measurements done in 2008. These simulations were performed with a point receiver positioned 100 mm from the plate, with the plate in the farfield of the transmitter. In 2014, Aanes [21] developed two models based on the FEM and ASM method (FEM approach and Hybrid FEM-ASM approach). These two models incorporate the transducer into the simulations allowing for more realistic beam battern to interact with the plate, which enabled a quantitative system description. These methods along with measurements, confirmed the dispersion and diffraction phenomena observed by Lohne et al. In 2015 Aanes et al. [25], [26], used the methods to show a correlation between the effects and a leaky Lamb mode with negative group velocity (NGV). It was also shown that with the excitation of a leaky Lamb mode having positive group velocity (PGV), there were no or only subtle frequency shifts, decrease of on-axis pressure after transmission, and widening of the transmitted beam. The dependence of the Poission's ratio on these effects were also studied. In 2016 and 2017, Aanes et al. [27], [28] showed that at the frequency of increased transmitted pressure, the transmitted pressure does not

decay as 1/distance, when the incident wave do. They also proposed that the narrowing of beam and increase of pressure was due to the phenomenon of opposite signs on the phase velocity and group velocity ("backward wave propagation" [31]). In the same year, Waag [19] used a model based on a model by Orofino and Pedersen [14], with a finite receiver for the study of plate transmission. This model was used to study, e.g., the frequency downshift phenomenon and its dependence on the Poisson's ratio of the plate, and its dependence of the distances between the source and plate, and the plate and receiver, which was set equal. It was found that when this distance is large relative to the Rayleigh-distance, the frequency downshift effect is minimal. It was however not done any further investigations to why the frequency shift is minimal with increasing distance, and it is also not clear whether it is the distance between source and plate or between plate and receiver that is the determining factor of the minimal frequency shift. Glushkov et al. [29] also did some work on these effects in 2017 and compared with the work by Aanes et al. They built a semi-analytical model to study the effects, and also studied some of the energy propagation and flux in the plate itself, along with dispersion analysis.

Even though these effects have been studied both for a point and finite receiver for negligible fluid loading, they have not been extensively addressed for a finite receiver when leakage is significant. In GUW applications in the industry, the receiver is always finite. Waag did some work on this, and it was mentioned that he studied the frequency downshift with a model based on Orofino and Pedersen. The model by Orofino and Pedersen is based on ASM using a baffled piston model for the transmitter and receiver, which are limited to having the same radius, for plate reflection studies. They used the boundary condition of constant pressure on the surface of the piston, and then solved for the received normal particle velocity. Waag used their model for transmission analysis instead of reflection. Another study using a finite receiver and plate, were done by Anderson and Martin [15] in 1995. They derived a model based on ASM, similar to Orofino and Pedersen, but focused on transmission studies. Unlike Orofino and Pedersen however, Anderson and Martin used a boundary condition with constant velocity on the surface of the piston source, and solved for the pressure at the finite receiver. In addition to the different boundary conditions between the two models, there are also differences in factors and coordinate systems. Additionally, the models of Orofino and Pedersen, and subsequently Waag, does not consider evanescent waves, which may

introduce errors in the nearfield of the baffled piston source, where the evanescent waves may be of an significant order.

1.2 Objective

The objective of the present work is to study and investigate diffraction and dispersion effects observed in plate transmission and with the excitation of backward wave leaky Lamb modes. The work will focus on these effects when using a finite receiver when the plate is significantly fluid loaded.

To keep the study at a generic level, a model based on the ASM will be developed where the transmitter and receiver are modeled as baffled pistons. It will be based on the model by Anderson and Martin, and is to be compared with their model and the model used by Waag, which was based on the model by Orofino and Pedersen, and will therefore be referred to as Orofino and Pedersen/Waag. The sound field generated by the models, without plate present, will also be compared with baffled piston source models that are independent of the ASM for further validation. Additionally, the validity of the constant pressure and constant velocity boundary conditions, the exclusion or inclusion of evanescent waves, and significance of differences in factors, are also to be investigated.

The dispersion and diffraction effects in plate transmission will be studied using a finite receiver and highlighted by comparisons with a point receiver. Further investigations of the effects and their distance dependency between the plate and receiver, both with and without finite receiver, will also be executed.

1.3 Outline of thesis

In Ch. 2, the three models of interest throughout the thesis are derived and explained. Then some ASM independent models are presented, followed by other preliminary definitions and theory required for the results presented in the thesis.

In Ch. 3, the simulation setups are reviewed for each of the three models. Some simulation challenges and how they were solved and

handled, are also explained.

In Ch. 4, the measurement setup is explained, along with the measurement methods and post-processing of data.

In Ch. 5, the three models are compared against each other and other models, with and without plate, along with some discussion concerning the potential differences between the simulation results. Then the influence of a finite receiver is discussed, by comparing with the case of a point receiver, with and without plate.

In Ch. 6, the simulation results of the transmitted pressure using the model developed for the thesis as a function of distance and frequency are presented. The observed phenomena are discussed.

In Ch. 7, conclusion of the results are given. Further work relevant to the observed results are also proposed.

In Appendix A, Appendix B, Appendix C, the code for the implementation of models are given. In Appendix D, Appendix E, Appendix F, Appendix G, Appendix H and Appendix I, the codes of the additional routines used within the simulation programs are given.

Chapter 2

Theory

This chapter introduces the theory of the three models, along with supplementary theory. In Sec. 2.1., the derivation of the developed model is presented, which is labeled as model 1. Following this, in Sec. 2.2., model 2, the model given by Anderson and Martin, is presented, but only the major steps of the derivation will be shown and the mathematical differences with model 1 will be highlighted. In Sec. 2.3., Orofino and Pedersen/Waags model, model 3, is presented, and again only the major steps will be shown with highlighting the mathematical differences with model 1. In Sec. 2.4., two ASM independent models which represent the pressure without plate, with and without finite receiver, are given. In Sec. 2.5., the required theory to understand the mathematical difference between propagating and evanescent waves is presented, followed by the definition of the plane-wave transmission coefficient in Sec. 2.6., where the dispersion equations given by Osbourne and Hart [5] are also presented. In Sec. 2.7., some transfer functions used to study transmission effects are defined. Finally, in Sec. 2.8., the method of introducing losses in fluid is explained.

2.1 Model 1

The system is in the cylindrical coordinate system (r, z) where r represent the radial direction, and z represents the vertical direction. A uniformly vibrating planar circular piston source centered in $r = z = 0$ in a rigid baffle of infinite extent is radiating normally towards an elastic plate with thickness d, and interacts with the plate at a distance

$z = d_T$, creating guided waves in the plate, which reradiates into the fluid at the lower side of the plate. The transmitted pressure is received at a distance $z = d_T + d_R$ with a baffled piston of radius b centered in $r = 0$. Both the piston source and piston receiver are axisymmetric around the z-axis. Constant and uniform velocity v_0 on the surface of the piston source is assumed. The plate is also assumed to be of infinite extent in the radial direction, and the surfaces of the piston source, plate, and piston receiver are aligned perfectly perpendicular with the z-axis and is thus parallel with each other. The system is also assumed to be lossless. See Fig. 2.1. for an illustration of the system.

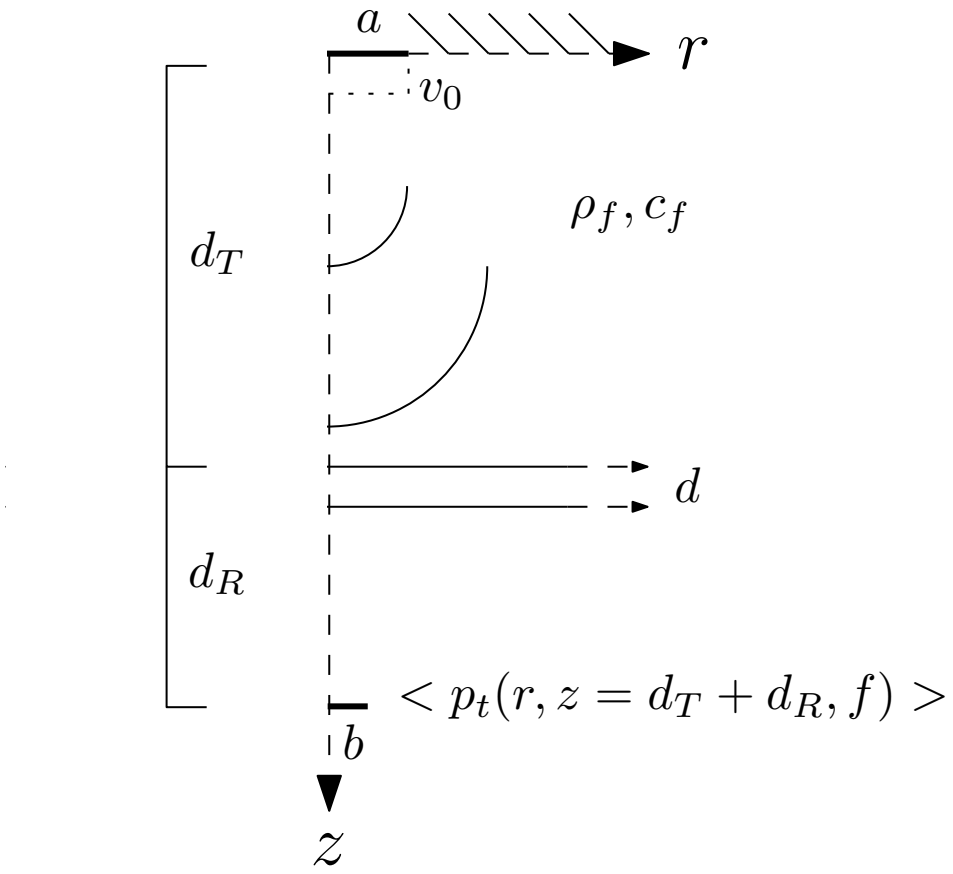

Figure 2.1: The case of model 1, where a piston source, plate and piston receiver are immersed in a fluid, in the cylindrical coordinate system.

The variables ρ_f, c_f are the fluid density and sound velocity of the fluid, respectively.

To decompose a function $v_z(r,z)$ that represents the normal particle velocity (z-direction) into a plane-wave representation, a Hankel transform/Fourier-Bessel transform is required [33], and in a arbitrary plane z with time convention $e^{-i\omega t}$ where $\omega = 2\pi f$ is the angular frequency, this is given as [32]

$$V_Z(\eta, z, f) = 2\,\pi \int_0^\infty v_z(r, z, f) J_0(\eta r)\, r\, dr, \tag{2.1}$$

where J_0 is the zeroth order Bessel function, and $V_Z(\eta, z, f)$ is the angular spectrum, or decomposed normal particle velocity, which is characterized by its wavenumber-dependence, i.e. the function is in the wavenumber-space (k-space [33]). The field variables in wavenumber-space will always be represented with capital letters. η is the horizontal wavenumber.

The boundary conditions at the surface of the baffled piston source are [30]

$$v_z(r, z=0, f) = \begin{cases} v_0, & r \leq a \\ 0, & r > a \end{cases} \tag{2.2}$$

With a constant velocity, $v_z(r, z = 0, f) = v_0$, so the decomposed normal particle velocity on the piston-source surface is given by [32]

$$V_Z(\eta, z=0, f) = V_Z(\eta, f) = 2\,\pi v_0 \int_0^a J_0(\eta r)\, r\, dr, \tag{2.3}$$

which gives a known integral identity [34][p. 484, eq. 11.3.20.], [32],

$$V_Z(\eta, f) = 2\,\pi v_0 \frac{1}{\eta^2} \int_0^{a\eta} J_0(x) x dx = 2\,\pi v_0 \frac{a}{\eta}\, J_1(a\eta), \tag{2.4}$$

where J_1 is the first order Bessel function. This gives the decomposed plane-wave, normal particle velocity on the piston source surface, also known as the source aperture function, as [32], [15]

$$V_Z(\eta, f) = \pi a^2 v_0 \frac{2J_1(a\eta)}{a\eta}, \tag{2.5}$$

where the fraction $2J_1(a\eta)/a\eta$ is the directivity function or Jinc function. This has the property that

$$\lim_{x \to 0} \frac{2J_1(x)}{x} = 1, \tag{2.6}$$

which will be used later.

The field-variable of interest is the pressure, so the decomposed normal particle velocity needs to be converted to pressure. This can be done using Euler's equation [30][p. 119, Eq. 5.4.10.]. In the time-domain, Euler's equation is

$$\rho_f \, \vec{v}(r, z, t) = -\nabla p(r, z, t). \tag{2.7}$$

Using a Fourier-transform to convert Eq. (2.7) into the frequency domain, the velocity and pressure are proportional to $e^{-i\omega t}$, so Eq. (2.7) becomes

$$i\omega \, \rho_f \, \vec{v}(r, z, f) = \nabla p(r, z, f). \tag{2.8}$$

The particle velocity of interest on the piston-surface is the normal component of the velocity, i.e., the velocity in the z-direction, so Eq. (2.8) reduces to [33]

$$i\omega \, \rho_f \, v_z(r, z, f) = \frac{\partial p(r, z, f)}{\partial z}. \tag{2.9}$$

This equation is then converted to wavenumber-space by doing a spatial Hankel transformation with respect to r of the spatial functions [33]

$$i\omega \, \rho_f \, 2\pi \int_0^\infty v_z(r, z, f) \, r \, dr = 2\pi \int_0^\infty \frac{\partial p(r, z, f)}{\partial z} \, r \, dr, \tag{2.10}$$

$$i\omega \, \rho_f \, V_Z(\eta, z, f) = \frac{\partial P(\eta, z, f)}{\partial z}. \tag{2.11}$$

In the wavenumber-domain, the pressure at a distance z can be calculated by using wave field extrapolation [33]. This is done by extrapolating the plane-wave pressure in a plane at some distance z' to another plane at a distance z, using a simple plane-wave phase change as $e^{ih_{f,z}(z-z')}$ where $h_{f,z}$ is the vertical wavenumber and is given as

$$h_{f,z} = \begin{cases} \sqrt{h_f^2 - \eta^2}, & \eta \leq h_f \\ i\sqrt{\eta^2 - h_f^2}, & \eta > h_f \end{cases} \tag{2.12}$$

where h_f is the magnitude of the directional wavenumber in the fluid, and $\eta \leq h_f$ represent propagating waves, while $\eta > h_f$ represent evanescent waves [33]. More on this in Sec. 2.5. If the initial distance is $z' = 0$, the calculation of the pressure at a distance z is given as

$$P(\eta, z, f) = P(\eta, z' = 0, f) \cdot e^{ih_{f,z}(z-z')} = P(\eta, f) \cdot e^{ih_{f,z}z}. \tag{2.13}$$

This means that with $P(\eta, z, f) \propto e^{ih_{f,z}z}$ the final relationship between the particle velocity and pressure in wavenumber-space at the surface of the piston is, [33], [15]

$$i\omega\,\rho_f\,V_Z(\eta, z, f) = ih_{f,z}P(\eta, z, f), \tag{2.14}$$

$$P(\eta, z, f) = \frac{\rho_f\omega}{h_{f,z}}\,V_Z(\eta, z' = 0, f)\,e^{ih_{f,z}z} \tag{2.15}$$

$$P(\eta, z, f) = \frac{\rho_f\omega}{h_{f,z}}\,V_Z(\eta, f)\,e^{ih_{f,z}z}, \tag{2.16}$$

which represents the angular spectrum of pressure, where the fraction $\rho_f\omega/h_{f,z}$ represents the impedance of the fluid in the z-direction. The equation is not valid for $\eta = h_f$, because of the denominator in the impedance term, $h_{f,z}$, which would then become 0, and give a singularity. In simulations this is solved with an approximation by sampling very closely to this point, excluding the point $\eta = h_f$, see Sec. 3. Doing an inverse Hankel transform of Eq. (2.16) gives the spatial pressure (free-field pressure) as [32]

$$p(r, z, f) = \frac{1}{2\pi}\int_0^\infty P(\eta, z, f)\,J_0(\eta r)\,\eta\,d\eta. \tag{2.17}$$

Including a plate can be done by using the angular spectrum, Eq. (2.16), as the incident pressure $P(\eta, z, f) = P_I(\eta, z = d_T, f)$ onto the upper side of plate. This can be inserted into the plane-wave definition of the transmission coefficient, as [30]

$$T(\eta, d, f) = \frac{P_T(\eta, z = d_T + d, f)}{P_I(\eta, z = d_T, f)}. \tag{2.18}$$

The expression of the transmission coefficient is given in Sec. 2.6. The transmitted plane-wave pressure on the surface at the lower side of the plate is then

$$P_T(\eta, z = d_T + d, f) = P_I(\eta, z = d_T, f)\,T(\eta, d, f). \tag{2.19}$$

Inserting Eq. (2.16) as $P_I(\eta, z = d_T, f)$, the transmitted angular spectrum of the pressure becomes [15]

$$P_T(\eta, z = d_T + d, f) = \frac{\rho_f\omega}{h_{f,z}}\,V_Z(\eta, f)\,T(\eta, d, f)\,e^{ih_{f,z}d_T}, \tag{2.20}$$

where the transmission coefficient handles the phase change in the propagation trough the plate, so the plate thickness d needs to be subtracted

in the propagation term [15]. Using wavefield extrapolation, the plane-wave pressure can be propagated to a distance $z = d_T + d_R$, which is done by multiplying with $e^{ih_{f,z}(d_R-d)}$. The angular spectrum of the transmitted the pressure at a distance $z = d_T + d_R$ from the source is then [15]

$$P_T(\eta, z = d_T + d_R, f) = \frac{\rho_f \omega}{h_{f,z}} V_Z(\eta, f)\, T(\eta, d, f)\, e^{ih_{f,z}(d_T+d_R-d)}. \quad (2.21)$$

Doing an inverse Hankel transform to get the free-field pressure in spatial coordinates is done as [32]

$$p_t(r, z = d_T + d_R, f) = \frac{1}{2\pi} \int_0^\infty P_T(\eta, z = d_T + d_R, f)\, J_0(\eta r)\, \eta\, d\eta. \quad (2.22)$$

To introduce a finite receiver, the spatial transmitted pressure, Eq. (2.22), is averaged over the finite receiver with radius b [15]. This is done as [15]

$$< p_t(r, z = d_T + d_R, f) >= \frac{1}{\pi b^2} \int_A p_t(r, z = d_T + d_R, f)\, dA, \quad (2.23)$$

$$= \frac{1}{\pi b^2} \int_A \frac{1}{2\pi} \int_0^\infty P_T(\eta, z = d_T + d_R, f)\, J_0(\eta r)\, \eta\, d\eta\, dA. \quad (2.24)$$

The only term that is dependent of spatial coordinates and needs to be integrated, is the zeroth order Bessel function [15], so Eq. (2.23) becomes

$$< p_t(r, z = d_T + d_R, f) >= \frac{1}{\pi b^2} \frac{1}{2\pi} \int_0^\infty P_T(\eta, z = d_T + d_R, f) \quad (2.25)$$

$$\times \int_A J_0(\eta r)\, dA\, \eta\, d\eta,$$

$$= \frac{1}{\pi b^2} \frac{1}{2\pi} \int_0^\infty P_T(\eta, z = d_T + d_R, f)$$

$$\times \int_0^{2\pi} \int_0^b J_0(\eta r)\, r\, dr\, d\psi\, \eta\, d\eta, \quad (2.26)$$

where ψ is the angle of r in the plane of the receiver. Having circular

symmetry, the integral becomes [32]

$$< p_t(r, z = d_T + d_R, f) >= \frac{1}{\pi b^2}\frac{1}{2\pi}\int_0^\infty P_T(\eta, z = d_T + d_R, f) \times 2\pi \int_0^b J_0(\eta r)\, r\, dr\, \eta\, d\eta, \tag{2.27}$$

where the last term was shown in the derivation of Eq. (2.4) to have a known solution, which gives the receiver aperture function defined as $H(\eta, f)$

$$H(\eta, f) = \pi b^2 \frac{2J_1(b\eta)}{b\eta}. \tag{2.28}$$

The average pressure at the finite receiver is then given as

$$< p_t(r, z = d_T+d_R, f) >= \frac{1}{\pi b^2}\frac{1}{2\pi}\int_0^\infty P_T(\eta, z = d_T+d_R, f)\, H(\eta, f)\, \eta\, d\eta. \tag{2.29}$$

The expression is independent of r so it is unnecessary to keep it, but will be kept to follow the convention used in [15].

Note: with the property of the directivity function, given in Eq. (2.6), the expression with a finite receiver, Eq. (2.29), can be shown to be equal to the equation of a point receiver, Eq. (2.22) with $r = 0$. The term $1/\pi b^2$ in Eq. (2.29) can be multiplied with the πb^2 in the receiver aperture function $H(\eta, f)$, while letting the receiver radius go to zero as

$$\lim_{b\to 0} \frac{2J_1(b\eta)}{b\eta} = 1. \tag{2.30}$$

Eq. (2.29) becomes

$$< p_t(r, z = d_T + d_R, f) >= \frac{1}{2\pi}\int_0^\infty P_T(\eta, z = d_T + d_R, f)\, \eta\, d\eta \tag{2.31}$$

which is exactly equal to Eq. (2.22) if $r = 0$ because $J_0(0) = 1$, i.e., it represents the on-axis pressure with a point receiver. This property will be used in later sections where appropriate.

The derivations of Anderson and Martins model, and Orofino and Pedersen/Waags model, will be done by referring to the derivation of Eq. (2.29), and the important differences will be highlighted.

2.2 Model 2: Anderson and Martin

Different to model 1, Anderson and Martin [15] derived a model in a Cartesian coordinate system, and set the radius of the source equal to that of the receiver. The case is illustrated in Fig. 2.2.: a baffled circular piston source with radius a centered at $x = y = z = 0$ is radiating towards a plate with thickness d, positioned in front of a receiver with radius a at distance $z = d_T + d_R$. The plate is perpendicular to the z-axis, while the x- and y-axis are parallel to the plate, and the baffled pistons have axial symmetry around the z-axis. The y-axis points out of the page. The piston source, plate, and piston receiver are parallel with each other, and the case is also lossless.

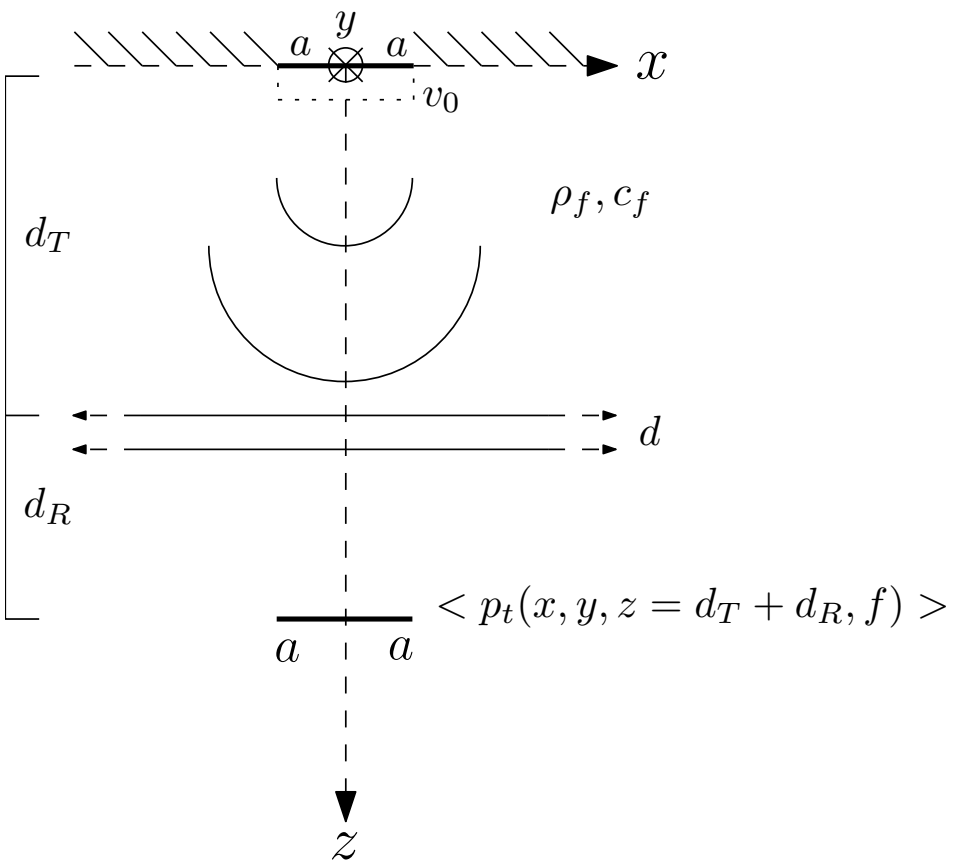

Figure 2.2: The case of model 2, which is in a Cartesian coordinate system with equal radius on the piston source and receiver.

With the notational conventions used in Sec. 2.1., with the inclusion

of a subscript A to denote Anderson and Martin, their expression in the article, [15][p. 2633, Eq. 19.], is given as

$$< p_t(x, y, z = d_T + d_R, f) >= \frac{1}{4\pi^2} \int_{-\infty}^{\infty} \int_{-\infty}^{\infty} P_A(h_{f,x}, h_{f,y}, z, f) \times H_A(h_{f,x}, h_{f,y}, f)\, dh_{f,x}\, dh_{f,y}, \tag{2.32}$$

with

$$P_A(h_{f,x}, h_{f,y}, z, f) = \frac{\rho_f \omega}{h_{f,z}} H_A(h_{f,x}, h_{f,y}, f)\, T(h_{f,x}, h_{f,y}, d, f)\, e^{ih_{f,z}(d_T + d_R - d)}, \tag{2.33}$$

and

$$H_A(h_{f,x}, h_{f,y}, f) = \pi a^2 v_0 \frac{J_1(a\sqrt{h_{f,x}^2 + h_{f,y}^2})}{a\sqrt{h_{f,x}^2 + h_{f,y}^2}}. \tag{2.34}$$

The independent variables $h_{f,x}$ and $h_{f,y}$ represent the horizontal wavenumbers in the x- and y-direction, respectively. The vertical wavenumber $h_{f,z}$ is now given as [15]

$$h_{f,z} = \begin{cases} \sqrt{h_f^2 - (h_{f,x}^2 + h_{f,y}^2)}, & h_{f,x}^2 + h_{f,y}^2 \leq h_f^2 \\ i\sqrt{(h_{f,x}^2 + h_{f,y}^2) - h_f^2}, & h_{f,x}^2 + h_{f,y}^2 > h_f^2 \end{cases} \tag{2.35}$$

The expression is otherwise similar to the expression in Sec. 2.1., Eq. (2.29), though in Cartesian coordinates. The introduction of the fluid impedance term, transmission coefficient and propagation is done very similar to that of model 1, but Anderson and Martin set the source- and receiver aperture functions equal, denoted with H_A. In model 1 this is equivalent to the source aperture function $V_Z(\eta)$ and receiver aperture function $H(\eta)$. Independent of radius of the source and receiver and coordinate system, these functions are not equal because of the constant v_0 in the source aperture function. Additionally, the factor 2 is missing from their aperture functions. The derivations of these two functions are shown in Sec. 2.1., though for cylindrical coordinates. It is not clear how Anderson and Martin did this in Cartesian coordinates. One method may be to derive the expression using cylindrical coordinates, and then convert back to Cartesian by the relation [32]

$$\eta = \sqrt{h_{f,x}^2 + h_{f,y}^2}, \tag{2.36}$$

which will be shown in the following, with a derivation independent of Anderson and Martins method. The conditions on the piston surface in Cartesian coordinates with constant normal particle velocity is given as

$$v(x, y, z = 0, f) = \begin{cases} v_0, & \sqrt{x^2 + y^2} \leq a \\ 0, & \sqrt{x^2 + y^2} > a \end{cases} \tag{2.37}$$

The angular spectrum of the normal particle velocity on the piston surface can be found using a two-dimensional Fourier transform as [33]

$$V_Z(h_{f,x}, h_{f,y}, f) = \int_{-\sqrt{a^2-x^2}}^{\sqrt{a^2-x^2}} \int_{-a}^{a} v(x, y, f)\, e^{-i(h_{f,x}x + h_{f,y}y)}\, dx\, dy. \tag{2.38}$$

If the velocity is constant, it becomes independent of the integral [32]

$$V_Z(h_{f,x}, h_{f,y}, f) = v_0 \int_{-\sqrt{a^2-x^2}}^{\sqrt{a^2-x^2}} \int_{-a}^{a} e^{-i(h_{f,x}x + h_{f,y}y)}\, dx\, dy. \tag{2.39}$$

The exponent can be written as the dot product of two vectors, and the integrand variables change accordingly [32]

$$V_Z(\vec{\eta}, f) = v_0 \int_{-\sqrt{a^2-x^2}}^{\sqrt{a^2-x^2}} \int_{-a}^{a} e^{-i\vec{\eta}\cdot\vec{r}}\, d\vec{r}, \tag{2.40}$$

where $\vec{r} = (x, y)$ and $\vec{\eta} = (h_{f,x}, h_{f,y})$. Using the geometric version of the dot product and changing the integration variables with respect to cylindrical coordinates, Eq. (2.40) now turns to [32]

$$V_Z(\vec{\eta}, z, f) = v_0 \int_0^{2\pi} \int_0^{a} e^{-i|\vec{\eta}||\vec{r}|cos\psi}\, r\, dr\, d\psi, \tag{2.41}$$

where $|\vec{r}| = r = \sqrt{x^2 + y^2}$ and $|\vec{\eta}| = \eta = \sqrt{h_{f,x}^2 + h_{f,y}^2}$, and ψ represents the angle of r in the receiver plane. Furthermore, by changing the integral order as [32]

$$V_Z(\eta, z, f) = v_0 \int_0^{a} \Big(\int_0^{2\,\pi} e^{-i\,\eta\, r\, \cos\psi}\, d\psi \Big)\, r\, dr, \tag{2.42}$$

it reveals a known solution on the integral inside the parenthesis [30][p. 512], [32], which is given as

$$\int_0^{2\,\pi} e^{-i\,\eta\, r\, \cos\psi}\, d\psi = 2\pi J_0(-\eta r) = 2\pi J_0(\eta r). \tag{2.43}$$

The resulting expression is then

$$V_Z(\eta, f) = 2\pi v_0 \int_0^a J_0(\eta r)\, r\, dr \tag{2.44}$$

This integral has a known solution, which was shown in the derivation of Eq. (2.4), so

$$V_Z(\eta, f) = 2\,\pi v_0 \frac{1}{\eta^2} \int_0^{a\eta} J_0(x) x dx = 2\,\pi v_0 \frac{a}{\eta}\, J_1(a\eta) = \pi a^2 v_0 \frac{2J_1(a\eta)}{a\eta} \tag{2.45}$$

The decomposed velocity on the piston surface with a two-dimensional description of the wavenumbers using $\eta = \sqrt{h_{f,x}^2 + h_{f,y}^2}$, can then be written as

$$V_Z(h_{f,x}, h_{f,y}, f) = \pi a^2 v_0 \frac{2J_1(a\sqrt{h_{f,x}^2 + h_{f,y}^2})}{a\sqrt{h_{f,x}^2 + h_{f,y}^2}} \tag{2.46}$$

By using the pressure and particle velocity relationship, Eq. (2.14), the decomposed particle velocity is converted to pressure and propagated to the distance $z = d_T$. Then by introducing the transmission coefficient, propagating the pressure to a distance $z = d_T + d_R$, and doing an inverse two-dimensional Fourier transform, the expression of the free-field transmitted pressure becomes

$$p_t(x, y, z = d_T + d_R, f) = \frac{1}{4\pi^2} \int_{-\infty}^{\infty} \int_{-\infty}^{\infty} P_T(h_{f,x}, h_{f,y}, z = d_T + d_R, f) \times e^{i(h_{f,x}x + h_{f,y}y)}\, dh_{f,x}\, dh_{f,y}, \tag{2.47}$$

where the angular spectrum is given as

$$P_T(h_{f,x}, h_{f,y}, z = d_T + d_R, f) = \frac{\rho_f \omega}{h_{f,z}} V_Z(h_{f,x}, h_{f,y}, f) T(h_{f,x}, h_{f,y}, d, f) e^{ih_{f,z}(d_T + d_R - d)}. \tag{2.48}$$

Averaging Eq. (2.47) over a finite receiver with radius a as in the same

way as in Sec. 2.1., which becomes

$$< p_t(x,y,z=d_T+d_R,f) >= \frac{1}{\pi a^2}\int_A p_t(x,y,z=d_T+d_R,f)\,dA \tag{2.49}$$

$$= \frac{1}{\pi a^2}\int_A \frac{1}{4\pi^2}\int_{-\infty}^{\infty}\int_{-\infty}^{\infty} P_T(h_{f,x},h_{f,y},z=d_T+d_R,f) \times e^{i(h_{f,x}x+h_{f,y}y)}\,dh_{f,x}\,dh_{f,y}\,dA \tag{2.50}$$

The only term that is dependent on the spatial integral and needs to be integrated over the surface, is the complex exponential function $e^{i(h_{f,x}x+h_{f,y}y)}$ so Eq. 2.50 becomes

$$< p_t(x,y,z=d_T+d_R,f) >= \frac{1}{\pi a^2}\int_A \frac{1}{4\pi^2}\int_{-\infty}^{\infty}\int_{-\infty}^{\infty} P_T(h_{f,x},h_{f,y},z=d_T+d_R,f) \times \int_A e^{i(h_{f,x}x+h_{f,y}y)}\,dA\,dh_{f,x}\,dh_{f,y}. \tag{2.51}$$

The last integral in Eq. (2.51) is similar to the integral that lead to Eq. (2.46), and thus will give the receiver aperture function as

$$\int_A e^{i(h_{f,x}x+h_{f,y}y)}\,dA = H(h_{f,x},h_{f,y},f) = \pi a^2 \frac{2J_1(a\sqrt{h_{f,x}^2+h_{f,y}^2})}{a\sqrt{h_{f,x}^2+h_{f,y}^2}}. \tag{2.52}$$

However Anderson and Martin states that

$$\int_A e^{i(h_{f,x}x+h_{f,y}y)}\,dA = V_Z(h_{f,x},h_{f,y},f), \tag{2.53}$$

i.e., that it is equal to the source aperture function in Eq. (2.46), which is not true. The claim is correct if dividing by v_0 as

$$\int_A e^{i(h_{f,x}x+h_{f,y}y)}\,dA = \pi a^2 \frac{2J_1(a\sqrt{h_{f,x}^2+h_{f,y}^2})}{a\sqrt{h_{f,x}^2+h_{f,y}^2}} = V_Z(h_{f,x},h_{f,y},f)/v_0. \tag{2.54}$$

The derivation done is meant to serve as a justification of the allegation that setting the aperture functions equal is not correct, and that the factor 2 should be included in the aperture functions. It also appears

that they neglected the factor $1/\pi a^2$ that comes with the averaging, so the total factor missing in their expression is calculated to be $4/\pi v_0 a^2$. In Sec. 5.2., it is shown that the inclusion of this factor is correct when comparing with an ASM independent model. For the results in the thesis, their expression, Eq. (2.32), will be used in simulations as it is given in their article.

2.3 Model 3: Orofino and Pedersen/Waag

Different to model 1 and model 3, Orofino and Pedersen (and subsequently Waag), used a constant pressure on the source piston surface as a boundary condition, and derived an expression for the normal particle velocity on the receiver surface. Their expression will be used for a case of transmission instead of reflection, which was also done by Waag. This is done by replacing their reflection coefficient with a transmission coefficient. They also used the same distance between the source-plate and plate-receiver, but this will be replaced with the distance used with model 1 and 2, i.e., $z = d_T + d_R$.

The case of transmission is shown in Fig. 2.3. A baffled circular piston source with constant pressure p_0s on the surface of the piston with a radius a centered at $r = z = 0$ is radiating towards a plate with thickness d, where the transmitted normal particle velocity is received by a receiver with radius a at position $z = d_T + d_R$. The coordinate system is cylindrical, with the plate perpendicular to the z-direction, with the r-axis as shown in the figure, and the baffled pistons have axial symmetry around the z-axis. The source, plate, and receiver are assumed to be perfectly parallel, and the case is lossless. The original expression that Orofino and Pedersen gives is [14][p. 1245, Eq. 29.]

$$V(\omega) = 2\pi \int_0^{\pi/2} \frac{\cos\theta_f}{\rho_f c_f} \left(\frac{2J_1(h_f a \sin\theta_f)}{h_f a \sin\theta_f} \right)^2 R(\theta_f, \omega)\, e^{ih_f 2w_0 \cos\theta_f} \times h_f \sin\theta_f\, h_f \cos\theta_f\, d\theta_f, \tag{2.55}$$

where $R(\theta, \omega)$ denotes the reflection coefficient, and w_0 is the equal distance between source-plate and plate-receiver. Orofino and Pedersen describes their expression as electrical signal output, denoted $V(\omega)$.

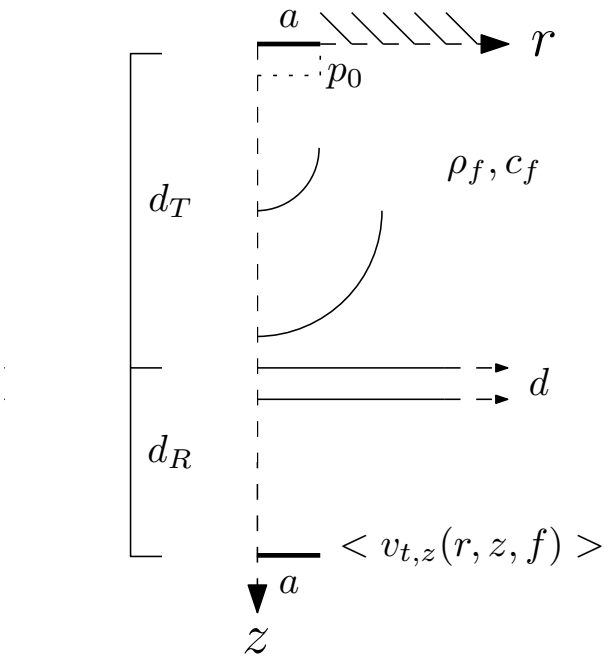

Figure 2.3: The case of model 3, which is in the cylindrical coordinate system, similar to model 1, but with constant pressure on the surface of the piston source, and the field variable of interest is the normal particle velocity.

As this notation is a bit ambiguous considering they did not include any real transducer into their expression, and because they did not include the constant value p_0 of the pressure on the surface of the piston source, the notation $V(\omega)$ is suspected to represent a transfer function, i.e., the averaged particle velocity at the surface of the receiver divided by p_0. This will therefore be used when representing their model, and the notation conventions used with model 1 and 2 will also be used. This, along with a transmission coefficient instead of reflection coefficient and the changing of $w_0 = z/2 = (d_T + d_R)/2$, gives their expression as [19][p. 43, Eq. 24]

$$\frac{< v_{t,z}(r, z = d_T + d_R, f) >}{p_0} = 2\pi \int_0^{\pi/2} V_{T,Z}(\theta_f, z = d_T + d_R, f)\, H_O(\theta_f, f) \times h_f \sin\theta_f \, h_f \cos\theta_f \, d\theta_f \quad (2.56)$$

which was also done by Waag. The subscript O denotes Orofino, capital subscript T denotes transmitted angular spectrum, and capital

subscript Z denotes the z-direction of the angular spectrum of normal particle velocity. The transmitted angular spectrum of the normal particle velocity is given as

$$V_{T,Z}(\theta_f, z = d_T + d_R, f) = \frac{\cos\theta_f}{\rho_f c_f} H_O(\theta_f, f)\, T(\theta_f, d, f)\, e^{ih_f(d_T+d_R-d)\cos\theta_f} \tag{2.57}$$

where the source and receiver aperture functions are defined equal as

$$H_O(\theta_f, f) = \frac{2J_1(h_f a \sin\theta_f)}{h_f a \sin\theta_f}. \tag{2.58}$$

The derivation of Eq. (2.57) can be done with the same method as for model 1 in Sec. 2.1., because both are in cylindrical coordinates, though Orofino and Pedersen used the independent variable θ_f instead of η as used in model 1. θ_f is the angle between the direction of the individual plane waves in the spectrum and the z-direction, where the relationship between θ_f and the horizontal and vertical wavenumbers are given as [14]

$$\eta = h_f \sin\theta_f, \tag{2.59}$$

$$h_{f,z} = h_f \cos\theta_f, \tag{2.60}$$

$$d\eta = h_f \cos\theta_f \, d\theta_f. \tag{2.61}$$

The decomposition of constant pressure on the baffled piston surface is done with the same method as decomposing constant velocity on the surface, but with a constant p_0 as the value of the constant pressure. Furthermore, converting the decomposed pressure on the source surface to normal plane-wave particle velocity is done by solving for the normal particle velocity in Eq. (2.14). Then the introduction of propagation, transmission and finite receiver are carried out the same way as model 1. However, notice that in Eq. (2.56), the upper integration limit is set to $\pi/2$. This is the same as exclusively integrating the propagating waves, and not the evanescent. If evanescent waves were included, the change of the integration limits if using the relationship given by Eq. (2.59), would be

$$\eta_{lower} = 0 \rightarrow \theta_{f,lower} = 0, \tag{2.62}$$

$$\eta_{upper} = \infty \rightarrow \theta_{f,upper} = \pi/2 - i\infty. \tag{2.63}$$

When the $i\infty$ term is included in $\theta_{f,upper}$, the integration includes evanescent waves. The notation $\pi/2 - i\infty$ is used in an article by

Lobkis and Chimenti [35] without any references or proof, so the fact that $\theta_f \to \pi/2 - i\infty$ when $\eta \to \infty$, will now be shown for the sake of validity. Using the definition of the inverse sine function [36],

$$\sin\theta_f = \frac{\eta}{h_f}, \tag{2.64}$$

$$\theta_f = \sin^{-1}(\frac{\eta}{h_f}), \tag{2.65}$$

$$\theta_f = -i\ln\big(i\frac{\eta}{h_f} + \sqrt{1 - \frac{\eta^2}{h_f^2}}\big) \text{ [36]}, \tag{2.66}$$

and with $(\eta/h_f)^2 \gg 1$ this can be approximated as

$$\theta_f \approx -i\ln\big(2i\frac{\eta}{h_f}\big), \tag{2.67}$$

$$= -i(\ln 2i\eta - \ln h_f), \tag{2.68}$$

and using that $a + ib = |r|e^{i\lambda}$ where $|r| = \sqrt{a^2 + b^2}$ and $\lambda = \tan^{-1}\frac{b}{a}$, the complex logarithm-term can be written as

$$\theta_f \approx -i(\ln|r| + \ln e^{i\lambda} - \ln h_f). \tag{2.69}$$

With $|r| = \sqrt{0 + b^2} = 2\eta$ and because $a = 0$ the limit of λ is $\lim_{x\to\infty}\lambda = \tan^{-1}(x) = \pi/2$ [37], so Eq. (2.69) becomes

$$\theta_f \approx -i(\ln 2 + \ln\eta + i\pi/2 - \ln h_f), \tag{2.70}$$

where $\ln\eta \gg \ln 2 - \ln h_f$ so

$$\theta_f \approx \pi/2 - i\ln\eta, \tag{2.71}$$

$$\lim_{\eta\to\infty}\theta_f \approx \pi/2 - i\infty = \theta_{f,upper}. \tag{2.72}$$

Note that when $\eta/h_f > 1$, the angle θ_f becomes complex, which introduces evanescent waves in the angular spectrum. This will be shown in Sec. 2.5.

Continuing on the analysis of the expression Eq. (2.57), the first term is the inverted normal impedance as used in model 1 and 2. By using that $h_{f,z} = h_f\cos\theta$ and $h_f = \omega/c_f$, the first term can be written as

$$\frac{\cos\theta_f}{\rho_f c_f} = \frac{h_{f,z}}{\omega\rho_f}, \tag{2.73}$$

and it is clear that this is the inverse of the normal impedance as used in the pressure models, model 1 and 2, Eq. 2.21 and Eq. 2.33, respectively. This is because of the relationship between pressure and particle velocity as seen in Eq. (2.14). The aperture functions have also been set equal, as Anderson and Martin, to $H_O(\theta_f, f)$. If Orofino and Pedersen/Waags expression represents a transfer function, which is an assumption, this is valid. It also appears that Orofino and Pedersen neglected the πa^2 that comes with both the aperture functions, the factor $1/\pi a^2$ that comes with the averaging, and it's also not clear to why there is a 2π outside the integral, and not $1/2\pi$ as in model 1. The total factor missing was calculated to be $a^2/4\pi$, though there are not any particle velocity models independent of the ASM to compare this with.

If including evanescent waves, the expression simply becomes

$$\frac{< v_{t,z}(r, z = d_T + d_R, f) >}{p_0} = 2\pi \int_0^{\pi/2 - i\infty} V_{T,Z}(\theta_f, z, f)\, H_O(\theta_f, f) \times h_f \sin\theta_f\, h_f \cos\theta_f\, d\theta_f, \tag{2.74}$$

with the angular spectrum given in Eq. (2.57). This will be referred to as "modified model 3", and even though evanescent waves are included, the vertical wavenumber is in this case still given as $h_{f,z} = h_f \cos\theta_f$ which will be discussed further in Sec. 2.5. The modified model 3 will be used to compare with model 3 which excludes.

Although model 3 (and modified model 3) is defined as a transfer function, where the denominator p_0 is a scalar, it fundamentally represents the normal particle velocity. The model will therefore be referred to as a representation of normal particle velocity, even though it mathematically represents a transfer function.

2.4 Additional comparison models without plate

In order to establish validity of the three models, it is necessary to compare simulations without plate with other models that are independent of the ASM and without plate. This section will introduce two additional models to compare with.

2.4.1 Williams' model

Williams [38] derived an expression for the average velocity potential over a finite receiver (without plate) that has the same radius as the source. The model was derived with the baffled piston model as defined in the present study, with a constant velocity of the surface of the source piston. The derivation of the average pressure will not be shown, but is done in [32], where the expression in cylindrical coordinates is given as (time convention $e^{-i\omega t}$)

$$< p(r,z,f) >= \rho_f c_f v_0 e^{ih_f z} \left\{ 1 - \tfrac{4}{\pi} \int_0^{\pi/2} e^{ih_f(\sqrt{z^2+4a^2\cos^2\theta}-z)} \sin^2\theta \, d\theta \right\}, \tag{2.75}$$

where θ represents the angles of deviations from a collimated beam [38], and is not the same as θ_f used in model 3, Eq. (2.56).

2.4.2 Kinsler et al. model

Kinsler et al. gives in [30] an expression for the on-axis pressure in free space without plate, i.e., with a point receiver on the acoustic axis. This is also based on the baffled piston model, with a constant velocity on the surface of the piston. The expression is given in cylindrical coordinates as (time convention $e^{i\omega t}$)

$$p_{ax}(r=0,z,f) = p_{ax}(z) = 2\rho_f c_f v_0 \left| \sin\left\{ \tfrac{1}{2} h_f z \left[\sqrt{1+(a/z)^2} - 1 \right] \right\} \right|, \tag{2.76}$$

which is valid for $z > 0$. This can be used to compare with model 1 when $b \to 0$, without plate.

2.5 Propagating and evanescent waves

This section is meant to elaborate on evanescent waves, and explain a bit further what this means mathematically.

The vertical wavenumber for model 1 is given as

$$h_{f,z} = \begin{cases} \sqrt{h_f^2 - \eta^2}, & \eta \le h_f \\ i\sqrt{\eta^2 - h_f^2}, & \eta > h_f \end{cases} \tag{2.77}$$

and for model 2 as

$$h_{f,z} = \begin{cases} \sqrt{h_f^2 - (h_{f,x}^2 + h_{f,y}^2)}, & h_{f,x}^2 + h_{f,y}^2 \leq h_f^2 \\ i\sqrt{(h_{f,x}^2 + h_{f,y}^2) - h_f^2}, & h_{f,x}^2 + h_{f,y}^2 > h_f^2 \end{cases} \tag{2.78}$$

and for modified model 3,

$$h_{f,z} = h_f \cos\theta_f. \tag{2.79}$$

It is important to note that the sign of the square root is important for the physical behavior of the wave. In this case, the sign is set as positive. When $h_{f,z}$ becomes complex, the exponential term in model 1 and 2 goes from being a complex number, to becoming a simple decaying exponential term, given as

$$e^{ih_{f,z}z} = e^{-z\sqrt{\eta^2 - h_f^2}}, \tag{2.80}$$

or for model 2

$$e^{ih_{f,z}z} = e^{-z\sqrt{(h_{f,x}^2 + h_{f,y}^2) - h_f^2}}. \tag{2.81}$$

When this happens, the angular spectrum of model 1 and model 2 become evanescent. The larger the frequency or the distance from the source, the faster these waves decay with respect to the horizontal wavenumber. For the modified model 3, the evanescent waves are introduced via the exponential term

$$e^{ih_{f,z}z} = e^{ih_f \cos\theta_f z}, \tag{2.82}$$

when θ_f becomes complex as shown in Sec. 2.3., which may be defined as $\hat{\theta}_f = \pi/2 - i\theta_f''$. The cosine of a complex number is [39]

$$\cos(\pi/2 - i\theta_f'') = \cos\pi/2 \cosh\theta_f'' + i \sin\pi/2 \sinh\theta_f'' \tag{2.83}$$

$$= i \sinh\theta_f'', \tag{2.84}$$

where the hyberbolic function $\sinh\theta_f'' > 0$. This will then give a decaying exponential term.

2.6 Transmission coefficient

The plane-wave transmission coefficient for an elastic plate is given in [15], but a more rigorous derivation is done by Aanes in [21] (though

with time convention $e^{i\omega t}$). In [15], with time convenction $e^{-i\omega t}$, it is given as

$$T(\eta, d, f) = \frac{iY(A+S)}{(S-iY)(A+iY)} \tag{2.85}$$

with Y, S and A equal to

$$Y = \frac{\rho_f h_{p,z}}{\rho_p h_{f,z}}, \tag{2.86}$$

$$S = (k_p^2 - 2\eta^2)^2 \cot(h_{p,z}\frac{d}{2}) + 4\eta^2 h_{p,z} k_{p,z} \cot(k_{p,z}\frac{d}{2}), \tag{2.87}$$

$$A = (k_p^2 - 2\eta^2)^2 \tan(h_{p,z}\frac{d}{2}) + 4\eta^2 h_{p,z} k_{p,z} \tan(k_{p,z}\frac{d}{2}), \tag{2.88}$$

where $h_p = \omega/c_{p,l}$ and $k_p = \omega/c_{p,s}$, while ρ_p represents the density of the plate. $h_{p,z}$ represents the vertical longitudinal wavenumber in the plate and $k_{p,z}$ represents the vertical shear wavenumber in the plate. To get a visualization of the different wave numbers, see figure 2.4.

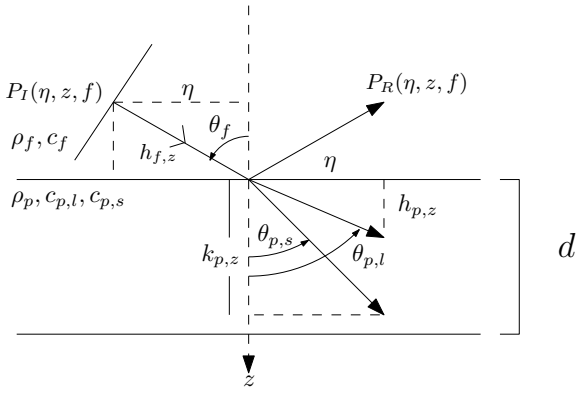

Figure 2.4: The wavenumbers of the propagating waves in the plate. $P_I(\eta, z, f)$ represents an incoming plane wave in the fluid while $P_R(\eta, z, f)$ represents a reflected wave in the fluid.

The vertical wavenumbers of the longitudinal and shear waves, $h_{p,z}$ and $k_{p,z}$, are given by

$$h_{p,z} = \begin{cases} \sqrt{h_p^2 - \eta^2}, & \eta \leq h_p \\ i\sqrt{\eta^2 - h_p^2}, & \eta > h_p \end{cases} \tag{2.89}$$

$$k_{p,z} = \begin{cases} \sqrt{k_p^2 - \eta^2}, & \eta \leq k_p \\ i\sqrt{\eta^2 - k_p^2}, & \eta > k_p \end{cases} \tag{2.90}$$

Setting $\eta = 0$ gives the transmission coefficient when the incident wave is a normally incident single plane wave. The symmetric cut-off frequencies, the frequencies of maximum or minimum transmission, for the Lamb modes is then given as [21]

$$f_{li}^{S} = \frac{(2i-1)c_{p,l}}{2d}, \qquad i = 1,\ 2,\ ...., \tag{2.91}$$

$$f_{si}^{S} = \frac{2ic_{p,s}}{2d}, \qquad i = 1,\ 2,\ ...., \tag{2.92}$$

which corresponds to the frequencies of symmetrical TE modes and thickness shear modes (TS) respectively, and the cut-off frequencies for anti-symmetric Lamb modes are

$$f_{li}^{A} = \frac{2ic_{p,l}}{2d}, \qquad i = 1,\ 2,\ .... \tag{2.93}$$

$$f_{si}^{A} = \frac{(2i-1)c_{p,s}}{2d}, \qquad i = 1,\ 2,\ ...., \tag{2.94}$$

which again corresponds to the frequencies of anti-symmetrical TE modes and TS modes, respectively.

2.6.1 Dispersion equations

In an article by Osbourne and Hart [5], dispersion equations for anti-symmetrical and symmetrical leaky Lamb modes of a plate immersed in water are given. The equations are given in terms of the horizontal wavenumber and phase velocity which in this case is η and $c_{ph} = \omega/\eta$, respectively, so

Symmetric:

$$\begin{aligned} &4\big[\big(1-\frac{1}{2}\frac{c_{ph}^2}{c_{s,p}^2}\big)^2 \coth\big(\eta\frac{d}{2}\big(1-\frac{c_{ph}^2}{c_{p,l}^2}\big)^{\frac{1}{2}}\big) - \big(1-\frac{c_{ph}^2}{c_{p,l}^2}\big)^{\frac{1}{2}}\big(1-\frac{c_{ph}^2}{c_{p,s}^2}\big)^{\frac{1}{2}} \\ &\times \coth\big(\eta\frac{d}{2}\big(1-\frac{c_{ph}^2}{c_{p,s}^2}\big)^{\frac{1}{2}}\big)\big] + \frac{\rho_f}{\rho_p}\frac{c_f^2}{c_{p,s}^2}\frac{1}{\big(1-\frac{c_{ph}^2}{c_f^2}\big)^{\frac{1}{2}}}\frac{c_{ph}^4}{c_f^2 c_s^2}\big(1-\frac{c_{ph}^2}{c_{p,l}^2}\big)^{\frac{1}{2}} \\ &= 0, \end{aligned} \tag{2.95}$$

Antisymmetric:

$$4\big[\big(1-\frac{1}{2}\frac{c_{ph}^2}{c_{p,s}^2}\big)^2\tanh\big(\eta\frac{d}{2}\big(1-\frac{c_{ph}^2}{c_{p,l}^2}\big)^{\frac{1}{2}}\big)-\big(1-\frac{c_{ph}^2}{c_{p,l}^2}\big)^{\frac{1}{2}}\big(1-\frac{c_{ph}^2}{c_{p,s}^2}\big)^{\frac{1}{2}*}$$
$$\times\tanh\big(\eta\frac{d}{2}\big(1-\frac{c_{ph}^2}{c_{p,s}^2}\big)^{\frac{1}{2}}\big)\big]+\frac{\rho_f}{\rho_p}\frac{c_f^2}{c_{p,s}^2}\frac{1}{\big(1-\frac{c_{ph}^2}{c_f^2}\big)^{\frac{1}{2}}}\frac{c_{ph}^4}{c_f^2c_{p,s}^2}\big(1-\frac{c_{ph}^2}{c_{p,l}^2}\big)^{\frac{1}{2}}$$
$$=0. \tag{2.96}$$

Notice at the end of the first line in Eq. (2.96), there is an asterisk. This is there to suggest that Osbourne and Hart in [5] [p. 7, Eq. 26.] forgot to include the square root, which is included in their symmetrical equation [5][p. 7, Eq. 25] in their article. Later calculations using this also agrees with simulations, which are shown in Sec. 5.4.

2.7 Transfer functions in plate transmission

In order to investigate plate transmission effects with a point receiver, the pressure-to-pressure transfer function $\mathrm{H_{pp}}(f)$ as a function of frequency have been frequently used, e.g [18], [21], [26], [25], [27], [28], [29]. This is defined as

$$\mathrm{H_{pp}}(f)=\frac{p_t(r=0,z=d_T+d_R,f)}{p_i(r=0,z=d_T,f)}, \tag{2.97}$$

where $p_i(r=0,z=d_T,f)$ is the on-axis pressure on the surface on the upper side of the plate at a point receiver, while $p_t(r=0,z=d_T+d_R,f)$ is the transmitted on-axis pressure at the point receiver. Because this transfer function requires a point receiver, only model 1, Eq. (2.29 with $b\to 0$) can be used to calculate this function. See Fig. 2.5. for an illustration of the transfer function.

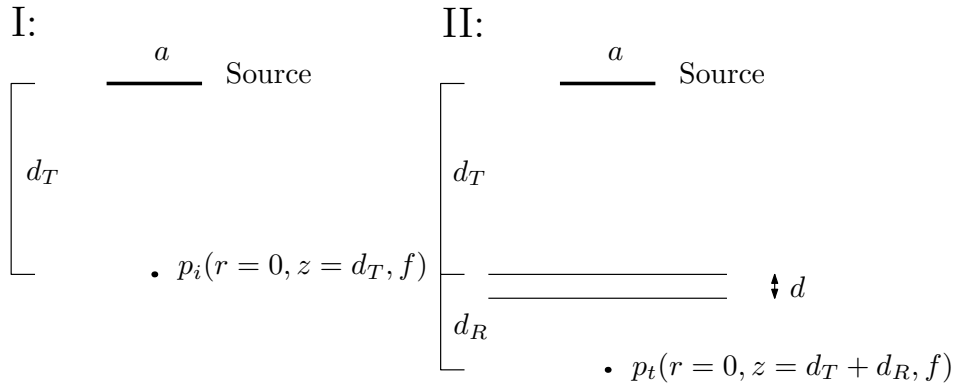

Figure 2.5: $\mathrm{H_{pp}}(f)$ illustrated. $p_i(r = 0, z = d_T, f)$ represents the on-axis, free-field pressure at the upper side of the plate where $z = d_T$, while $p_t(r = 0, z = d_T + d_R, f)$ is the on-axis free-field transmitted pressure at $z = d_T + d_R$.

In addition to this, in order to see the influence of a finite receiver in the case of plate transmission, the newly defined $\mathrm{H_{p<p>}}(f)$ for the thesis is also of interest. This transfer function is the ratio of the transmitted average pressure at a finite receiver and the on-axis pressure on the upper side of the plate as a function of frequency, giving the transfer function

$$\mathrm{H_{p<p>}}(f) = \frac{< p_t(r, z = d_T + d_R, f) >}{p_i(r = 0, z = d_T, f)}, \tag{2.98}$$

which again can only be used with model 1, Eq. (2.29), because the model allows for a different radius on the source and receiver. See Fig. 2.6. for an illustration of the transfer function.

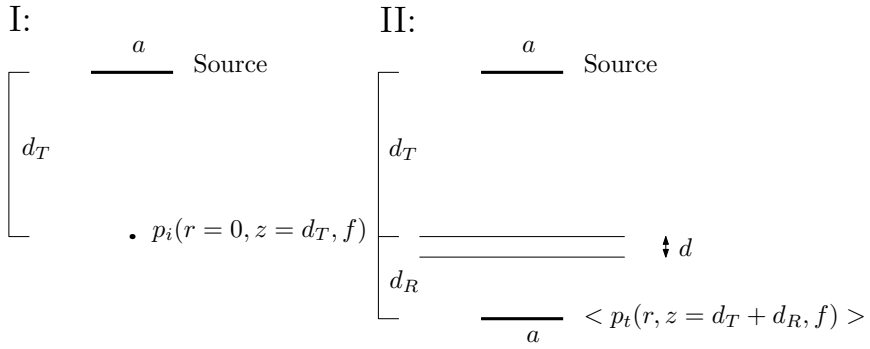

Figure 2.6: $\mathrm{H_{p<p>}}(f)$ illustrated. $p_i(r = 0, z = d_T, f)$ represents the on-axis, free-field pressure at the upper side of the plate where $z = d_T$, while $< p_t(r, z = d_T + d_R, f) >$ is the average transmitted pressure at the finite receiver at $z = d_T + d_R$.

In order to compare model 1 and 2 with plate transmission with each other, a third transfer function, $\mathrm{H}_{<\mathrm{p}><\mathrm{p}>}(f)$, will also be used. This is defined as the ratio between the average transmitted pressure and the average incoming pressure as a function of frequency, as

$$\mathrm{H}_{<\mathrm{p}><\mathrm{p}>}(f) = \frac{< p_t(r, z = d_T + d_R, f) >}{< p_i(r, z = d_T, f) >}, \tag{2.99}$$

where an illustration is given in Fig. 2.7.

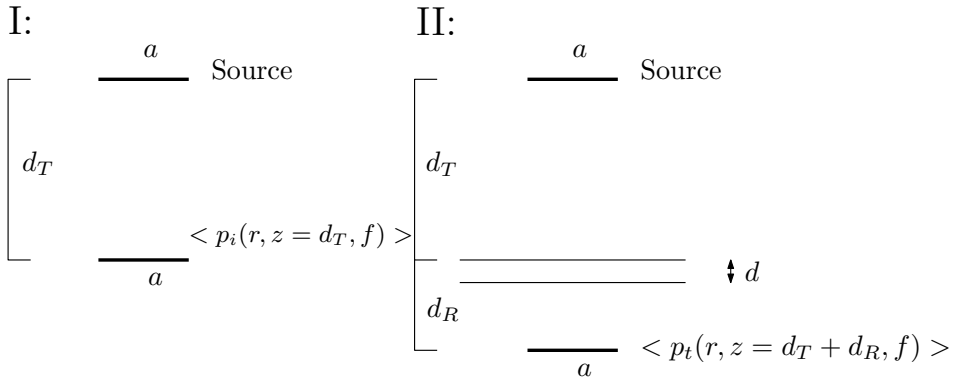

Figure 2.7: $\mathrm{H}_{<\mathrm{p}><\mathrm{p}>}(f)$ illustrated. $< p_i(r, z = d_T, f) >$ represents the average pressure at a finite receiver at the upper side of the plate where $z = d_T$, while $< p_t(r, z = d_T + d_R, f) >$ is the average transmitted pressure at a finite receiver at $z = d_T + d_R$.

Equivalently, for model 3 yields a particle velocity to particle velocity transfer function

$$\mathrm{H}_{<\mathrm{pv}><\mathrm{pv}>}(f) = \frac{< v_t(r, z = d_T + d_R, f) >}{< v_i(r, z = d_T, f) >}, \tag{2.100}$$

which can be compared with Eq. (2.99).

Finally, the last transfer function of interest, which is used in e.g. [25] and [28], is the transfer function $\mathrm{H}_{\mathrm{pp}}^{\mathrm{plate}}$ which is defined as the ratio between the on-axis transmitted pressure at the surface of the lower side of the plate, and incident on-axis pressure on the upper side of the plate, as

$$\mathrm{H}_{\mathrm{pp}}^{\mathrm{plate}} = \frac{p_t(r = 0, z = d_T + d, f)}{p_i(r = 0, z = d_T, f)}. \tag{2.101}$$

This will be used to reproduce some results from [25] and [28], in Sec. 6.1.

2.8 Introducing losses in fluid

Losses in fluid can be introduced in order to overcome sampling challenges, and losses will only be introduced in the fluid and not the plate, for reasons which will be discussed in Sec. 5.1.1. and Sec. 5.4.

The losses in fluid can be defined in terms of a loss-factor Q_f where the relationship between Q_f and the absorption coefficient α_f, is [30]

$$\alpha_f = \frac{1}{2}\frac{h_f}{Q_f}, \tag{2.102}$$

which is incorporated in the wavenumber of the fluid as

$$\hat{h}_f = h_f + i\alpha_f \tag{2.103}$$

Q_f is kept constant, which means that α_f is proportional with frequency, and not frequency squared. A proportionality with frequency squared is used in e.g. [30]. With the introduction of a complex wavenumber, there is not at singularity at $\eta = h_f$, which can be shown with the insertion of $\hat{h}_f$ into $h_{f,z}$ as

$$h_{f,z} = \sqrt{\hat{h}_f^2 - \eta^2}, \tag{2.104}$$

$$= \sqrt{h_f^2 + i2h_f\alpha_f - \alpha_f^2 - \eta^2}, \tag{2.105}$$

and with $\eta = h_f$, it becomes

$$h_{f,z} = \sqrt{i2h_f\alpha_f - \alpha_f^2}. \tag{2.106}$$

Chapter 3

Simulation setups and methods

This chapter explains the simulation setups and methods used within the different models. First the simulation parameters are presented in Sec. 3.1., with an explanation of the choice of parameters, before the simulation methods used with model 1 are explained in Sec. 3.2. In Sec. 3.3, the simulation methods used for model 2 are explained, and in Sec. 3.4., the simulation methods used with model 3 are also explained. All the models were implemented using MATLAB®.

3.1 Simulation parameters

The following parameters have been used in all the simulations unless otherwise specified:

- $1\,\mathrm{kHz} \leq Frequency \leq 1000\,\mathrm{kHz}$ with a step of $\Delta f = 1\,\mathrm{kHz}$,
- $a = b = 10.55\,\mathrm{mm}$,
- $c_f = 1485\,\mathrm{m} \cdot \mathrm{s}^{-1}$,
- $\rho_f = 1000\,\mathrm{kg} \cdot \mathrm{m}^{-3}$,
- $v_0 = 1\,\mathrm{m} \cdot \mathrm{s}^{-1}$,
- $\rho_p = 8000\,\mathrm{kg} \cdot \mathrm{m}^{-3}$,
- $c_{p,l} = 5780\,\mathrm{m} \cdot \mathrm{s}^{-1}$,

- $c_{p,s} = 3130\,\mathrm{m} \cdot \mathrm{s}^{-1}$,
- Poisson's ratio $\sigma = 0.293$
- $d_T = 270\,\mathrm{mm}$,
- $d_R = 106.05\,\mathrm{mm}$,
- $d = 6.05\,\mathrm{mm}$,
- $z = d_T + d_R = 376.05\,\mathrm{mm}$,
- $Q_f = 50 \cdot 10^3$,
- $\Delta z = 1\,\mathrm{mm}$,

where a, c_f, ρ_f, ρ_p, c_l, c_s, σ, d_T, d_R, d are the parameters used in previous work within the acoustics group at the University of Bergen, [18], [21], [25], [27], [28]. The radius a is the effective radius of the transducer used and built by Aanes in [21], when adjusted to a frequency of 575 kHz which is the frequency of maximum source sensitivity, see [21]. The effective radius is determined by using the relationship [21]

$$a = \frac{1.6137}{h_f \sin\theta_{-3\mathrm{dB}}} \tag{3.1}$$

where θ_{-3dB} is the 3dB-angle of the real transducer. This means that comparisons between measurements and simulations may be a bit off for lower or higher frequencies than 575 kHz, and the effect of this will be shown in Sec. 5.5.

The loss factor Q_f will be introduced when simulating the models at low frequencies with plate transmission. In Sec. 5.4., the presence of surface waves, known as Scholte-waves, in the transmission coefficient is discussed, which appears as singularities in the transmission coefficient. In order to be able to calculate the models' field variables at low frequencies, these singularities need to be dampened with the introduction of loss, if not, the simulations are inflicted by undersampling effects. The loss factor of $Q_f = 50 \cdot 10^3$, was determined by checking at which loss factor the models were able to produce a non-undersampled field variable while maintaining decent computational efficiency at these low frequencies.

3.2 Model 1

3.2.1 Maximum wavenumber

Common for all models, is that the independent variables are the first variables that are determined. In model 1, this is the horizontal wavenumber η, where the maximum wavenumber η_{max} needs to be determined. The requirement of the maximum wavenumber is that it is set to a point where the angular spectrum is truncated when the evanescent part is negligible. Knowing this, a temporary array is created, streching from h_f to a high number with a step of $1\,\mathrm{rad}\cdot\mathrm{m}^{-1}$. The expression of the angular spectrum, Eq. (2.21), is then calculated for this range of wavenumbers, until the decaying pressure in Decibels is below some threshold-limit, which is set to $-200\,\mathrm{dB}$. This means that the absolute value of the angular spectrum at this point is less than $1 \cdot 10^{-10}$ which is deemed as negligible. Whenever this limit is reached, the wavenumber is stored and set as the maximum wavenumber. See Appendix D for the implementation of this algorithm in MATLAB®.

3.2.2 Non-uniform sampling

With the maximum wavenumber found, a non-uniform sampling routine is run. In Sec. 2.1., it was stated that when there are no losses in the fluid and $\eta = h_f$, there is a singularity in the angular spectrum because of the inverse proportionality with $h_{f,z}$, which becomes zero. In order to avoid this, but still sample close to this point, a non-uniform sampling method was implemented. Additionally, the singularities in the transmission coefficient caused by the surface waves are also sampled closely, even with losses, to ensure that they are decently represented in the transmission coefficient. The wavenumbers at which these waves appear are labeled as the symmetric Scholte-wave η_S and the antrisymmetric Scholte-wave η_A which is bigger than η_S. First the algorithm of non-uniform sampling without a plate is explained, in order to set some preliminary theory for when a plate is included.

The algorithm of non-uniform sampling, FindEta, see Appendix E, without a plate, first sets a vector with a small sampling step around h_f. With a given h_f the algorithm sets a minimum and maximum limit on the sampling area around h_f. These limits have been chosen to be $\eta_{h_f,min} = h_f - h_f/N$ and $\eta_{h_f,max} = h_f + h_f/(N-1)$ where N is the

number of samples and is an even number. The sampling step in this area is then

$$\Delta\eta_{h_f} = \frac{\eta_{h_f,max} - \eta_{h_f,min}}{N} = \frac{h_f(2N-1)}{N(N-1)}, \tag{3.2}$$

and the wavenumber vector is

$$\eta_{h_f} = \eta_{h_f,min} + l\Delta\eta_{h_f}, \;\; l = 0,\, 1,\, ...\; N-1. \tag{3.3}$$

In Fig. 3.1. the idea is simply illustrated.

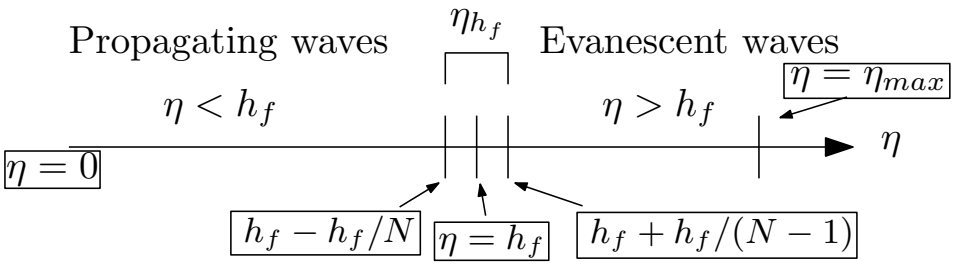

Figure 3.1: The algorithm of non-uniform sampling sets some boundaries around h_f where an extra small sampling step is to be used.

The reason that $\eta_{h_f,max}$ was set to $h_f + h_f/(N-1)$, i.e., with the subtraction $N-1$ in the denominator, is to avoid that the vector hits h_f exactly. If the wavenumber vector is given as in Eq. (3.3), it means that in order to hit h_f exactly, the following is true

$$\eta_{h_f,min} + l\Delta\eta_{h_f} = h_f. \tag{3.4}$$

Inserting Eq. (3.2) for $\Delta\eta_{h_f}$ and with $\eta_{h_f,min} = h_f - h_f/N$, the equation becomes

$$h_f - h_f/N + l\frac{h_f(2N-1)}{N(N-1)} = h_f. \tag{3.5}$$

Solving for l gives

$$l = \frac{N-1}{2N-1}, \tag{3.6}$$

where the left side l is an integer while the right side is less than 1, which is a contradiction, i.e., it is not possible to hit h_f. If $\eta_{h_f,min}$ and $\eta_{h_f,max}$ had an addition and subtraction of h_f/N respectively, l would

be equal to $l = N/2$, and would give the singularity and numerical error in the simulations.

When h_f is sampled, the vector of wavenumbers for the entire spectrum are declared with the concatenation of three sets: the wavenumbers for the propagating part of the spectrum η_{prop}, the wavenumbers for η_{h_f}, and wavenumbers for the evanescent part η_{evsct}. Using the following relationships for the minimum and maximums wavenumbers for the propagating and evanescent parts

$$\eta_{prop,min} = 0, \tag{3.7}$$

$$\eta_{prop,max} = \eta_{h_f,min}, \tag{3.8}$$

$$\eta_{evsct,min} = \eta_{h_f,max}, \tag{3.9}$$

$$\eta_{evsct,max} = \eta_{max}, \tag{3.10}$$

where the individual sampling steps are given by

$$\Delta\eta_{prop} = \frac{\eta_{prop,max}}{N}, \tag{3.11}$$

$$\Delta\eta_{evsct} = \frac{\eta_{evsct,max} - \eta_{evsct,min}}{N}. \tag{3.12}$$

Finally the individual vectors are

$$\eta_{prop} = l\Delta\eta_{prop}, \qquad l = 0,\ 1,\ \ldots,\ N-1, \tag{3.13}$$

$$\eta_{evsct} = \eta_{evsct,min} + l\Delta\eta_{evsct}, \qquad l = 0,\ 1,\ \ldots,\ N-1. \tag{3.14}$$

The final η vector is then created by concatenating the three vectors η_{prop}, η_{h_f}, η_{evsct}. It should also be mentioned that the choice of N for the sampling step of the evanescent part, Eq. (3.12), is doubled in the nearfield where the evanescent part may need a high number of samples.

A similar routine is also run when a plate is included, but the wavenumbers η_S and η_A needs to be determined. This is done by using the dispersion equations by Osbourne and Hart, Eqs. (2.95) and (2.96), and inserting a temporary wavenumber vector η and phase velocity c_{ph}. The minima at $\eta > h_f$ are found for the two equations, which then represent η_S and η_A. Once these are decided, the non-uniform sampling routine is run. The upper limit around h_f is set to $\eta_{h_f,max} = \eta_S + \eta_S/(N-1)$ because the wavenumber $\eta_{Scholte,S}$ is very close to h_f. The sampling step however, is doubled as

$$\Delta\eta_{h_f,S} = \frac{\eta_{h_f,max} - \eta_{h_f,min}}{2N}, \tag{3.15}$$

to ensure that both the singularity at h_f and η_S is sampled good enough. The wavenumber vector is then set as

$$\eta_{h_f,S} = \eta_{h_f,min} + m\Delta\eta_{h_f,S},\ m = 0,\ 1,\ \ldots,\ 2N-1. \tag{3.16}$$

Following this, the wavenumber-vector around the antisymmetric Scholte-wave at wavenumber η_A are found, where the limits are set as $\eta_{A,min} = \eta_A - \eta_A/N$ and $\eta_{A,max} = \eta_A + \eta_A/(N-1)$, where the sampling step is

$$\Delta\eta_A = \frac{\eta_{A,max} - \eta_{A,min}}{N}, \tag{3.17}$$

with the wavenumber vector

$$\eta_A = \eta_{A,min} + l\Delta\eta_A,\ l = 0,\ 1,\ \ldots,\ N-1. \tag{3.18}$$

This also requires the space between η_S and η_A to be sampled, where the minimum and maximum wavenumber are set as

$$\eta_{StoA,min} = \eta_{h_f,max}, \tag{3.19}$$

$$\eta_{StoA,max} = \eta_{A,min}, \tag{3.20}$$

$$\tag{3.21}$$

with the sampling step

$$\Delta\eta_{StoA} = \frac{\eta_{StoA,max} - \eta_{StoA,min}}{N}, \tag{3.22}$$

which gives the wavenumber vector as

$$\eta_{StoA} = \eta_{StoA,min} + l\Delta\eta_{StoA},\ l = 0,\ 1,\ \ldots,\ N-1. \tag{3.23}$$

Finally the remaining wavenumber vectors for the propagating and evanescent part are set as

$$\eta_{prop,min} = 0, \tag{3.24}$$

$$\eta_{prop,max} = \eta_{h_f,min}, \tag{3.25}$$

$$\eta_{evsct,min} = \eta_{A,max}, \tag{3.26}$$

$$\eta_{evsct,max} = \eta_{max}, \tag{3.27}$$

where the respective sampling steps and wavenumbers are defined in Eqs. (3.11), (3.12), and Eqs. (3.13), (3.14). The final vector for η is created by concatenating η_{prop}, $\eta_{h_f,S}$, η_{StoA}, η_A, η_{evsct}.

3.2.3 The implementation of equations

In Appendix A the code for the program and the implementation of Eq. (2.29) are shown. First all the constant variables are declared. Then the program iterates through two for()-loops, where the outer loop iterates through a vector of distances, while the inner loop iterates through a vector of frequencies. This is convenient if the pressure as a function of frequency and distance is to be calculated. Inside the inner loop, a number of samples N is set, which in general has been set to $N = 512 \times 512 = 2^{18}$. This allows for a fairly fast computational time, which for a typical scenario, e.g. calculation of transmitted pressure, takes about 5 s per calculation. This means that 900 points of calculation takes approximately 1 h, which was deemed fast enough. Following this is the determining of the maximum horizontal wavenumber, and the non-uniform sampling routine. When this is finished, all the terms in the expression are declared, and the final expression is then integrated using a trapezoidal method by MATLAB®, *trapz(x, y)*, which takes an integration limit x and an integrand y as input. The integration limit is simply the η-vector calculated in the program, while the integrand is the integrand of Eq. (2.29).

3.3 Model 2

Although model 2 is three-dimensional, where the independent wavenumbers, $h_{f,x}$ and $h_{f,y}$, are in two dimensions, the deciding of maximum wavenumber and the non-uniform sampling routine are run with the wavenumbers in one dimension which conveniently lets the routines described in Sec. 3.2.1. and Sec. 3.2.2. to be used.

3.3.1 Non-uniform sampling

Exploiting symmetry, only the maximum wavenumber in one direction is needed, e.g., $h_{f,x,max}$. When this is determined, the non-uniform sampling around h_f and the singularities caused by the Scholte-waves, are found with the same method as in Sec. 3.2.2. This returns a temporary vector that stretches from 0 to $h_{f,x,max}$, which can be labeled as $h_{f,x,temp}$. Declaring then a new vector equal to $h_{f,x,temp}$, but which is set negative and flipped using MATLAB® *fliplr()*. This is

concatenated with $h_{f,x,temp}$, and creates a one-dimensional vector $h_{f,x}$, stretching from $-h_{f,x,max}$ to $h_{f,x,max}$ which is also equal to $h_{f,y}$. The two-dimensional matrix form of these two are created using MATLAB® $meshgrid(h_{f,x}, h_{f,y})$ which creates two matrices $[h_{f,x}]$, $[h_{f,x}]$, where one have equal elements in the column-direction, while the other have equal elements in the row-direction. Declaring then $\eta = \sqrt{[h_{f,x}]^2 + [h_{f,y}]^2}$ for further calculations.

3.3.2 The implementation of equations

The implementation of the expression Eq. (2.32) is exactly the same as described in Sec. 3.2.3., though the trapezoidal method is handled a bit differently. When the integration limits are two-dimensional, the *trapz()* routine is simply run twice. Also, the number of samples is set as $N = 1024 \times 1024 = 2^{20}$ samples, which needs some commenting. The sampling of the spectrum is, as stated, in two dimensions. This means that the amount of samples is limited if computational efficiency are of importance. With this, model 2 is very sensitive to undersampling effects, and especially for low frequencies within the approximate interval between $f = 10\,\text{kHz}$ and $f = 80\,\text{kHz}$, model 2 struggles to sample correctly. The results of this is shown in Sec. 5.5. This problem can be fixed by increasing the number of samples, but with this comes more computational demanding calculations. With the amount of samples $N = 1024 \times 1024$ the computational time is about 40 s for the calculation of one point in the case of plate transmission, which would require even more time if the frequency range subjected to undersampling were to be sampled better. The sampling method could perhaps be improved, but because the frequencies of undersampling is for a small range of frequencies, it was deemed unimportant to improve the methods and calculation time. See Appendix B for the code.

3.4 Model 3

Orofino and Pedersen/Waag neglects evanescent waves, so the maximum angle can simply be set to $\theta_{f,max} = \pi/2$. The sampling step is then

$$\Delta\theta_f = \frac{\theta_{f,max}}{N} \tag{3.28}$$

and the angle-vector is

$$\theta_f = l\Delta\theta_f,\ l = 0, 1, \ ..., N-1 \tag{3.29}$$

If however including evanescent waves, the same routines as described with model 1 in Sec. 3.2. are run, where η_{max} is found and used to decide a temporary wavenumber vector. The threshold of truncating the algorithm is different however, because the spectrum of model 3 in dB is much less than 0, see Sec. 5.3.1., so the threshold is set as a difference. The algorithm checks when the difference between the maximum value of the particle velocity spectrum and some later value in the evanescent part, is bigger than approximately 200 dB. With η_{max} determined and the wavenumber-vector created, it is simply converted to θ_f by using the relationship

$$\theta_f = \sin^{-1}\frac{\eta}{h_f}, \tag{3.30}$$

which is then used for the further implementation. Besides this, the rest of the implementation and handling of the integration is also as done as with model 1. The number of samples used with model 3 when excluding evanescent waves have been set to $N = 1024 * 32 = 2^{15}$ samples, while the same number of samples as model 1 are used when including evanescent waves. See Appendix C for the code.

Chapter 4

Experimental setup and methods

To confirm and validate simulations, it is of interest to do comparisons with measurements. In Sec. 4.1., an overview of the technical experimental setup used to do measurements is given. In Sec. 4.2., the methods used when measuring the transfer functions defined in Sec. 2.7. are described, before the post-process of the measurements are explained in Sec. 4.3.

4.1 Experimental setup

The signal flow in the experimental setup without plate when using a hydrophone is illustrated in figure 4.1. This setup was developed and used by Aanes in [21]. The computer sets the parameters of the signal in the signal generator - length of signal in time, voltage amplitude, frequency, and burst rate - that is to be sent to the transducer which is in-house built [21]. Aanes built two transducers, "prototype no. 2" and "prototype no. 3", for the frequency range of 350 kHz to 1000 kHz, and in the present work, "prototype no. 3" is used as source.

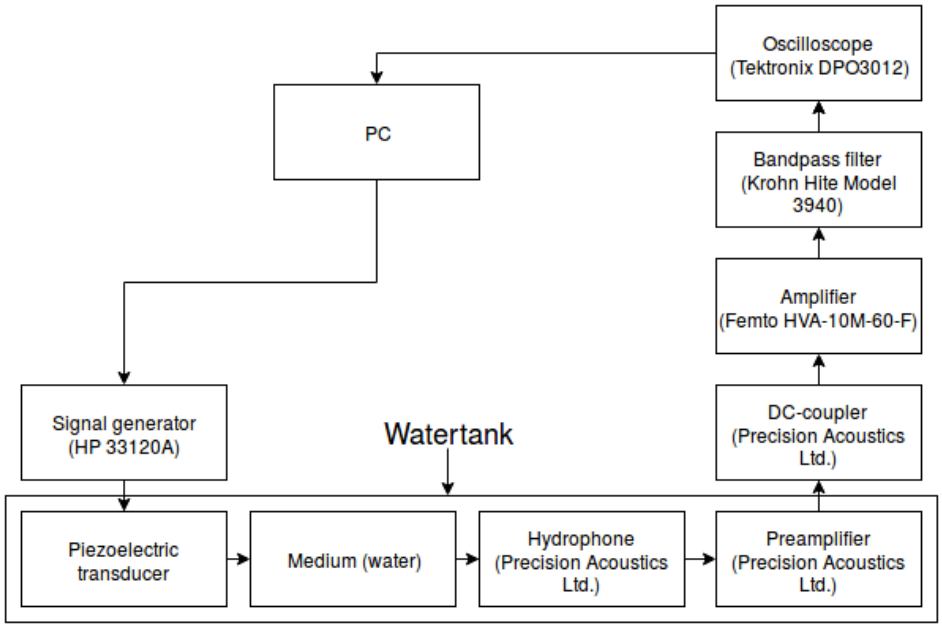

Figure 4.1: The experimental setup when doing hydrophone measurements.

The time length of the signal is set to 130 µs, the voltage amplitude to 20 V_{p-p}, and the burst rate varied between 25 Hz and 100 Hz depending on other parameters, e.g. distance between source and receiver. A low burst rate is used if there is a big distance between the source and receiver. The signal generator then sends a signal with the given parameters to "prototype no. 3" located in a water tank (with size height $\times$ width $\times$ length $= 60 \times 75 \times 160$ cm^3), and radiates towards the PVDF needle hydrophone (Precision Acoustics Ltd.). The hydrophone has a probe length of 100 mm, with 1 mm in diameter, and an uncertainty of ± 0.8 dB [40]. The received signal is terminated with 50 Ω in parallel with an amplifier (HVA-10M-60-F, Precision Acoustics Ltd.) which has an input impedance 1 MΩ and an amplifier gain of approximately 46 dB [21]. This is connected through an coaxial cable with the DC-coupler(Precision Acoustics Ltd.). The amplified signal is then filtered in a bandpass filter (100 kHz − 2 MHz) of type Krohn Hite Model 3940, and the signal is received by the oscilloscope (Tektronix DPO3012). The computer also sets the oscilloscope parameters, i.e., the amount of samples, the time of how long the oscilloscope waits before storing the data in the computer, and the amount of bursts to find an average of. The amount of samples is set to $100 \cdot 10^3$ samples, while

an average of 256 bursts is used in the present work.

The signal flow in the experimental setup when using a finite receiver is illustrated in figure 4.2.

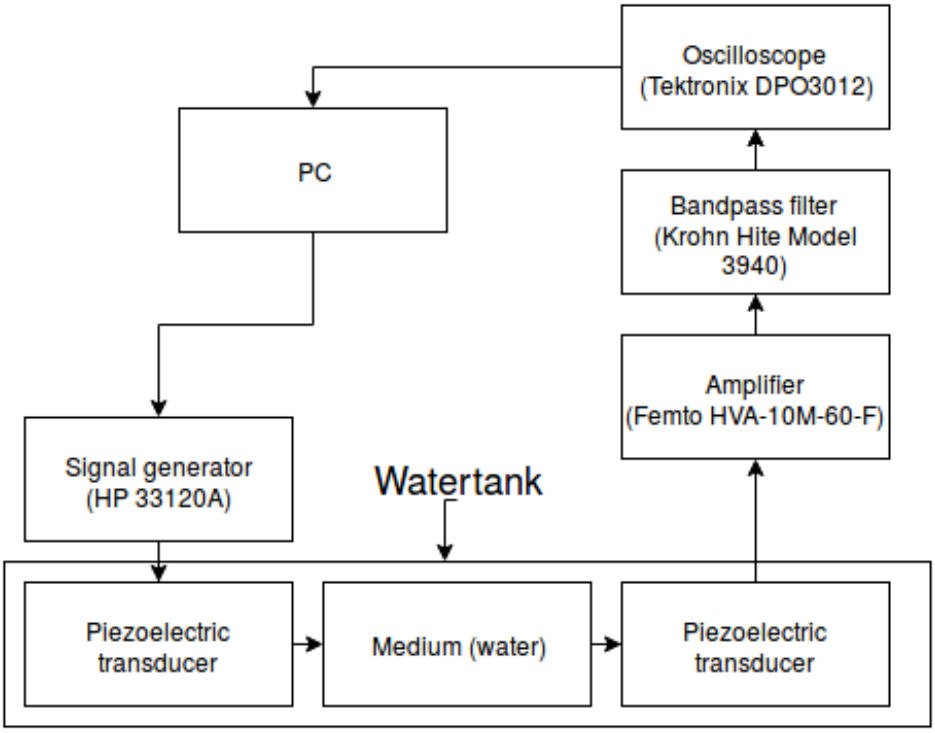

Figure 4.2: The experimental setup when doing finite receiver measurements

Similar to the hydrophone setup, but without the DC-coupler and the 50 Ω termination, as the DC-coupler is the supply voltage needed for the hydrophone preamplifier. The parameters on the signal generator were similar to that of the hydrophone, except for the voltage amplitude which is set to 100 mV. "Prototype no. 2" is used as a receiver.

The motor-stages are illustrated in figure 4.3, which are independent of whether the receiver is finite or a hydrophone. The linear stage Parker 404XE T09 sets the position of the receiver in the y-direction, the linear stage Micos LMS-100 sets the position in the x-direction, and the Parker 404XE T07 sets the position in the z-direction. The rotary Micos PRS100 controls the angle of incidence of the source. The different stages are controlled with commands through drivers which again are controlled with the computer.

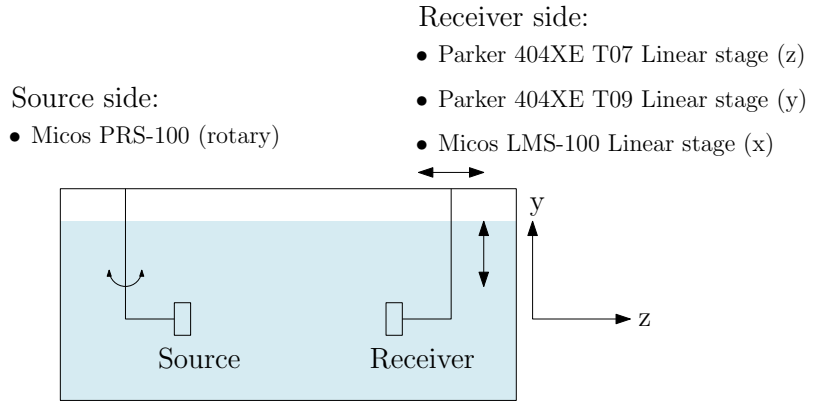

Figure 4.3: The different motor stages of the setup. The x-axis represents the width of the tank, the y-axis represents the height, while the z-axis represents the length. The positive x-axis goes into the screen.

4.2 Methods

4.2.1 Aligning the source and receiver

To be able to measure the on-axis pressure with a hydrophone, the hydrophone has to be perfectly parallel and in center of the source. A laser with horizontal and vertical beams is put on the opposite side of the source so that the laser-cross is in the center of it. Then the hydrophone is placed in front of the laser again, so that the cross is in the center on the backside of the hydrophone. The hydrophone is then simply moved along the x-axis to find the maximum pressure via the readings on the oscilloscope, and then along the y-axis. The rotary stage is also used to rotate the source to check if the pressure increases or decreases with a small rotary step. This method of aligning the source and receiver is the same if using a finite receiver.

4.2.2 Measuring $\mathrm{H_{pp}}(f)$

The setup when measuring $\mathrm{H_{pp}}(f)$ is illustrated in Fig. 4.4.

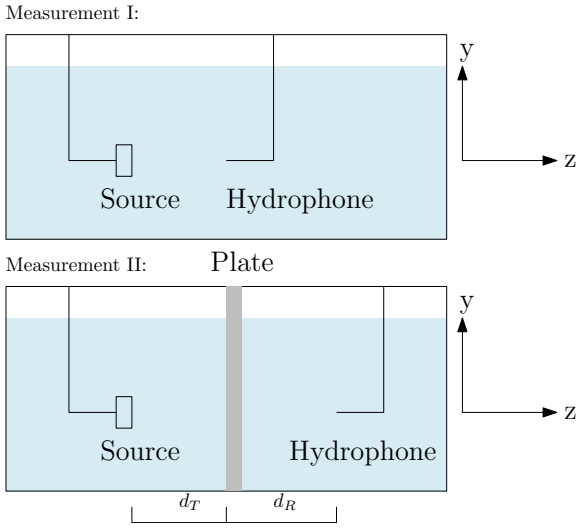

Figure 4.4: The setup and steps when measuring $\mathrm{H_{pp}}(f)$.

The plate is a AISI 316L stainless steel plate with a thickness $d = 6.05\,\mathrm{mm}$, length of 760 mm and width of 500 mm [21]. First the pressure at $z = d_T$ is measured as a function of frequency. Then the plate is inserted and the hydrophone is positioned at $z = d_T + d_R$ to measure the transmitted pressure as a function of frequency. Measuring the distances between the elements are done using in-house constructed measuring pieces or with the use of the arrival time on the oscilloscope without the plate present.

4.2.3 Measuring $\mathrm{H_{p<p>}}(f)$

This transfer function was not measured because the receiver sensitivity on the transducers have not yet been determined.

4.2.4 Measuring $\mathrm{H_{<p><p>}}(f)$

The setup when measuring $\mathrm{H_{<p><p>}}(f)$ is illustrated in Fig. 4.5.

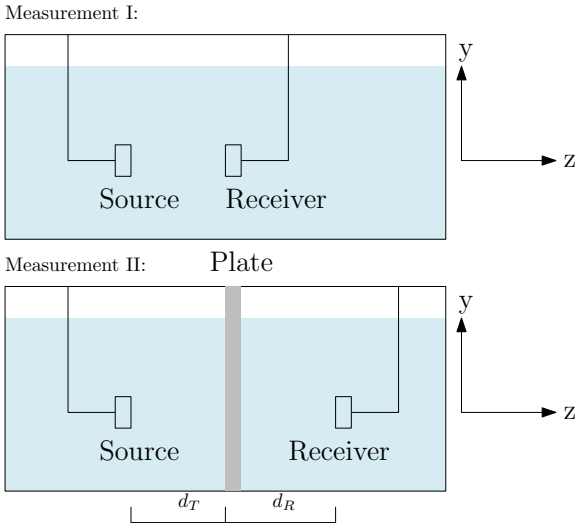

Figure 4.5: The setup and steps when measuring $H_{<p><p>}(f)$

The steps are the same as when the receiver is a hydrophone in Sec. 4.2.2.

4.3 Post-processing of data

4.3.1 $H_{pp}(f)$

The measured voltage at the respective distances are converted from the time-domain to the frequency domain, by using Fourier analysis to retrieve the voltage in the frequency domain. By then using the relationship between the receiver sensitivity, voltage and pressure as [21]

$$p(f) = \frac{V(f)}{M_{hyd}(f)}, \tag{4.1}$$

where $p(f)$ is the pressure, $V(f)$ is the measured voltage, and $M_{hyd}(f)$ is the receiver sensitivity of the hydrophone. The receiver sensitivity was calibrated by National Physics Laboratory(NPL) [40], but was also calibrated by Aanes [21].

4.3.2 $H_{<p><p>}(f)$

The receiver sensitivity is not yet determined for the transducers, but the transfer function is relative, so the voltages in the frequency domain can be used. This can be shown by using the relationship for the pressure, voltage, and receiver sensitivity, the transfer function can be calculated as

$$\begin{aligned} H_{<p><p>}(f) &= \frac{< p_t(r, z = d_T + d_R, f) >}{< p_i(r, z = d_T, f) >} \\ &= \frac{\frac{<V_t(r, z=d_T+d_R, f)>}{Mv(f)}}{\frac{<V_i(r, z=d_T, f)>}{Mv(f)}} \\ &= \frac{< V_t(r, z = d_T + d_R, f) >}{< V_i(r, z = d_T, f) >}, \end{aligned} \tag{4.2}$$

which is compared with simulations in Sec. 5.5.

Because the receiver sensitivity is not determined, the transfer function $H_{p<p>}(f)$ can not be measured. The reason is that the transfer function is the ratio between the average transmitted pressure at the surface of the receiver and the on-axis pressure on the upper side of the plate. In order to find this ratio, the respective voltages needs to be converted to pressure by using the receiver sensitivity.

Chapter 5

Comparison of the models

This chapter will compare the models, without plate and with plate, in order to establish potential differences, confirm validity of the models, and investigate the influence of a finite receiver. The simulation parameters given in Sec. 3.1. will be used unless otherwise stated.

In Sec. 5.1., simulation results of model 1 without plate are presented, with some examples of the calculated magnitude and phase of the angular spectrum, followed by comparisons with the models by Kinsler et al. and Williams, before some discussion concerning the exclusion or inclusion of evanescent waves. In Sec. 5.2., the results of model 2 without plate are presented, with examples of magnitude and phase of the angular spectrum and comparisons with Williams' model. Then in Sec. 5.3., the results of model 3 without a plate are presented, with representations of the magnitude and phase of the angular spectrum, comparisons with Williams' model, along with discussions of the effect of inclusion or exclusion of evanescent waves and the boundary condition of constant pressure. Model 1, 2, and 3, will be compared with Williams' model, which implicitly compares the three models with each other, so this will not be done explicitly. Before presenting the results with plate, the Scholte-waves' representation in the transmission coefficient are discussed in Sec. 5.4., before the results and comparisons of the three models with a plate in the farfield of the source are presented in Sec. 5.5. In Sec. 5.6., the results when the plate is in the nearfield of the source, using Waag's transmission setup, are discussed. Finally, the influence of a finite receiver is discussed, both with and without a plate, in Sec. 5.7.

5.1 Model 1: Without Plate

5.1.1 Magnitude and phase of the angular spectrum

The magnitude of the angular spectrum of model 1, Eq. (2.21), at two distances are almost identical. In Fig. 5.1., the magnitude of the angular spectrum without plate, $T(\eta, d) = 1$, at the distances $z = 200\,\text{mm}$ and $z = 1000\,\text{mm}$ with frequency $f = 500\,\text{kHz}$ are presented.

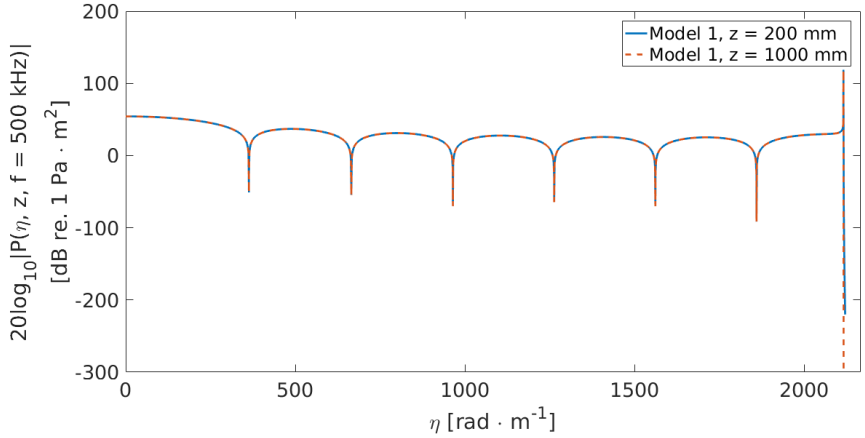

Figure 5.1: The calculated $|P(\eta, z, f = 500\text{kHz})|$ for the distances $z = 200\,\text{mm}$ and $z = 1000\,\text{mm}$ at a frequency $f = 500\,\text{kHz}$. $h_f a = 22$.

The spectrum is truncated at approximately the point when it is less than 200 dB as explained in Sec. 3.2.1. The minima are caused by the directivity function becoming approximately zero. The only change between the two magnitudes, is with the evanescent part, which decays faster with respect to η as z increases. A closer look on the evanescent part is shown in Fig. 5.2. to highlight the differences.

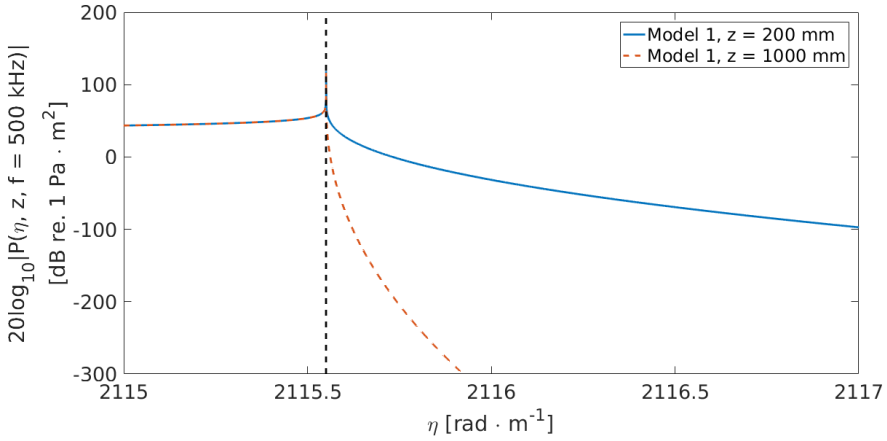

Figure 5.2: Zoomed in on the evanescent part in Fig. 5.1. The black dotted line represents where $\eta = h_f$.

Because the magnitudes are almost equal, the change of spatial pressure at the two distances are due to a change of phase, which is very different for the two distances. In Fig. 5.3. the phase of the angular spectra at these two distances are presented.

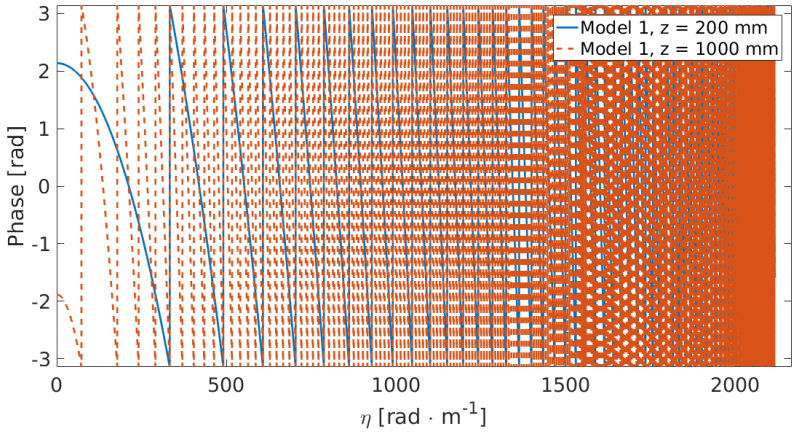

Figure 5.3: The phase of $P(\eta, z, f = 500\text{kHz})$ of model 1 without plate simulated for the distances $z = 200\,\text{mm}$ and $1000\,\text{mm}$ at a frequency $f = 500\,\text{kHz}$. $h_f a = 22$.

A larger z introduces a faster rate of change in the phase with respect to η. If looking at the phase-term, $h_{f,z} z$, and differentiating with respect

to η, it becomes

$$\frac{\partial h_{f,z} z}{\partial \eta} = -\frac{\eta z}{h_{f,z}}, \tag{5.1}$$

which means that the rate of change in the phase is proportional to $-\eta z$ and therefore decays faster when the product increases, if $\eta < h_f$. When $\eta > h_{f,z}$ the phase jumps to $\pm\pi/2$ (because the angular spectrum becomes purely imaginary) depending on the sign of the directivity function in Eq. (2.21), which is illustrated in Fig. 5.4. where the phase from Fig. 5.3. is zoomed in on the transition where $\eta = h_f$.

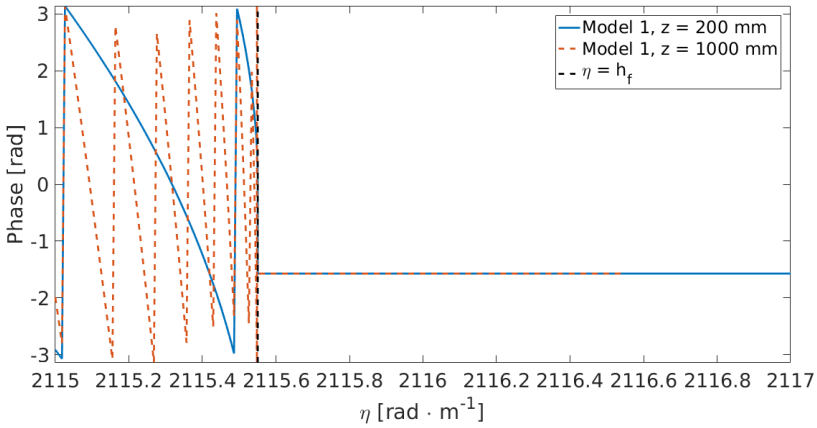

Figure 5.4: Zoomed in on the phase in Fig. 5.3., at the transition between $\eta \leq h_f$ and $\eta > h_f$. The black dotted line represents $\eta = h_f$.

At this frequency and distance, the evanescent part decays very fast, so the threshold limit is reached when η is just slightly bigger than h_f. This means that the sign of the directivity function does not change within this short range of $\eta > h_f$, but if the threshold limit for η_{max} is increased to e.g. 1000 dB, the variation of phase between $\pi/2$ and $-\pi/2$ in the evanescent part is clear. An illustration of this can be shown by increasing the threshold limit to 1000 dB and calculate the angular spectrum at $z = 200\,\text{mm}$ at $f = 500\,\text{kHz}$, see Fig. 5.5. This is just to illustrate the variation between $\pi/2$ and $-\pi/2$.

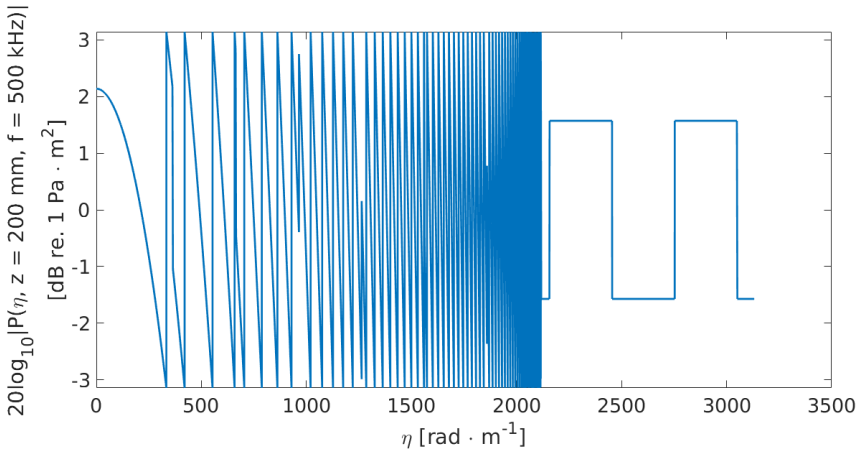

Figure 5.5: The phase of $P(\eta, z = 200\,\text{mm}, f = 500\text{kHz})$ when increasing η_{max}. The variation between $\pi/2$ and $-\pi/2$ as $\eta > h_f$ is clear.

As z increases, the transition between propagating and evanescent waves is harder to sample correctly, because of the fast rate of change in the phase and the fast decaying exponential term in the magnitude, which may introduce undersampling effects. This can however be resolved by introducing a small amount of losses in the fluid or increase the number of samples, but in order to keep computational efficiency, it's more convenient to introduce losses. If the amount of losses is very small, this compromise is worth implementing. The complex loss-factor dampens the oscillations making the transition to $\pm\pi/2$ in the phase smoother, while it also dampens the spike in the magnitude. In Fig. 5.6., the angular spectrum at $z = 200\,\text{mm}$ at the frequency $f = 500\,\text{kHz}$ is presented both with and without loss. The spike is clearly dampened down, while the effect of loss in the magnitude for the rest of the spectrum is of negligible difference compared to the lossless case. In Fig. 5.7., the phase for the angular spectra of Fig. 5.4. are shown at the transition when $\eta = h_f$.

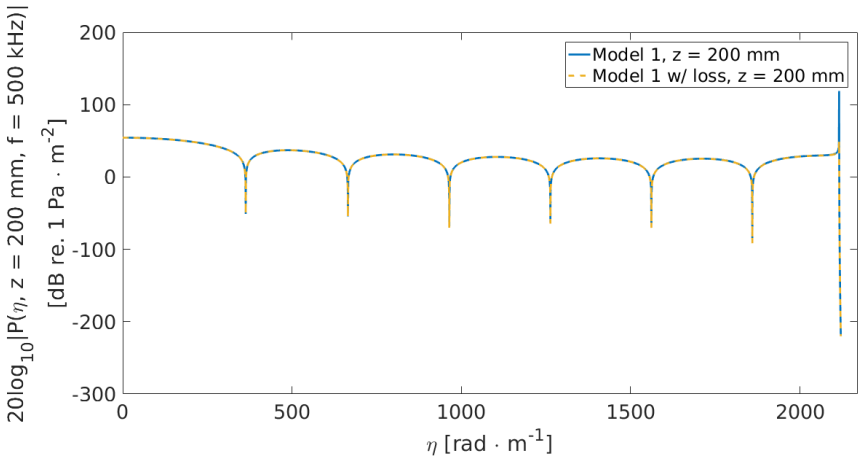

Figure 5.6: The magnitude $|P(\eta, z = 200\,\text{mm}, f = 500\text{kHz})|$ at $z = 200\,\text{mm}$ at the frequency $f = 500\,\text{kHz}$ with and without loss. $h_f a = 22$.

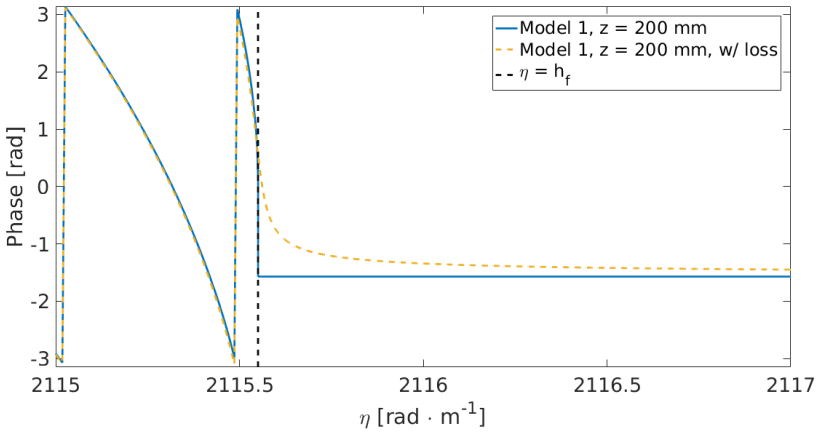

Figure 5.7: The phase of $P(\eta, z = 200\,\text{mm}, f = 500\text{kHz})$ at $z = 200\,\text{mm}$ at the frequency $f = 500\,\text{kHz}$ with and without loss. The black dotted line represents the point when $\eta = h_f$.

The transition into the evanescent part is smoother, and therefore easier to sample. This is convenient to exploit if the distances are very large. An example of the spatial pressure with losses is shown in Sec. 5.1.2., Fig. 5.17.

5.1.2 Comparisons with additional models

As mentioned in section 2.1, model 1 can be used to find the on-axis pressure with a point receiver by letting the receiver radius b go towards zero in Eq. (2.29). If $T(\eta, d) = 1$, model 1 can then be compared with the on-axis expression for a point receiver by Kinsler et al. defined in Sec. 2.4.2., Eq. (2.76), which is shown in Fig. 5.8. at $f = 500\,\text{kHz}$ as a function of distance to $z = 120\,\text{mm}$. The Rayleigh-distance is approximately $R_A = 110\,\text{mm}$.

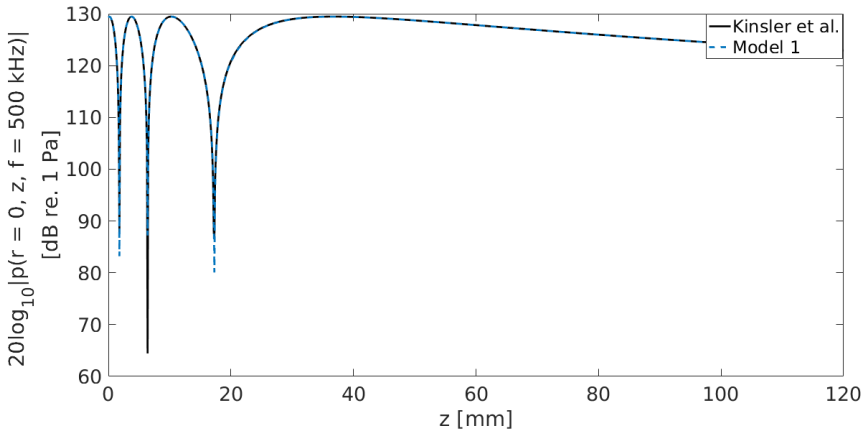

Figure 5.8: Model 1 compared to Kinsler et al.' model simulated as a function of distance to $z = 120\,\text{mm}$ at frequency $f = 500\,\text{kHz}$. The Rayleigh-distance is approximately $R_A = 110\,\text{mm}$. $h_f a = 22$.

They produce similar results, but with some differences in the minimums. In Figs. 5.9 and 5.10 model 1 is compared to Kinsler et al. at the frequencies $f = 40\,\text{kHz}$ and $f = 1000\,\text{kHz}$, respectively, as a function of distance. These frequencies were simply chosen to show a bigger range of frequencies, where 40 kHz represents a low frequency, and 1000 kHz represents a high frequency.

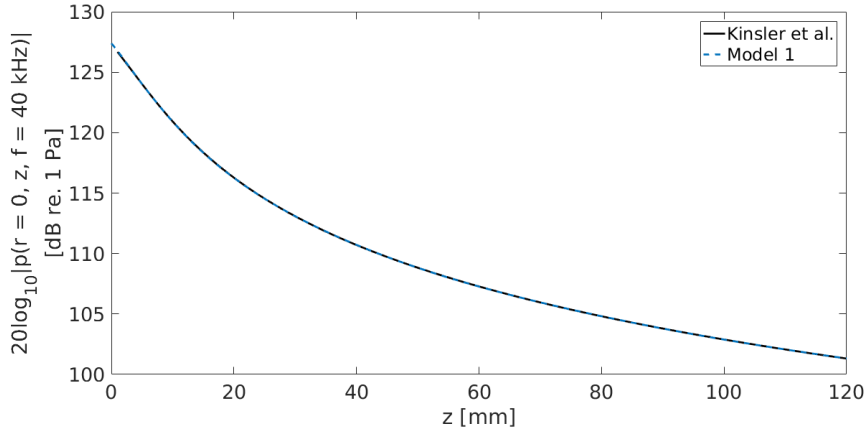

Figure 5.9: Model 1 compared with Kinsler et al.' model simulated as a function of distance to $z = 120\,\text{mm}$ at frequency $f = 40\,\text{kHz}$. The Rayleigh-distance is approximately $R_A = 9\,\text{mm}$. $h_f a = 2$

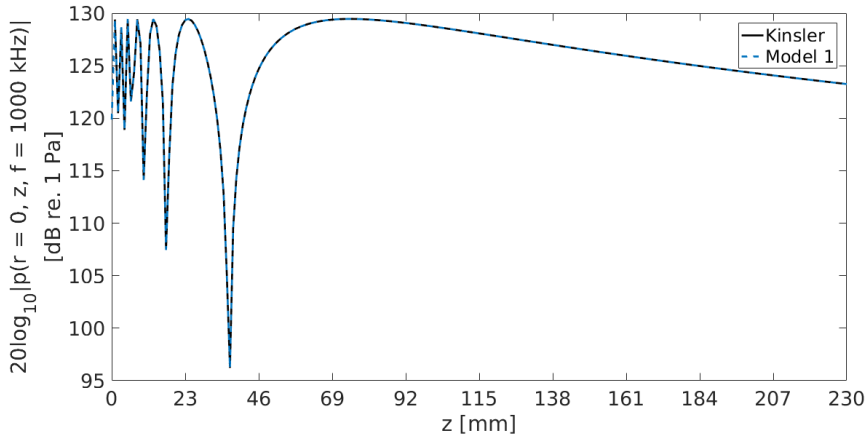

Figure 5.10: Model 1 compared with Kinsler et al.' model simulated as a function of distance to $z = 230\,\text{mm}$ at frequency $f = 1000\,\text{kHz}$. The Rayleigh-distance is approximately $R_A = 220\,\text{mm}$. $h_f a = 45$.

In figure 5.11, the magnitude of model 1 with a finite receiver $b = 10.55\,\text{mm}$, is compared with the magnitude of Williams' model, Eq. 2.75, as a function of distance to $z = 120\,\text{mm}$ at $f = 500\,\text{kHz}$.

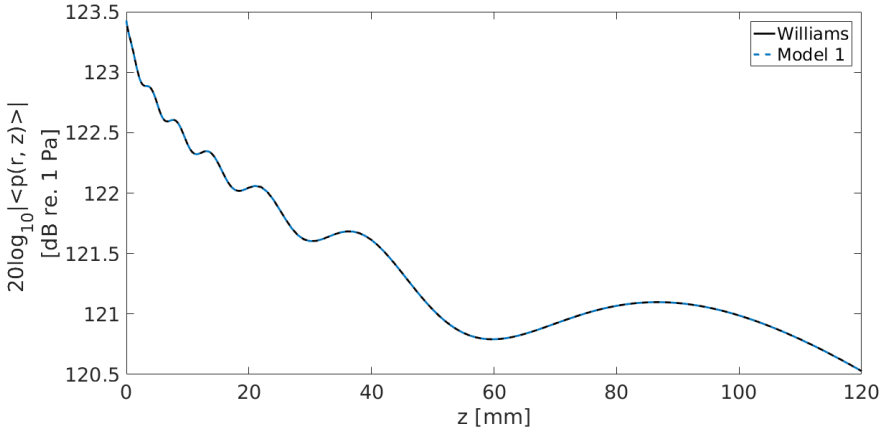

Figure 5.11: The magnitudes of model 1 and Williams' model simulated as a function of distance to $z = 120\,\text{mm}$ with frequency $f = 500\,\text{kHz}$. $h_f a = 22$.

In Fig. 5.12. the phase of the models are plotted.

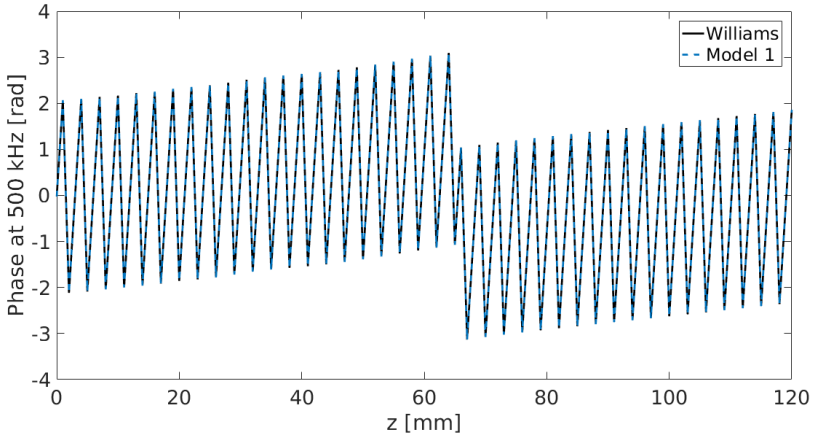

Figure 5.12: The phases of model 1 and Williams' model simulated as a function of distance to $z = 120\,\text{mm}$ with frequency $f = 500\,\text{kHz}$. $h_f a = 22$.

The reason that the phase does not vary between $-\pi$ and π is because of the stepsize of the distance. 1 mm was used, but the models still produce the same results, which is the important attribute. In order for the phase to be correct, a simulation with $\Delta z = 0.1\,\text{mm}$ was run, but both the models still did not vary consistently between $-\pi$ and π.

This was therefore neglected as this would require simulations for all the models running over a very long period of time. Again, in order to show a bigger frequency range, model 1 calculated with the frequencies $f = 40\,\text{kHz}$ as a function of distance to $z = 120\,\text{mm}$ are compared with Williams' model in Fig. 5.13. where the phase is given in Fig. 5.14.

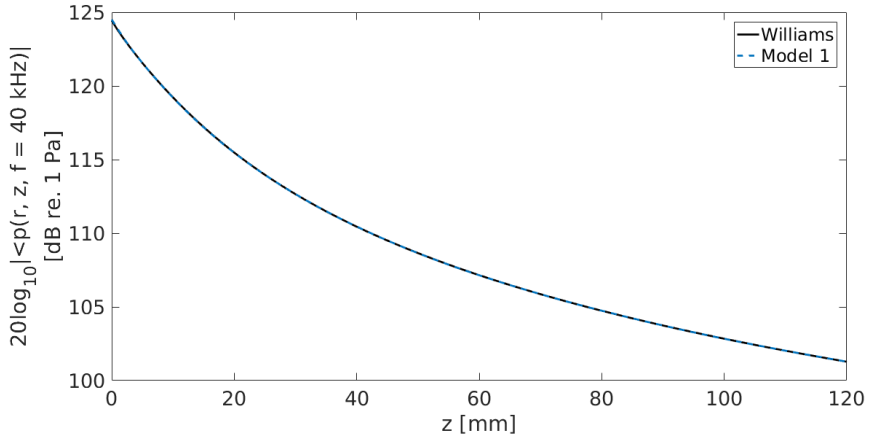

Figure 5.13: The magnitudes of model 1 and Williams' model simulated as a function of distance to $z = 120\,\text{mm}$ with frequency $f = 40\,\text{kHz}$. $h_f a = 2$

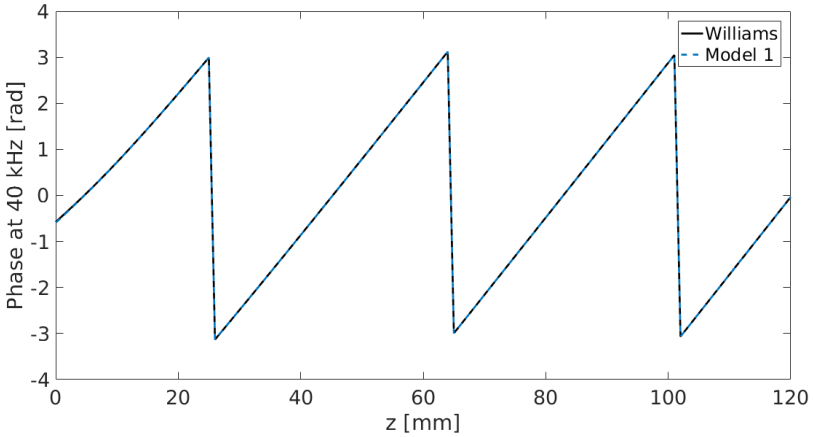

Figure 5.14: The phase of model 1 and Williams' model simulated as a function of distance to $z = 120\,\text{mm}$ with frequency $f = 40\,\text{kHz}$. $h_f a = 2$

In Fig. 5.15., the magnitudes of model 1 and Williams' model have been

calculated as a function of distance to $z = 500\,\text{mm}$ with $f = 1000\,\text{kHz}$. The phase of the models are shown in Fig. 5.16.

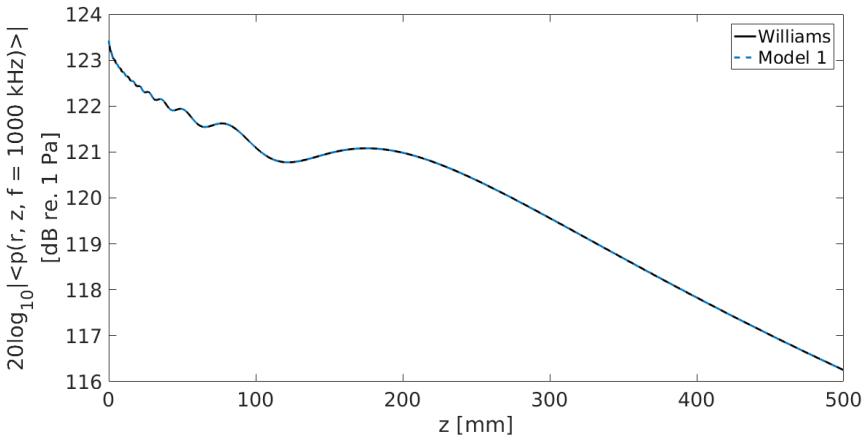

Figure 5.15: The magnitudes of model 1 and Williams' model simulated as a function of distance to $z = 500\,\text{mm}$ with frequency $f = 1000\,\text{kHz}$. $h_f a = 45$

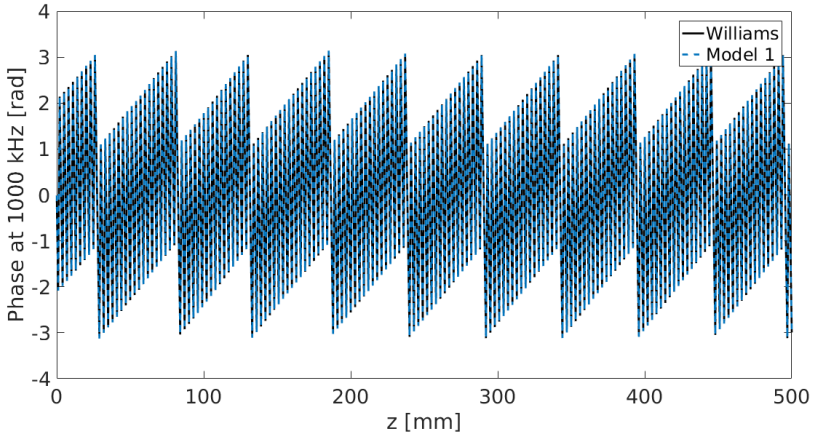

Figure 5.16: The phases of model 1 and Williams' model simulated as a function of distance to $z = 500\,\text{mm}$ with frequency $f = 1000\,\text{kHz}$. $h_f a = 45$

At the three frequencies, model 1 produce the same results as Williams' model.

In Sec. 2.8., the absorption coefficient was shown to be proportional to the frequency, which means that for the frequency range in the present

study, the maximum loss will be at $f = 1000\,\text{kHz}$. To illustrate the amount of losses introduced with a Q-factor $Q_f = 50 \cdot 10^3$, a simulation with losses in model 1 compared to Williams' model without losses, as a function of distance to $z = 500\,\text{mm}$ with the frequency $f = 1000\,\text{kHz}$ is shown in Fig. 5.17.

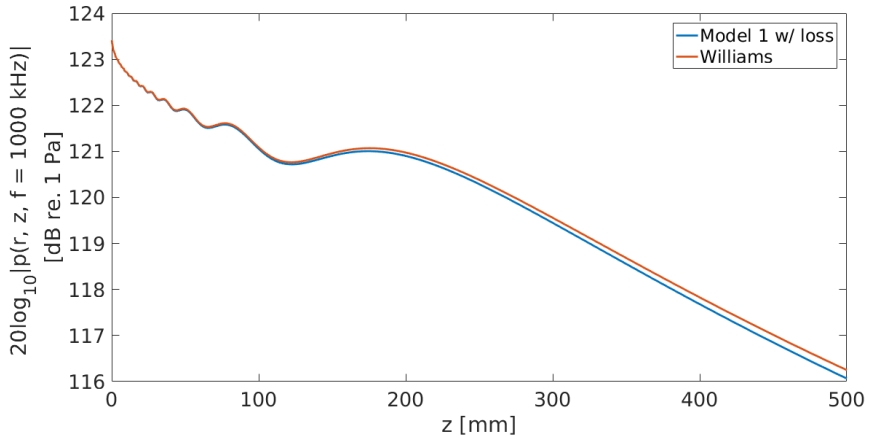

Figure 5.17: Model 3 when using losses compared with Williams' model which is lossless at $f = 1000\,\text{kHz}$.

The difference in dB at 500 mm is approximately 0.2 dB. In other words, the difference will be even smaller for lower frequencies and distances.

5.1.3 The effect of evanescent waves

Because model 3 neglects evanescent waves, which is also a model for the normal particle velocity, it is of interest to see this effect in model 1 because it represents pressure. Using model 1 with a finite receiver and without a plate, but excluding evanescent waves, the pressure as a function of distance at $f = 500\,\text{kHz}$ is compared in Fig. 5.18.

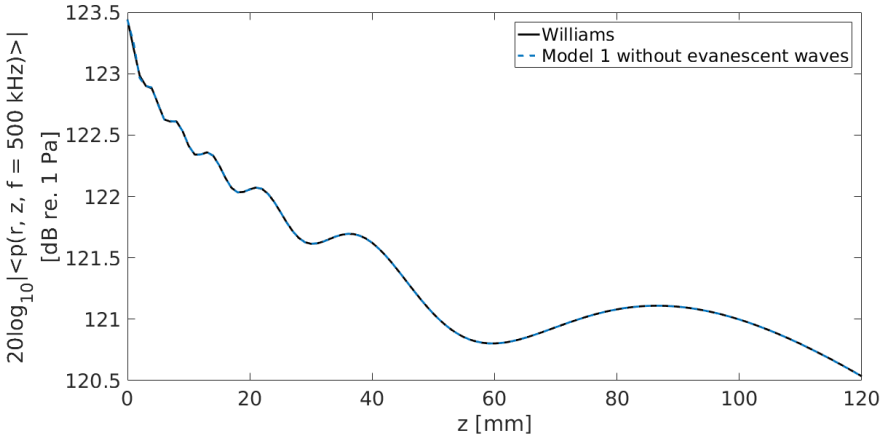

Figure 5.18: Model 1 as a function of distance to $z = 120\,\text{mm}$, excluding evanescent waves, compared with Williams' model at $f = 500\,\text{kHz}$. $h_f a = 22$.

Overall they both match, but close to the source $z \leq 10\,\text{mm}$, there is less agreement, see Fig. 5.19. for a closer look.

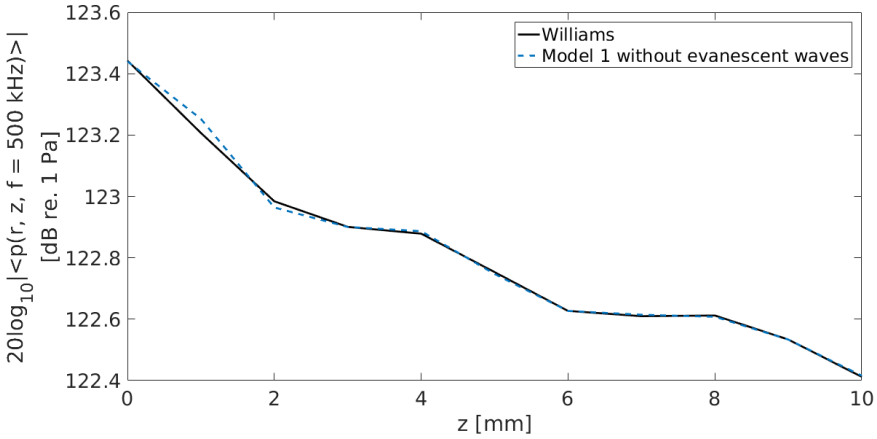

Figure 5.19: Zoomed in on the nearfield of Fig. 5.18.

The cause of this is clear if looking at the angular spectrum at, e.g., $z = 3\,\text{mm}$ when evanescent waves are included and when they are excluded, see Fig. 5.20.

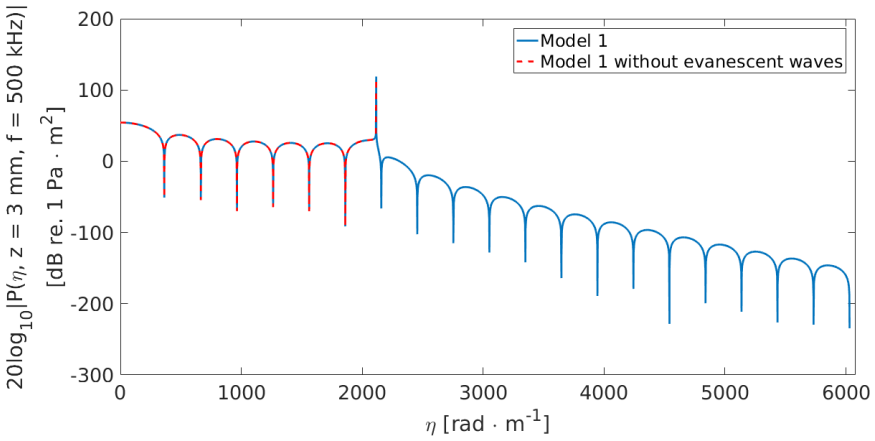

Figure 5.20: The magnitude of the angular spectrum $|P(\eta, z = 3\,\text{mm}, f = 500\,\text{kHz})|$ of model 1 at $z = 3\text{mm}$ with frequency $f = 500\,\text{kHz}$, with and without evanescent waves. $h_f a = 22$.

Just as η is slightly bigger than h_f, the evanescent waves have a significant magnitude which influences the integration. If left out, the spatial pressure will be undersampled and incorrect in the nearfield, as seen in Fig. 5.19. This effect is even more significant at the frequency $f = 40\,\text{kHz}$, if calculating model 1 as a function of distance $z = 120\,\text{mm}$ with frequency $f = 40\,\text{kHz}$ and compared with Williams' model, see Fig. 5.21.

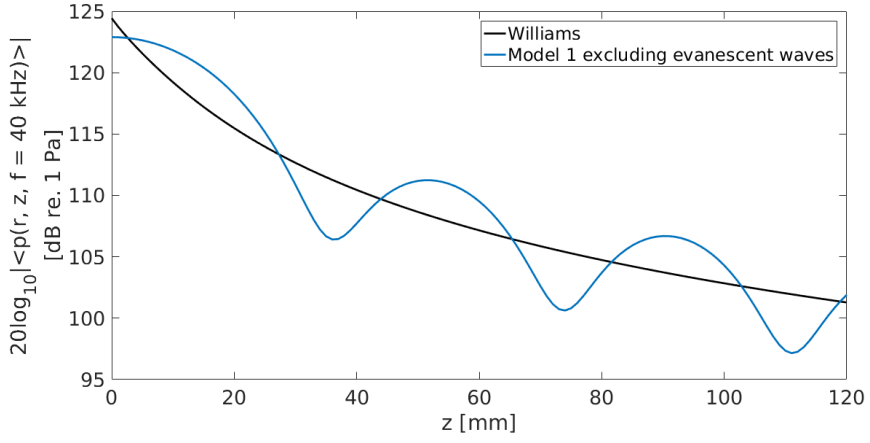

Figure 5.21: The magnitude of model 1 as a function of distance to $z = 120\,\text{mm}$, excluding evanescent waves, compared with the magnitude of Williams' model at $f = 40\,\text{kHz}$. $h_f a = 2$.

There is a great deviance between the two. This is also evident if comparing the phases, see Fig. 5.22.

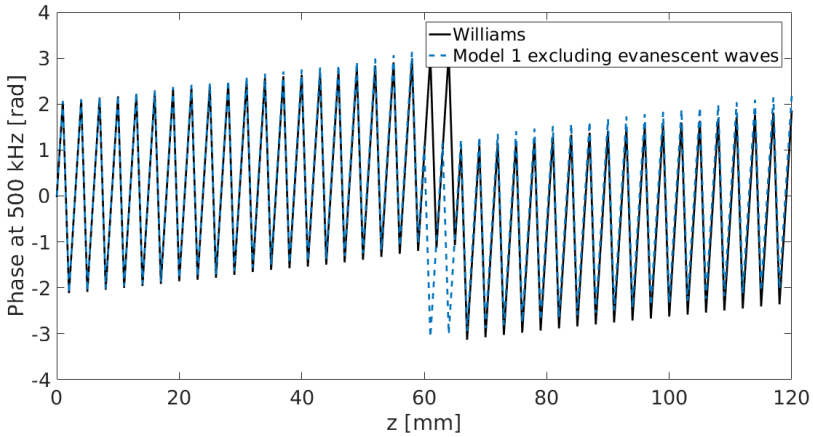

Figure 5.22: The phases of model 1 and Williams' model as a function of distance to $z = 120\,\text{mm}$, when excluding evanescent waves in model 1, at $f = 40\,\text{kHz}$. $h_f a = 2$.

The exclusion of evanescent waves at $f = 40\,\text{kHz}$ is not a good approximation, and again the reason can be explained by looking at the angular spectrum. In Fig. 5.23., the magnitude of the angular spectrum is calculated for $f = 40\,\text{kHz}$ at a distance of $z = 100\,\text{mm}$.

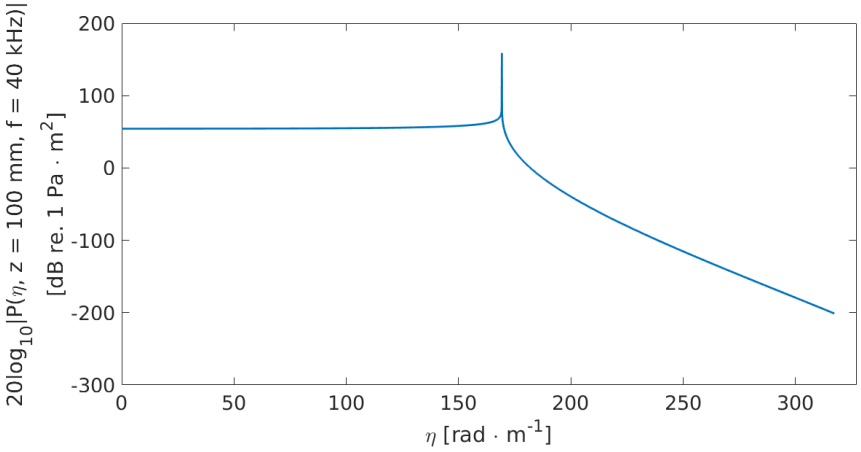

Figure 5.23: The magnitude of the angular spectrum $|P(\eta, z = 100\,\text{mm}, f = 40\,\text{kHz})|$ of model 1 at $z = 100\text{mm}$ with frequency $f = 40\,\text{kHz}$.

When $\eta > h_f$ the evanescent part is significant if compared with the magnitude of the propagating part, which will affect the spatial integration and therefore cause undersampling effects.

Model 1 produces the same results as analytical models, in the nearfield and farfield, without plate. It was also seen that the exclusion of evanescent waves is not a good approximation for low frequencies. This was due to the significance of evanescent waves just as η is slightly bigger than h_f, which is a phenomenon for the pressure ASM models, i.e., for model 1 and 2. This will therefore not be studied using model 2 in Sec. 5.2.

5.2 Model 2: Without plate

5.2.1 Magnitude and phase of the angular spectrum

In Fig. 5.24. an incision of the magnitude of the angular spectrum, Eq. (2.33), at the axis of $h_{f,x}$ where $h_{f,y} = 0$ is plotted for a frequency of $f = 500\,\text{kHz}$ at $z = 200\,\text{mm}$ and $z = 1000\,\text{mm}$ without plate.

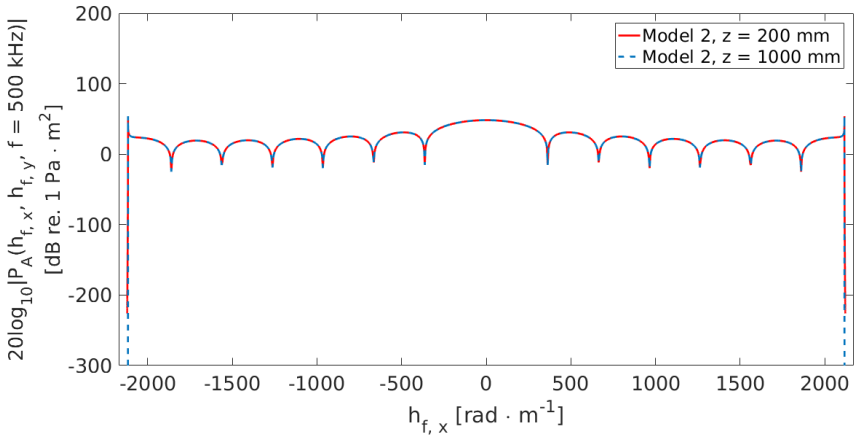

Figure 5.24: The magnitude of the angular spectrum $|P_A(h_{f,x}, h_{f,y} = 0, z, f = 500\,\text{kHz})|$ of model 2 with frequency $f = 500\,\text{kHz}$ at $z = 200\,\text{mm}$ and $z = 1000\,\text{mm}$. $h_f a = 22$.

Notice that compared with model 1, the spike at $h_{f,x} = h_f$ are not as good sampled. This is because of the limitations in number of samples

as mentioned in Sec. 3.3.2. An example of the phase of the angular spectrum of model 2, can be seen in Fig. 5.25., which was calculated with frequency $f = 500\,\text{kHz}$ at $z = 200\,\text{mm}$.

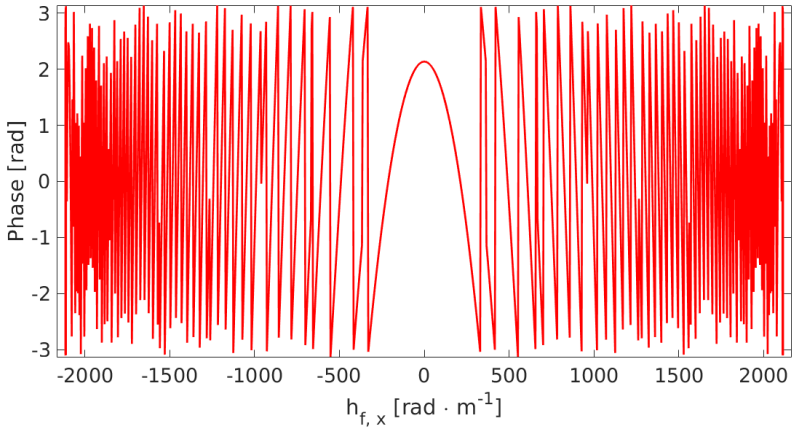

Figure 5.25: The phase of the angular spectrum $P_A(h_{f,x}, h_{f,y} = 0, z = 200\,\text{mm}, f = 500\,\text{kHz})$ of model 2 with frequency $f = 500\,\text{kHz}$ at $z = 200\,\text{mm}$. $h_f a = 22$.

The phase is also subjected to undersampling effects as the rate of change increases.

5.2.2 Comparisons with additional models

In figure 5.26, model 2 Eq. (2.32) with $T(h_{f,x}, h_{f,y}, d, f) = 1$, and Williams' model Eq. (2.75), have been calculated with $f = 500\,\text{kHz}$ as a function of distance to $z = 120\,\text{mm}$, and there is a magnitude difference. Also note that the unit of the pressure is wrong. This is because of the factor missing from model 2, as stated in Sec. 2.2., which was calculated to be $4/\pi v_0 a^2$. Multiplying model 2 with the missing factor gives the plot in figure 5.27.

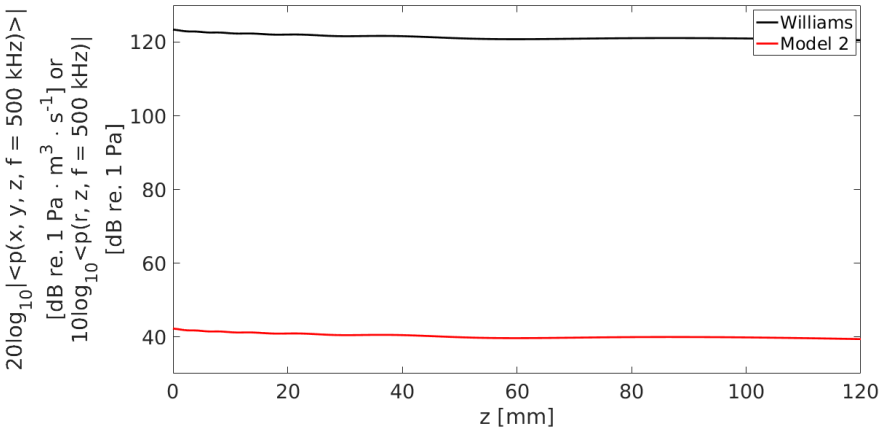

Figure 5.26: Model 2 without plate compared with Williams' model, simulated with frequency $f = 500\,\text{kHz}$ as a function of distance to $z = 120\,\text{mm}$. $h_f a = 22$.

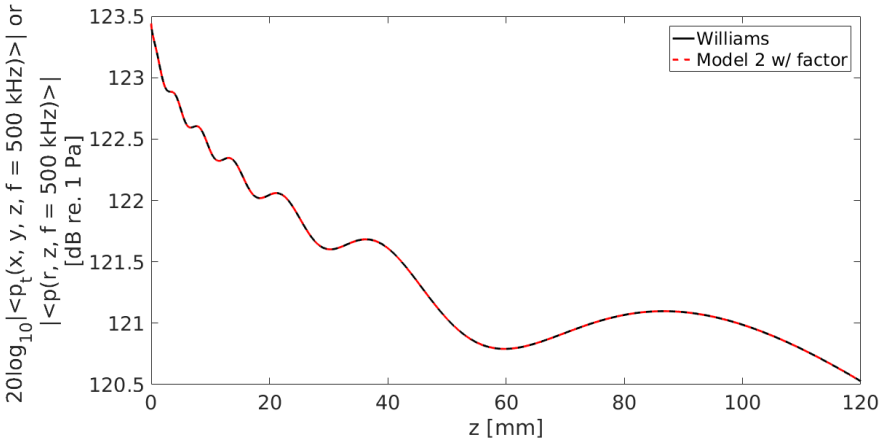

Figure 5.27: Model 2 mulitplied with missing factor compared with Williams' model, simulated with frequency $f = 500\,\text{kHz}$ as a function of distance to $z = 120\,\text{mm}$

The phase at $f = 500\,\text{kHz}$ of the two models are compared in Fig. 5.28.

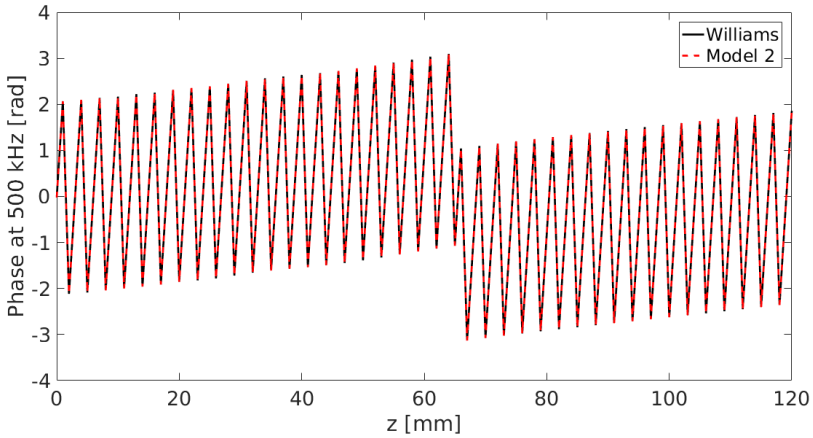

Figure 5.28: The phases of model 2 and Williams' model, simulated with frequency $f = 500\,\text{kHz}$ as a function of distance to $z = 120\,\text{mm}$.

For consistency, model 2 mulitplied with missing factor is compared with Williams' model for the frequency $f = 40\,\text{kHz}$ in Fig. 5.29., as a function of distance to $z = 120\,\text{mm}$. The simulation have multiplied with the missing factor.

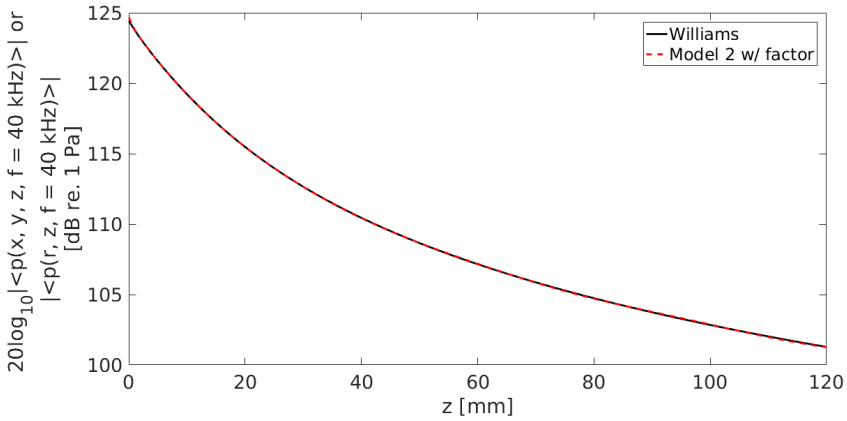

Figure 5.29: Model 2 multiplied with missing factor compared with Williams' model, simulated as a function of distance to $z = 120\,\text{mm}$ with frequency $f = 40\,\text{kHz}$. $h_f a = 2$.

The phase at $f = 40\,\text{kHz}$ for the two models are presented in Fig. 5.30.

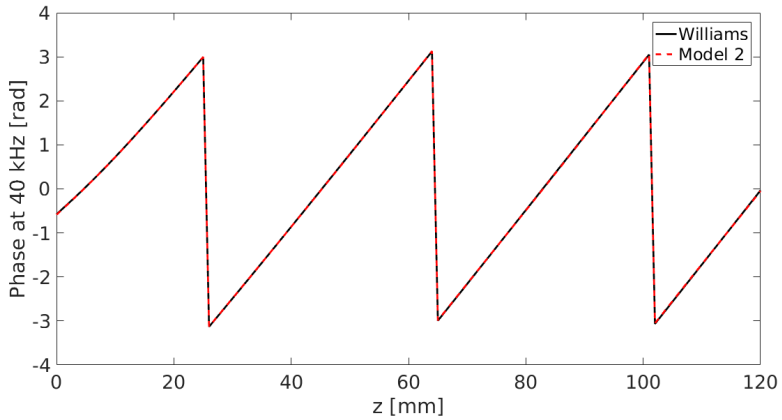

Figure 5.30: The phases of model 2 and Williams' model, simulated as a function of distance with frequency $f = 40\,\text{kHz}$. $h_f a = 2$.

What is perhaps a bit difficult to see in Fig. 5.29. is that as the distance increases, some undersampling effects starts to appear. If extending the distance to $z = 150\,\text{mm}$ and zooming in, the effects are more visible, see Fig. 5.31.

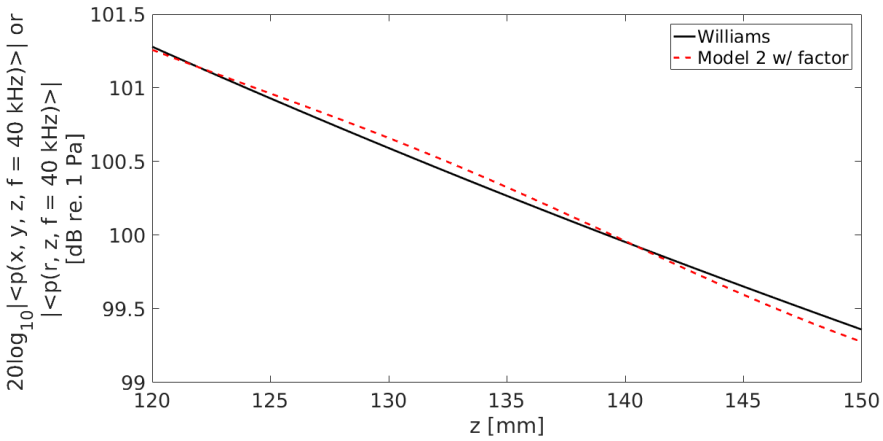

Figure 5.31: Model 2 with missing factor compared with Williams' model, simulated as a function of distance with frequency $f = 40\,\text{kHz}$ for a distance between 100 mm and 150 mm.

These deviances are very small, but for greater distances they may be more significant, which will be shown in Sec. 5.5.. The undersampling effects are a result of the limit in number of samples as stated in Sec.

3.3.2. At this frequency, the evanescent part is crucial to sample with enough samples, which was also seen in Sec. 5.1.3. In Fig. 5.32., model 2 with missing factor is compared with Williams' model at $f = 1000\,\text{kHz}$. The phase at $f = 1000\,\text{kHz}$ for the two models are plotted in Fig. 5.33. Apart from the missing factor, model 2 produce the same results as Williams' model, however, model 2 has some limitations in terms of number of samples and computational efficiency, because it is a three-dimensional description.

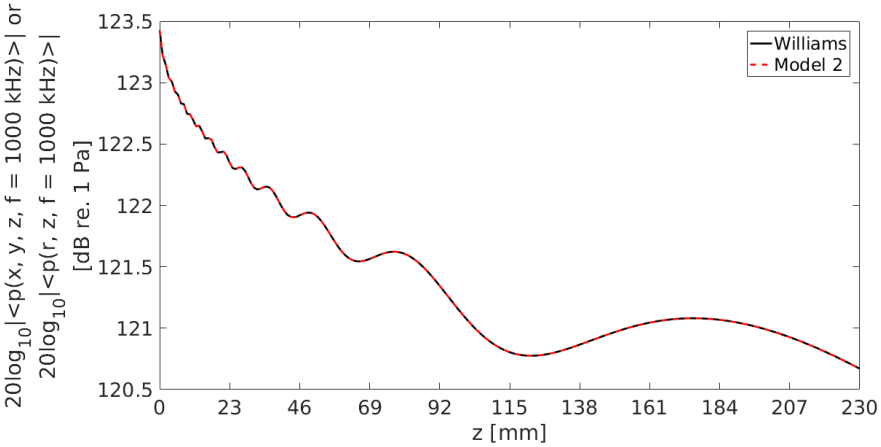

Figure 5.32: Model 2 multiplied with missing factor compared with Williams' model, simulated as a function of distance to $z = 230\,\text{mm}$ with frequency $f = 1000\,\text{kHz}$. $h_f a = 45$.

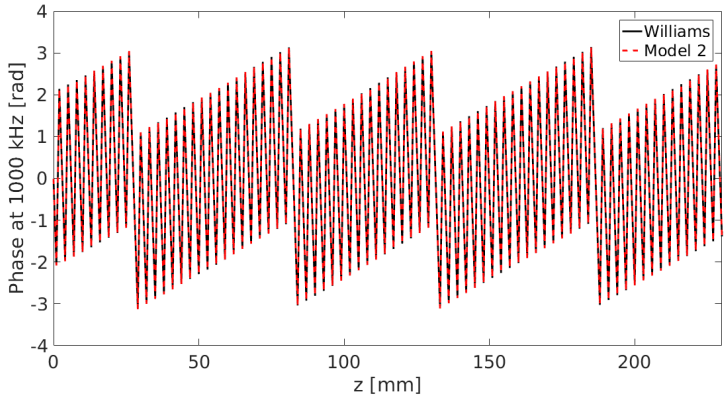

Figure 5.33: The phases of model 2 and Williams' model, simulated as a function of distance to $z = 230\,\text{mm}$ with frequency $f = 40\,\text{kHz}$. $h_f a = 45$.

5.3 Model 3: Without plate

5.3.1 Magnitude and phase of the angular spectrum

The magnitude of the angular spectrum of model 3 without plate, Eq. (2.57) with $T(\theta_f, d) = 1$, at the distance $z = 200\,\text{mm}$ with frequency $f = 500\,\text{kHz}$ is compared with the same case when including evanescent waves (modified model 3), are presented in Fig. 5.34.

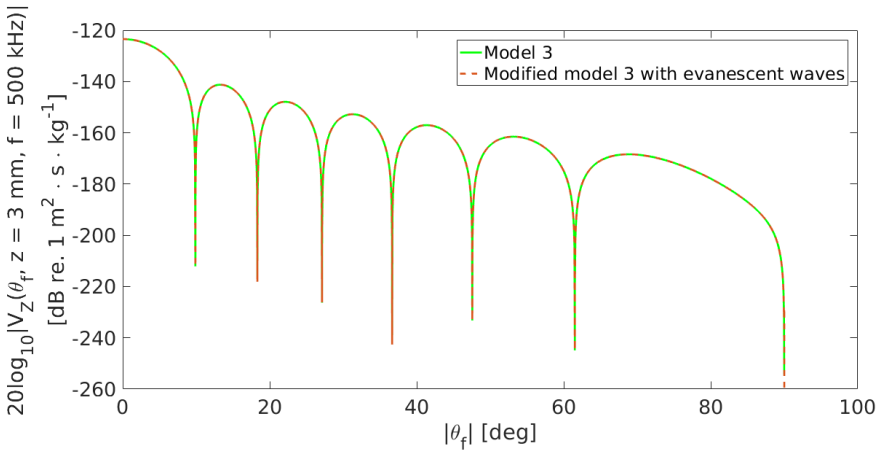

Figure 5.34: The magnitude of the angular spectrum $|V_Z(\theta_f, z = 200\,\text{mm}, f = 500\,\text{kHz})|$ of model 3 and modified model 3, at the distance $z = 200\,\text{mm}$ with frequency $f = 500\,\text{kHz}$. $h_f a = 22$.

The unit should be $\text{m}^4 \cdot \text{s} \cdot \text{kg}^{-1}$, but because of the missing πa^2 term in the aperture function, as stated in Sec. 2.3., the unit is incorrect. The phase of the angular spectra in Fig. 5.34. are shown in Fig. 5.35. See Sec. 5.1.1. for comparisons with the angular spectrum and phase of model 1. The phase of the plane-wave component of model 1 in Fig. 5.3. is equal to the plane-wave component in Fig. 5.35., which means that the plane-wave pressure and plane-wave particle velocity are in phase with each other. The spectrum of model 3 in Fig. 5.34. is truncated at $\theta_f = 90°$. The effect of the inverse impedance term of model 3 is clear as the spectrum goes toward 0 instead of infinity which was seen with model 1 and 2. When excluding evanescent waves, there is not much difference compared to when they're included in Fig. 5.34., which is due to the large distance and frequency. However, at

e.g. $z = 3\,\text{mm}$ at the same frequency, the significance of the evanescent waves may be higher. In Fig. 5.36. the angular spectrum of model 3 at the distance $z = 3\,\text{mm}$ with frequency $f = 500\,\text{kHz}$ is compared to the same case when including evanescent waves. The magnitude of the evanescent waves are relatively low compared to the rest of the spectrum and in Sec. 5.3.3. this will be shown to not matter for the spatial values if excluding the evanescent part.

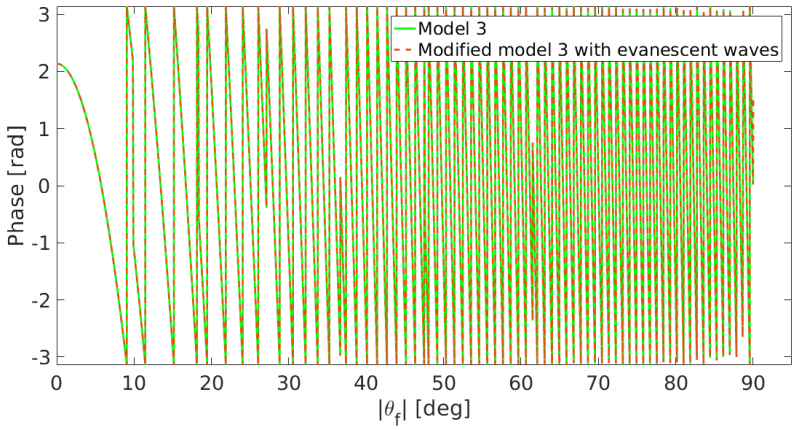

Figure 5.35: The phase of the angular spectrum $V_Z(\theta_f, z = 200\,\text{mm}, f = 500\,\text{kHz})$ presented in Fig. 5.34. $h_f a = 22$.

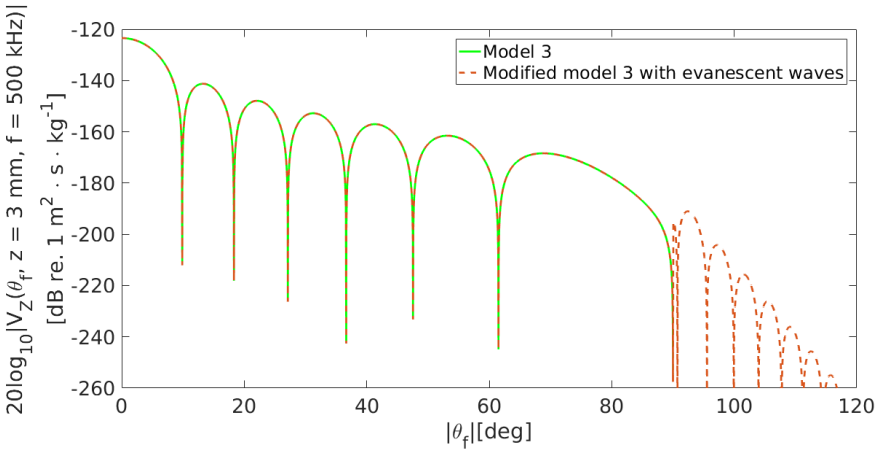

Figure 5.36: The magnitude of the angular spectrum $|V_Z(\theta_f, z = 3\,\text{mm}, f = 500\,\text{kHz})|$ of model 3 at the distance $z = 3\,\text{mm}$ with frequency $f = 500\,\text{kHz}$ compared with modified model 3 when including evanescent waves. $h_f a = 22$.

5.3.2 Comparison with Williams

In order to compare model 3 with Williams' model, a method is to do a normalization of the two models. In Fig. 5.37., model 3, Eq. (2.56) with $T(\theta_f, d) = 1$, have been calculated as a function of distance with frequency $f = 500\,\text{kHz}$, and normalized to it's value at $z = 120\,\text{mm}$. The same is done with Williams' model.

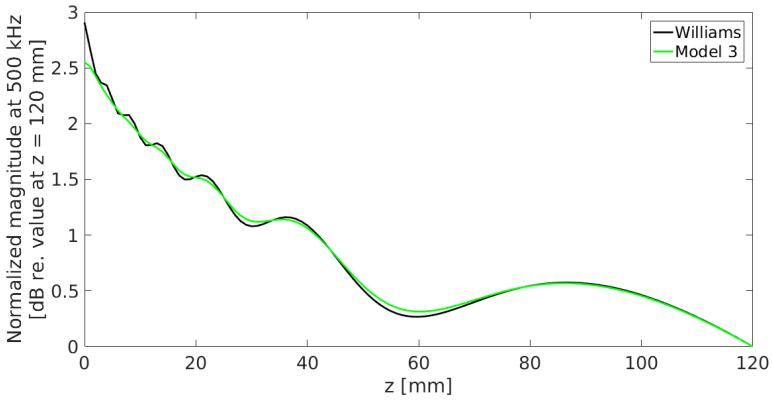

Figure 5.37: Model 3 compared with Williams' model as function of distance with frequency $f = 500\,\text{kHz}$. Both models are normalized with their values at $z = 120\,\text{mm}$. $h_f a = 22$.

The phase of the models at the same frequency and distance range are shown in Fig. 5.38.

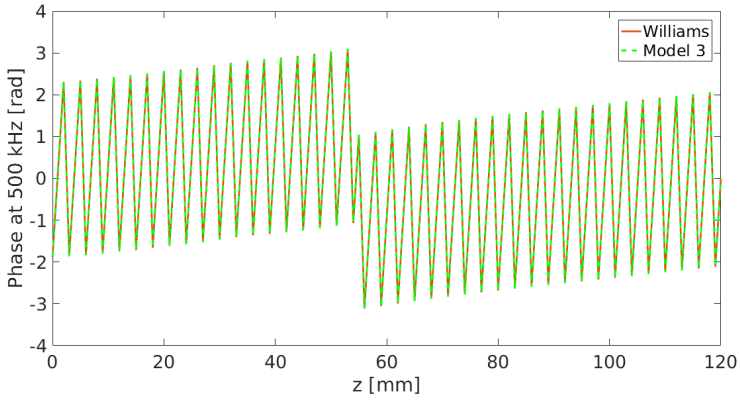

Figure 5.38: The phases of model 3 and Williams' model as function of distance with frequency $f = 500\,\text{kHz}$. Both models are normalized with their values at $z = 120\,\text{mm}$. $h_f a = 22$.

The phases match, but there are clear differences in magnitude in Fig. 5.37 in the nearfield, with more distinct interference effects for Williams' model, before it starts to decay as $1/z$. They converge towards the same value at $z = 120\,\text{mm}$, which is important to note when introducing the results including plate in Sec. 5.5. and Sec. 5.6. In Fig. 5.39., the two models are again compared through normalization with their respective values at $z = 120\,\text{mm}$, but at frequency $f = 40\,\text{kHz}$.

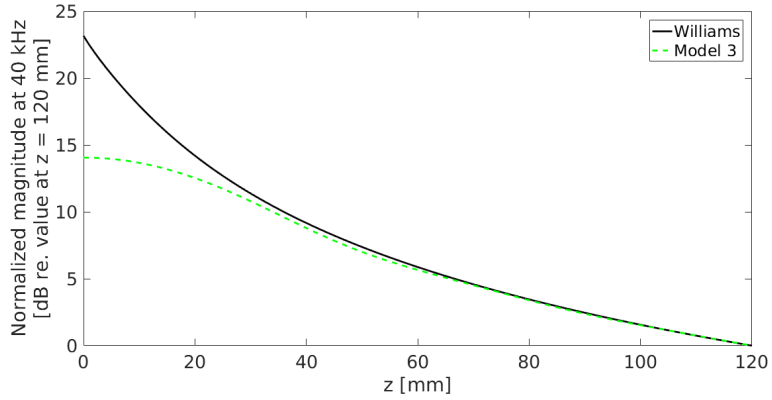

Figure 5.39: The magnitudes of model 3 compared with Williams as function of distance with frequency $f = 40\,\text{kHz}$. Both models are normalized with their values at $z = 120\,\text{mm}$. $h_f a = 2$.

The phase of the two models are shown in Fig. 5.40.

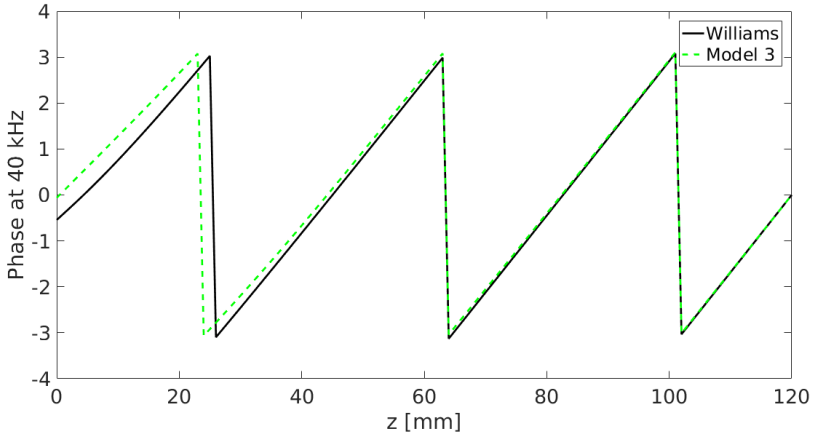

Figure 5.40: The phases of model 3 and Williams' model as function of distance with frequency $f = 40\,\text{kHz}$. Both models are normalized with their values at $z = 120\,\text{mm}$. $h_f a = 2$

The phases in Fig. 5.40. are different from one another, as opposed to the phases in e.g. Fig. 5.38. This may be caused by $h_f a \to 0$, where the baffled piston goes towards a point source, for which the consequence is that pressure and particle velocity becomes more out of phase in the nearfield [30]. Finally, the two models are compared through normalization with their respective values at $z = 500\,\text{mm}$ at frequency $f = 1000\,\text{kHz}$ in Fig. 5.41, with the respective phase in Fig. 5.42. At this frequency their dynamics are almost indistinguishable. These results will be important when introducing a plate and with the calculations of the transfer functions defined in Sec. 2.7.

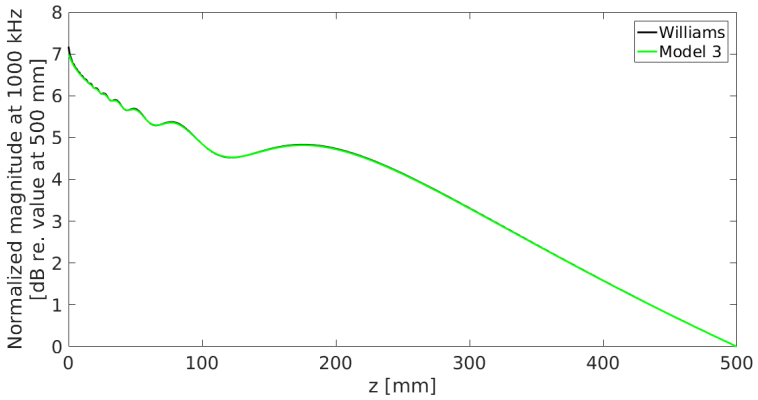

Figure 5.41: Model 3 compared with Williams' model as function of distance with frequency $f = 1000\,\text{kHz}$. Both models are normalized with their values at $z = 500\,\text{mm}$.

5.3.3 The inclusion or exclusion of evanescent waves

In Fig. 5.43. modified model 3 with evanescent waves and model 3 without evanescent waves at $f = 500\,\text{kHz}$ have been simulated as a function to a distance to $z = 120\,\text{mm}$, without plate.

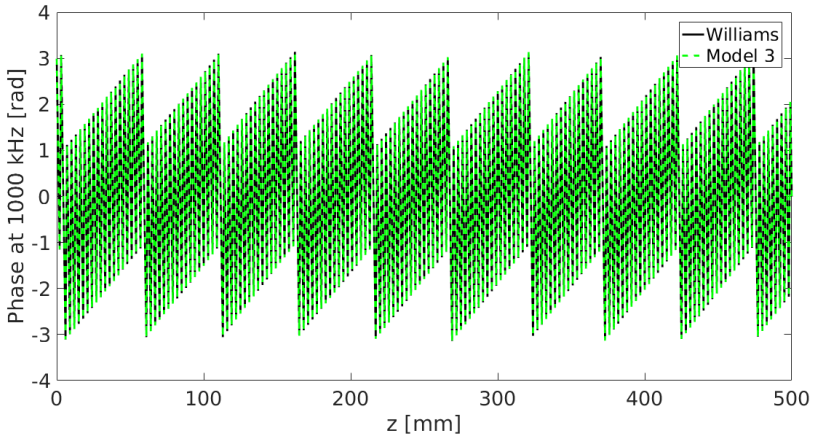

Figure 5.42: The phases of model 3 and Williams' model as function of distance with frequency $f = 1000\,\text{kHz}$. Both models are normalized with their values at $z = 500\,\text{mm}$.

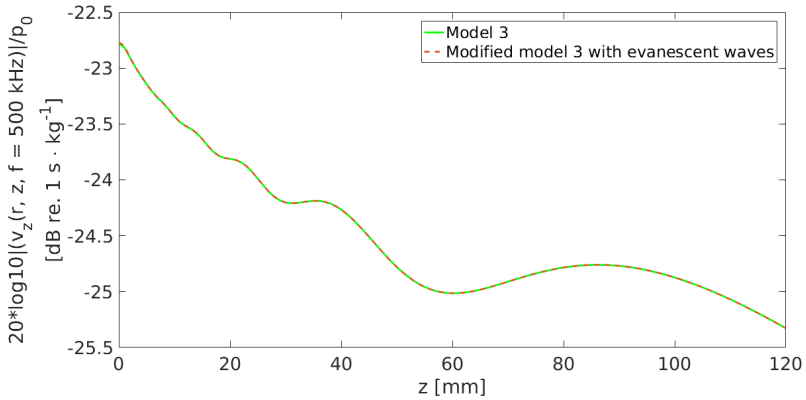

Figure 5.43: Model 3 without evanescent waves compared to modified model 3 with evanescent waves as a function of distance to $z = 120\,\text{mm}$ with $f = 500\,\text{kHz}$.

There is only slight deviance in the nearfield, which can be seen in Fig. 5.44.

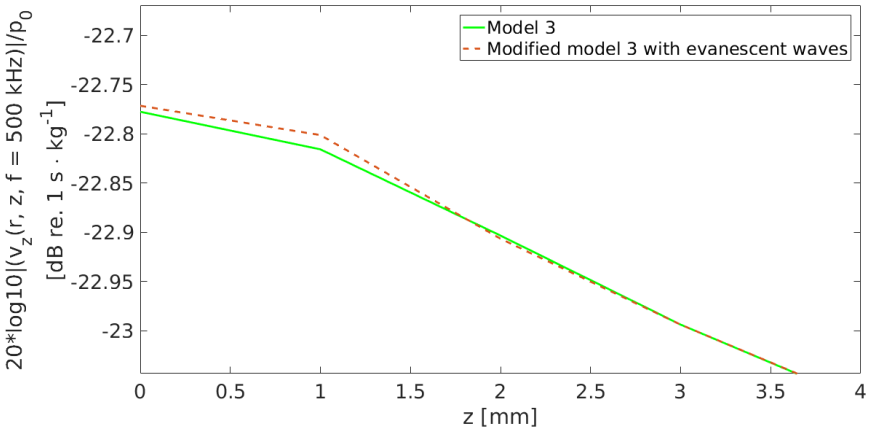

Figure 5.44: Zoomed in on the nearfield of Fig. 5.43.

Otherwise the two simulations are very similar. In Fig. 5.45. the same case has been simulated, but at a lower frequency, $f = 40\,\text{kHz}$, as a function of distance to $z = 120\,\text{mm}$.

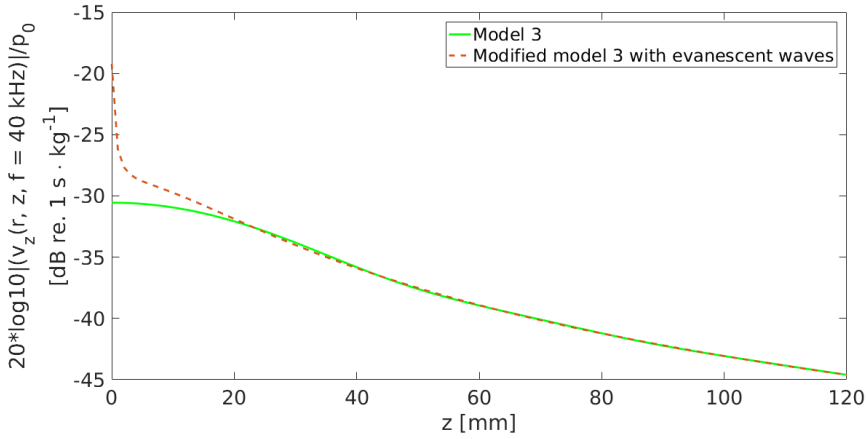

Figure 5.45: Model 3 without evanescent waves and modified model 3 with evanescent waves as function of distance to $z = 120\,\text{mm}$ with $f = 40\,\text{kHz}$. $h_f a = 2$

There is a significant difference in the nearfield, but further out in the field, the difference is small. In Fig. 5.46 the respective phases at the same frequency are plotted. Again there is a difference, but for lower distances compared to the magnitude. They become equal at approximately $z = 10\,\text{mm}$.

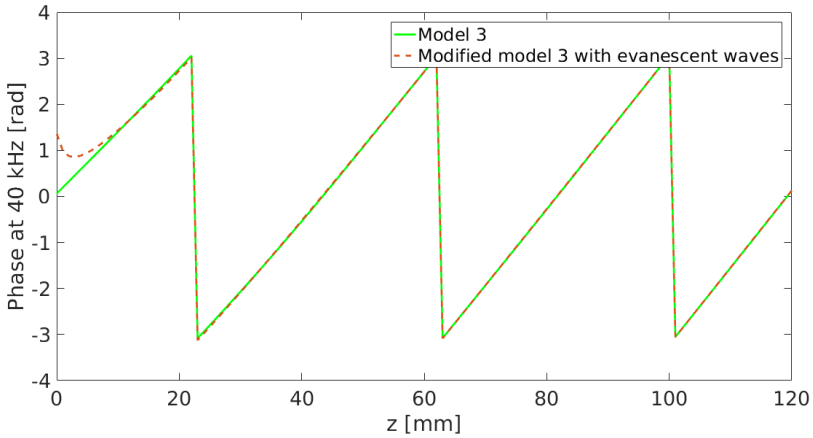

Figure 5.46: The phases of model 3 without evanescent waves and modified model 3 with evanescent waves as function of distance to $z = 120\,\text{mm}$ with $f = 40\,\text{kHz}$. $h_f a = 2$

In Sec. 5.1.3., it was shown that excluding evanescent waves in the angular spectrum of the pressure for low frequencies was a poor approximation. Interestingly, this not is necessarily true for model 3, i.e. particle velocity, in the farfield, which seems to be caused by the inverse impedance relationship when compared to pressure, which in turn does not influence the spatial integration. In Fig. 5.47., the magnitude of the angular spectrum of modified model 3 with frequency $f = 40\,\text{kHz}$ at distance $z = 100\,\text{mm}$ is plotted. The evanescent part just after $|\theta_f| > 90°$ is not as significant as with the pressure shown in Sec. 5.1.3., Fig. 5.23., because of the inverse impedance term. However, in in Fig. 5.48. the angular spectrum of modified model 3 have been calculated at the distance $z = 3\,\text{mm}$ with frequency $f = 40\,\text{kHz}$. The evanescent part has approximately the same magnitude as the propagating part. Ergo, leaving this out will cause the difference shown in Fig. 5.45.

5.3.4 Validity of constant pressure as boundary condition

Model 3 uses a constant pressure as a boundary condition for the baffled piston model, which is unusual, as the boundary condition for the baffled piston model usually is constant velocity [32], [30], [38], [21]. Younghouse [16] also used a constant pressure as boundary condition in the derivation of an angular spectrum model based on the baffled

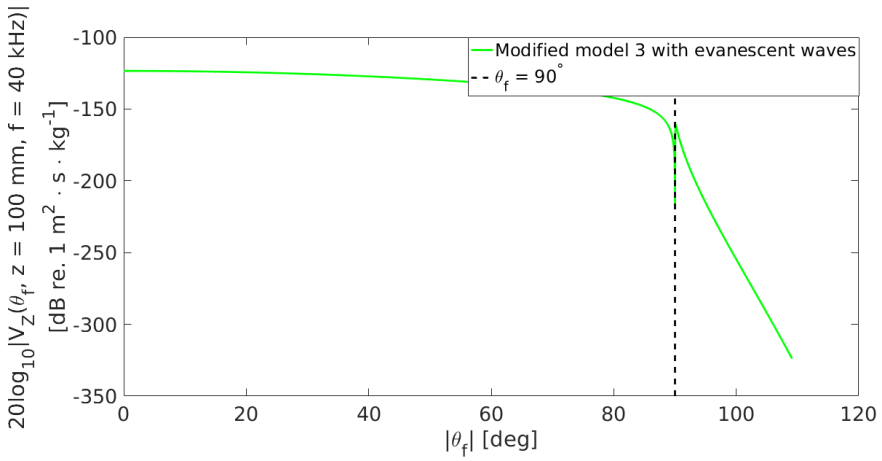

Figure 5.47: The magnitude of the angular spectrum of modified model 3 $|V_Z(\theta_f, z = 100\,\text{mm}, f = 40\,\text{kHz})|$ with evanescent waves with frequency $f = 40\,\text{kHz}$ at distance $z = 100\,\text{mm}$. The black dotted line represents where $\theta_f = 90°$.

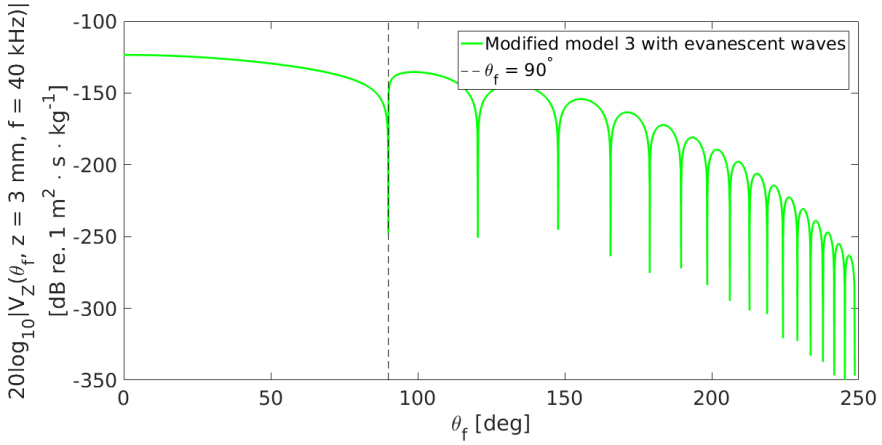

Figure 5.48: The magnitude of the angular spectrum $|V_Z(\theta_f, z = 3\,\text{mm}, f = 40\,\text{kHz})|$ of model 3 with evanescent waves with frequency $f = 40\,\text{kHz}$ at distance $z = 3\,\text{mm}$. The black dotted line represents where $\theta_f = 90°$.

piston model. Unlike Orofino and Pedersen he did not do any conversion to particle velocity, but propagated the pressure to a distance. He stated that this is only valid for distances bigger than approximately $z \approx a(ah_f)^{\frac{1}{3}}$ without giving any references to this, though it is believed to stem from parabolic equation approximations. He used a point receiver and this approximation refers to such a case. In Sec. 5.7.1. it is shown that the nearfield when using a finite receiver is "longer" than when using a point receiver. The pressure when using a finite receiver does not decay as $1/z$ at the Rayleigh distance, as the point receiver do. It can therefore be indicated that Younghouse's distance approximation of when the constant pressure boundary condition is valid, also applies for the case when using finite receiver, though for an even bigger distance. In addition to Younghouse's statement, Tjotta [41] stated that the constant pressure is valid as a boundary condition if the surface of the piston is compliant, which is not the case for the present study, as the piston is assumed to be baffled.

Model 3 simulates the normal particle velocity at the surface of a receiver. It was seen that the dynamics in the nearfield does not match with Williams. This may due to the fact that this represents particle velocity, or that the pressure boundary condition is seemingly not a valid boundary condition in the nearfield for the baffled piston model.

5.4 Scholte-waves in the plane-wave transmission coefficient

Before the comparisons with plate transmission in Sec. 5.5., it is necessary to discuss the phenomenon of surface waves in the plane-wave transmission coefficent, defined with Eq. (2.85), specifically known as Scholte-waves [42]. The parameters for the plate simulations are given in Sec. 3.1.

When working with the plate transmission analysis and not including losses, it was found that for a certain $\eta > h_f$, the transmission coefficient goes far above unity, see Fig. 5.49., where a closer look is shown in Fig. 5.50.

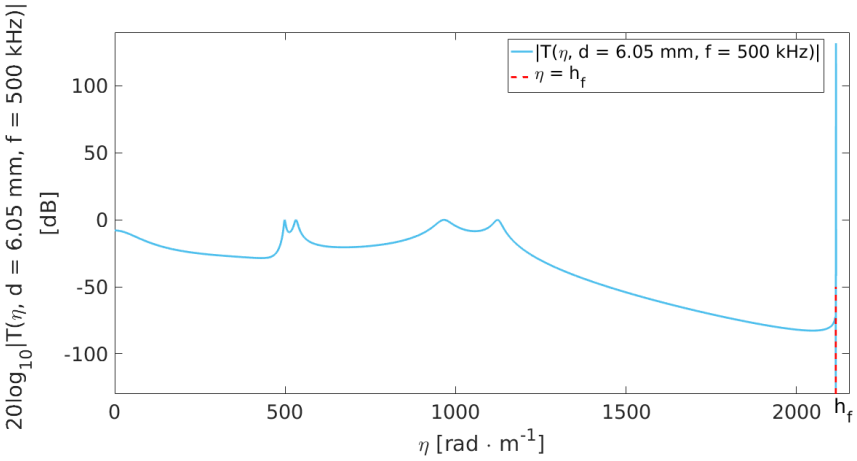

Figure 5.49: The magnitude of the transmission coefficient $|T(\eta, d = 6.05\,\text{mm}, f = 500\,\text{kHz})|$ at $f = 500\,\text{kHz}$ goes over unity when $\eta > h_f$, where the red dotted line represents $\eta = h_f$.

And with an even closer look, the spike actually consists of two spikes, see Fig. 5.51.

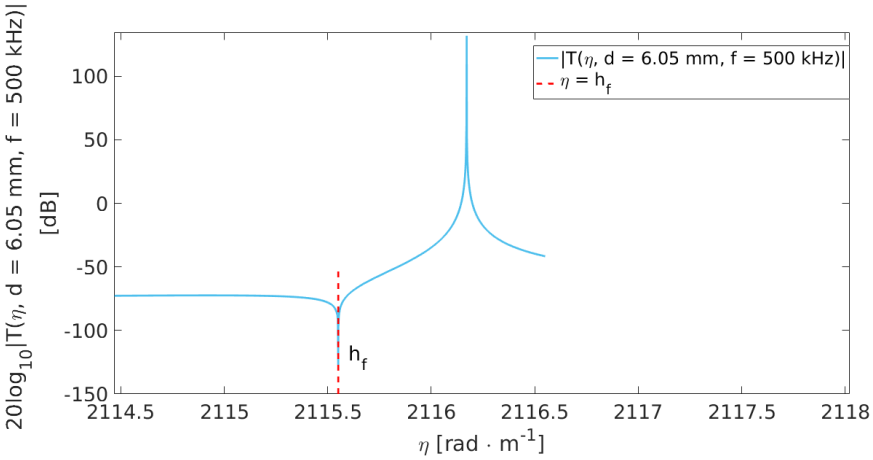

Figure 5.50: Zoomed in on Fig. 5.49. The red dotted line represents $\eta = h_f$.

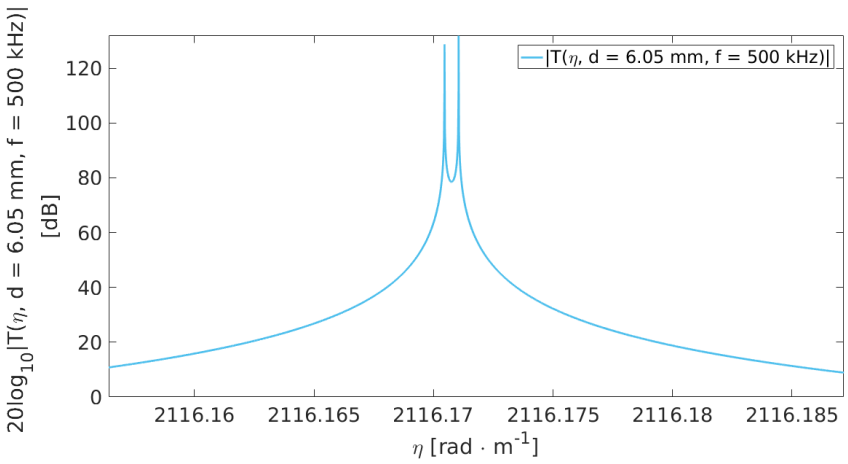

Figure 5.51: Zoomed in on Fig. 5.50.

The phenomenon was due to the presence of surface-waves at the interface of the plate-fluid/fluid-plate, also known as Scholte-waves [43], [44], [29], which can either trigger antisymmetric or symmetric modes at the interfaces between the fluid-plate and plate-fluid. These are not leaky Lamb-modes.

Osbourne and Hart [5] did a mathematical analysis of the dispersion equations, defined in Sec. 2.6.1., Eqs. (2.95), (2.96), and found an antisymmetrical and a symmetrical mode which are not near the leaky Lamb modes [5]. The analysis show that at low frequencies the phase velocity of the antisymmetric mode goes to zero, while the phase velocity of the symmetric mode goes towards the velocity of the wave in fluid. At high frequencies, both of the phase velocitites go asymptotically towards the velocity in the fluid.

The dispersion equations, Eqs. (2.95) and (2.96), can be used to find the wavenumbers at which there is Scholte-waves. The result is plotted in Fig. 5.52. for low frequencies.

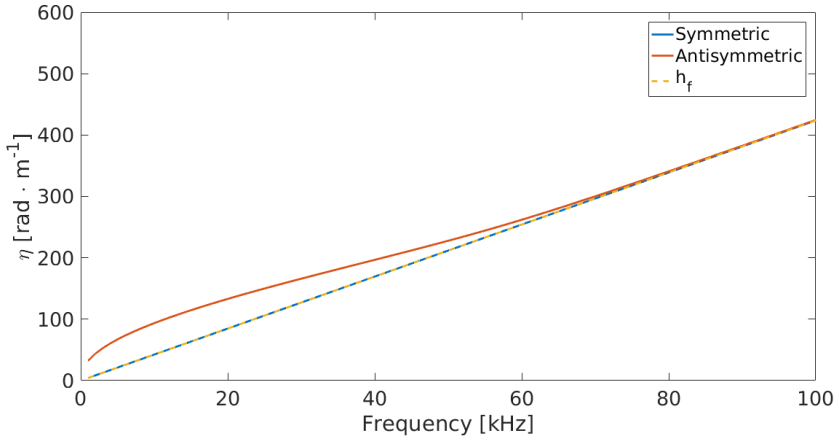

Figure 5.52: The dispersion diagram for lower frequencies of the symmetric and antisymmetric Scholte waves.

If the dispersion diagram is plotted in terms of the phase velocity instead, see figure 5.53, it shows the exact behavior of the two Scholte-waves as described in [43], [24], [5], [29], for low frequencies. Using then the wavenumbers found for the symmetric and antisymmetric Scholte-waves at $f = 500\,\text{kHz}$, the two spikes in Fig. 5.51. can be identified, see Fig. 5.54.

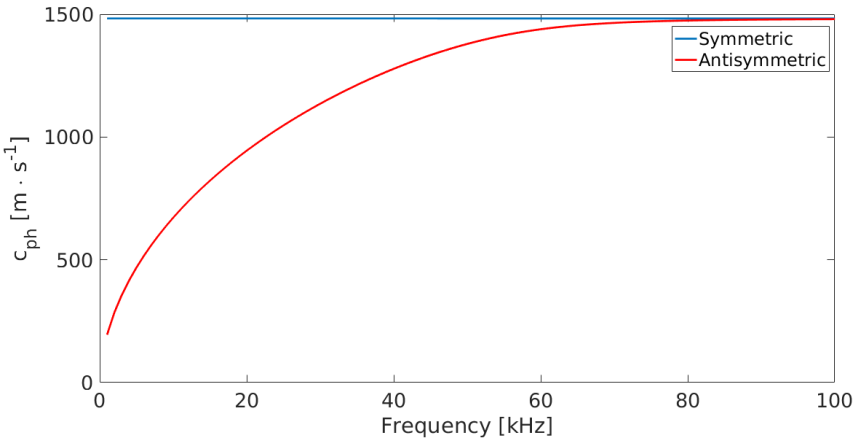

Figure 5.53: The dispersion diagram in terms of phase velocity c_{ph}, of the symmetric and antisymmetric Scholte waves for lower frequencies.

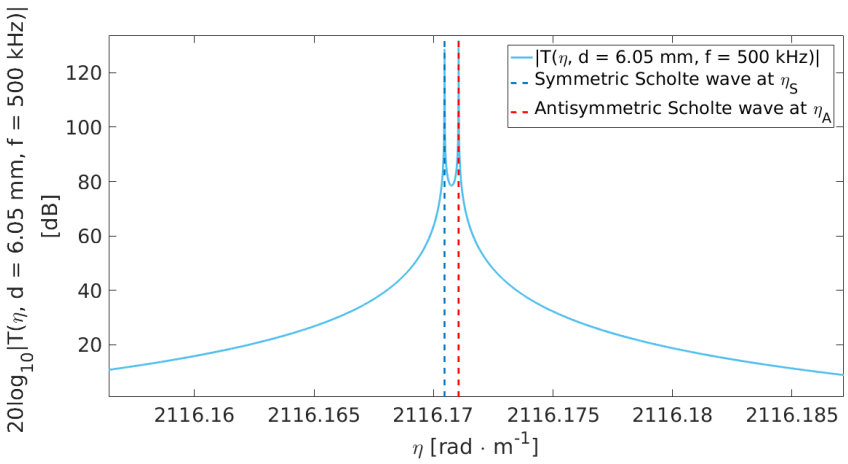

Figure 5.54: The Scholte-wavenumbers found at $f = 500\,\text{kHz}$ inserted in Fig. 5.51.

Thus the behavior of the transmission coefficient for these wavenumbers are caused by the presence of Scholte-waves. The answer of why the pressure of the angular spectrum is seemingly that much greater after transmission at this particular phase velocity and wavenumber remains unanswered as this would require a level of research that is beyond the scope of this thesis. It is still of interest to discuss whether these surface waves affect the sound field after plate transmission. In simulations however, it proved very difficult to get good simulations at low frequencies without any undersampling-effects, especially if the plate was in the nearfield of the source. This was therefore solved with the introduction of a complex wavenumber $\hat{h}_f$ in the fluid (loss in the fluid), and as a consequence, the spikes gets sufficiently damped down and affects the simulations less. This also reflects the fact stated by Glorieux et al. [45], that the energy of the Scholte-waves mainly exists in the fluid. An example of when loss is included in the transmission coefficient at $f = 500\,\text{kHz}$, using a Q-factor of $Q_f = 5 \cdot 10^3$ is shown in Fig. 5.55. Even with such a small amount of loss, the Scholte-waves' influence on the transmission coefficient are significantly damped, but still goes above unity.

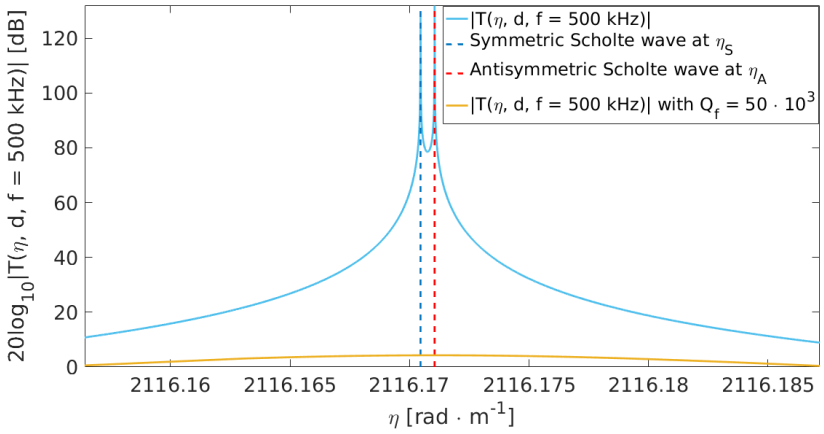

Figure 5.55: The transmission coefficient with loss versus without loss using $Q_f = 5 \cdot 10^3$ at $f = 500\,\text{kHz}$.

5.5 Comparison of transmission models with plate in farfield

The transfer function of interest is $H_{<p><p>}(f)$ and $H_{<pv><pv>}(f)$, defined in Sec. 2.7., Eq. (2.99) and Eq. (2.100), respectively. Loss in fluid have been included in all the simulations. The three models will not be individually presented because they give surprisingly equal results, which in turn will be discussed.

Using model 1, 2, and 3 with plate, Eqs. (2.29), (2.32), (2.56), respectively, the results of the transfer functions are shown in Fig. 5.56. The different maxima and minima, which are due to the excitation of leaky Lamb modes in the plate, are labeled using the associated leaky Lamb mode label following the convention used in [21] and [28]. The frequencies of maximum or minimum transmission in the respective models are given in Tab. 5.1 along with their associated leaky Lamb mode label. The frequencies was determined using a smaller step-size, 0.1 kHz, for more accuracy, and then rounded up to integers.

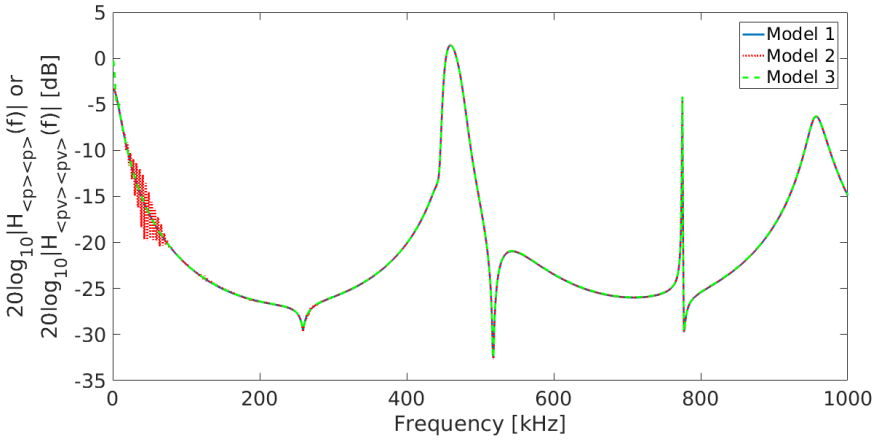

Figure 5.56: The transfer function $|\mathrm{H}_{<\mathrm{p}><\mathrm{p}>}(f)|$ using model 1 and model 2, and the transfer function $|\mathrm{H}_{<\mathrm{pv}><\mathrm{pv}>}(f)|$ using model 3.

Table 5.1: The frequencies of maximum and minimum transmission between the models.

Label:	Model 1 [kHz]	Model 2 [kHz]	Model 3 [kHz]
A_1	259	259	259
S_{-2}	460	460	460
S_2	518	518	518
A_2	775	775	775
A_3	957	957	957

Except at frequencies below approximately $f = 30\,\mathrm{kHz}$, there is virtually no difference in the three models, which is not surprising. $\mathrm{H}_{<\mathrm{p}><\mathrm{p}>}(f)$ and $\mathrm{H}_{<\mathrm{pv}><\mathrm{pv}>}(f)$ are relative to the pressure or particle velocity at 270 mm and in Sec. 5.3.2., it was shown that distance-relative normal particle velocity and pressure have very similar dynamics, especially as the distance increases. Because of this, the transfer functions will therefore be indistinguishable. Also in Sec. 5.3.3., it was shown the exclusion of evanescent waves in model 3 gives very similar results if compared to a simulation that includes evanescent waves, especially with high frequencies or large distances. Additionally, the missing factors in model 2 and model 3 does not matter, again because the transfer functions are relative.

For the lower frequencies, some deviance between the models, and the transfer functions $\mathrm{H}_{<\mathrm{p}><\mathrm{p}>}(f)$ and $\mathrm{H}_{<\mathrm{pv}><\mathrm{pv}>}(f)$ are found, see Fig.

5.57. for a closer look.

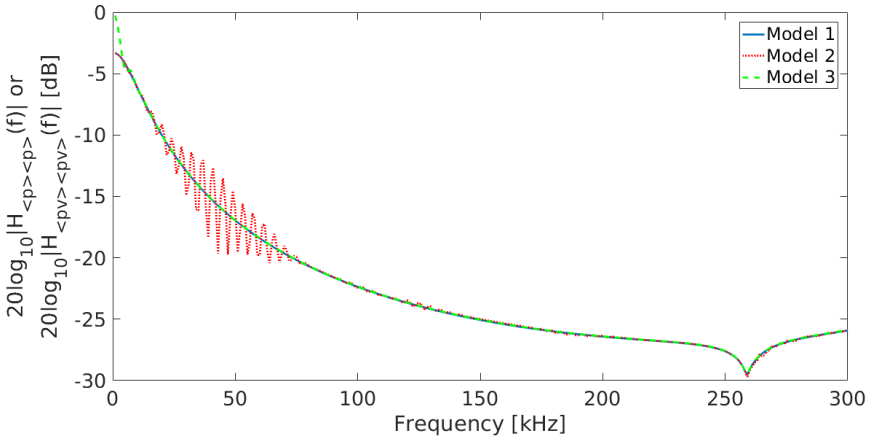

Figure 5.57: Zoomed in on the lower frequencies in the comparison of the transfer function $|\mathrm{H}_{<\mathrm{p}><\mathrm{p}>}(f)|$ using model 1 and model 2, and the transfer function $|\mathrm{H}_{<\mathrm{pv}><\mathrm{pv}>}(f)|$ using model 3.

Model 2 is afflicted by undersampling effects. At the frequency range between approximately 10 kHz and 80 kHz model 2 struggles to sample correctly, even though losses are included. It was shown in Sec. 5.2. that model 2 had some undersampling effects at 40 kHz due to it not being able to sample the angular spectrum close enough. However, as seen in Fig. 5.57., this is exclusively for the frequency range between 10 kHz and 80 kHz, as it is able to calculate the transfer function for lower and higher frequencies than this range. Why this frequency range is particularly hard to sample have not been investigated, as this frequency range is not important for the scope of the thesis.

Between the transfer functions, there is deviance for very low frequencies, i.e., lower than approximately 15 kHz, see Fig. 5.58. for a closer look. This difference may be due to model 3 excluding evanescent waves, so in Fig. 5.59. the modified model 3 have been simulated with evanescent waves, and the resulting transfer function is different when excluding evanescent waves.

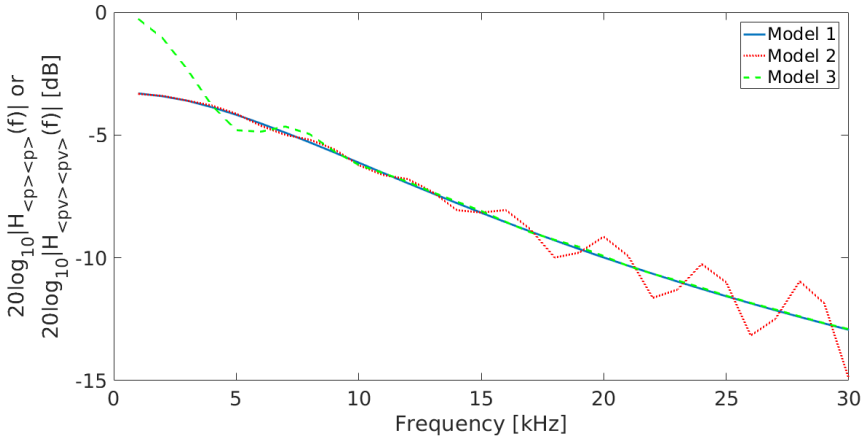

Figure 5.58: The transfer functions for frequencies below 30 kHz.

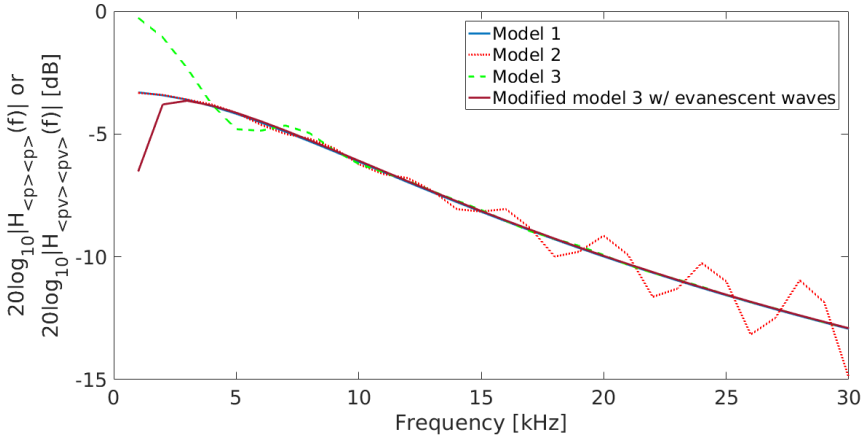

Figure 5.59: The transfer functions for frequencies below 30 kHz, including the transfer function calculated using modified model 3 with evanescent waves.

It seems therefore that the exclusion is not valid for these frequencies, but the validity of the dampening of Scholte-waves should be confirmed through measurements or other methods. The difference using model 1 and 3 could be due to the fact that as $h_f a \to 0$ the baffled piston source goes towards that of a point source where the pressure and particle velocity are more out of phase [30].

In order to verify the results of the transfer function, model 1 is used to compare with measurement, which implicitly verifies the other two

models as well because of their similarity. The results of simulation compared to measurement are presented in Fig. 5.60.

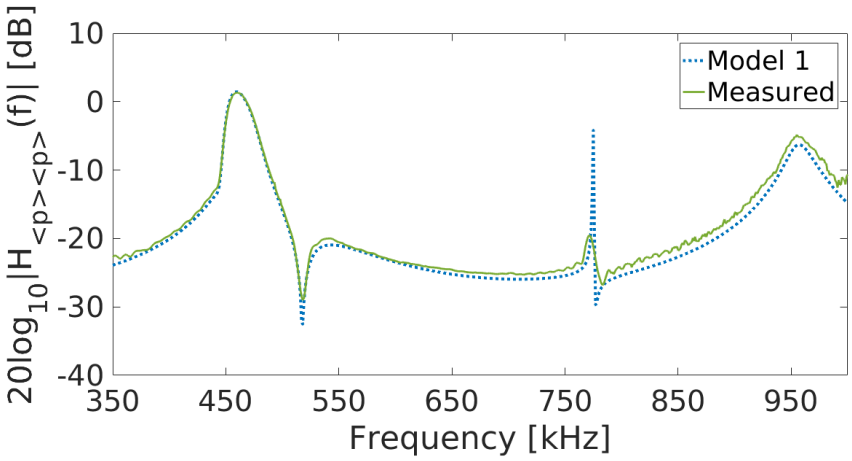

Figure 5.60: The measured and simulated transfer function $|H_{<p><p>}(f)|$ with plate and finite receiver using model 1 to calculate the simulation.

The frequencies of maximum and minimum transmission are given in Tab. 5.2.

Table 5.2: The differences in frequencies of maximum and minumum transmission between model 1 and measurements.

Label:	Simulated [kHz]	Measured [kHz]
S_{-2}	460	460
S_2	518	518
A_2	775	771
A_3	957	955

The deviance of frequency and magnitude between measurements and simulations at the maximum associated with the A_2-mode is characteristic to the ASM: similar results can be seen in e.g. [21] and [18]. Furthermore, the indicated deviance of magnitude at the A_3 mode, may be because of the radius of the piston used in simulations. In Sec. 3.1. it was shown how the radius of the piston was determined, and stated that the radius is determined by using the angle θ_{-3dB} of the real transducer at 575 kHz. Adjusting the radius to, e.g., a frequency of 850 kHz of the real transducer, the radius is $a = 12.2$ mm. Using model 1 to

calculate $H_{<p><p>}(f)$ with this radius as source- and receiver radius, the magnitude at A_3 fits better, see Fig. 5.61.

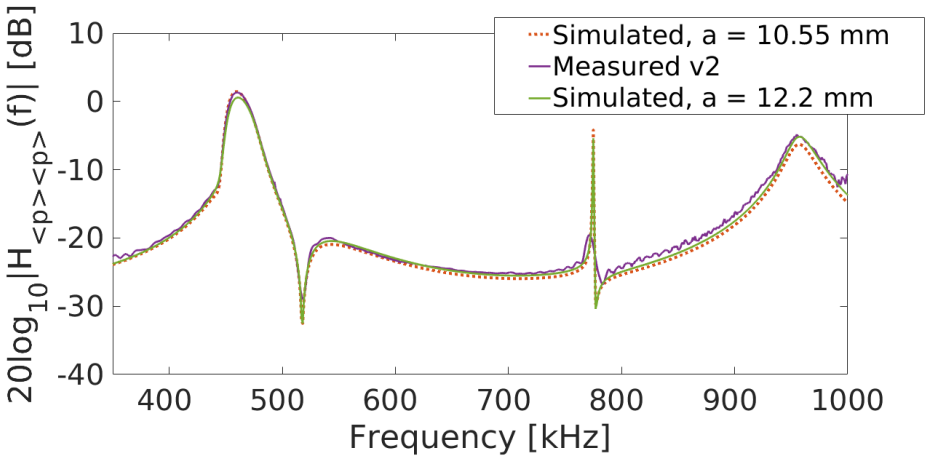

Figure 5.61: $|H_{<p><p>}(f)|$ calculated using model 1 with radius $a = b = 12.2\,\mathrm{mm}$ compared with measurement.

The magnitude on the S_{-2} deviates, because the radius is adjusted for a high frequency. Ideally, the radius of the piston source in the simulation program would be frequency dependent, by determining the effective radius for the real transducer for a wider range of frequencies, but this is not done at the present time.

5.6 Comparison of transmission models with plate in nearfield

Waag used Orofino and Pedersens model for a transmission-case as done here, i.e. model 3. An incentive to compare with him, is that he had the plate in the nearfield, which may introduce differences considering the the exclusion or inclusion of evanescent waves, and the different dynamics seen with normal particle velocity and pressure in the nearfield. Waag's simulation parameters were:

- $a = b = 10\,\mathrm{mm}$,
- $c_f = 1500\,\mathrm{m} \cdot \mathrm{s}^{-1}$,
- $\rho_f = 1000\,\mathrm{kg} \cdot \mathrm{m}^{-3}$,

- $\rho_p = 7945\,\mathrm{kg} \cdot \mathrm{m}^{-3}$,
- $c_{p,l} = 5790\,\mathrm{m} \cdot \mathrm{s}^{-1}$,
- $c_{p,s} = 3300\,\mathrm{m} \cdot \mathrm{s}^{-1}$,
- $d_T = 40\,\mathrm{mm}$,
- $d_R = 50\,\mathrm{mm}$,
- $d = 10\,\mathrm{mm}$,
- $z = d_T + d_R = 90\,\mathrm{mm}$,
- $f_{l1} = 298500\,\mathrm{kHz}$,

where f_{l1} is the cut-off frequency of the leaky Lamb mode he labeled as S_2, which can be calculated using Eq. (2.91). For more details concerning Waag's work, see the dissertation [19].

In Waag's dissertation, there is specifically a plot [19][p. 91, Fig. 2.] to compare with. The data of this plot were retrieved from Waag himself [46]. Only model 1, model 3 and modified model 3, will be used to compare with Waag's result, because it was shown in Sec. 5.5. that model 1 and 2 gives equivalent results. Additionally, it was shown that model 2 does not handle the low frequencies properly, and it is therefore difficult to get decent simulations when the plate is at an even shorter distance from to the source. This because the number of samples required to sample the Scholte-waves have to be quite large as the evanescent part is more significant at shorter distances. Regardless, model 1 and model 2 both represent the principle of using constant normal particle velocity velocity on the piston source surface which is used to solve for an expression for pressure at the receiver surface, and the comparison with Waag is mainly meant to serve as comparison of the different principles used.

The data retrieved by Waag was somewhat corrupted in the sense that the data had shifted slightly from what is believed to be correct, due to article writing processes [46]. The data is the transmitted particle velocity as a function of frequency, normalized to its maximum transmitted value, in dB. This means that the plot should go to 0 at the maximum value, but the retrieved data did not. This was solved by adding the difference between 0 and maximum value to the data. The results of this can be seen in Fig. 5.62.

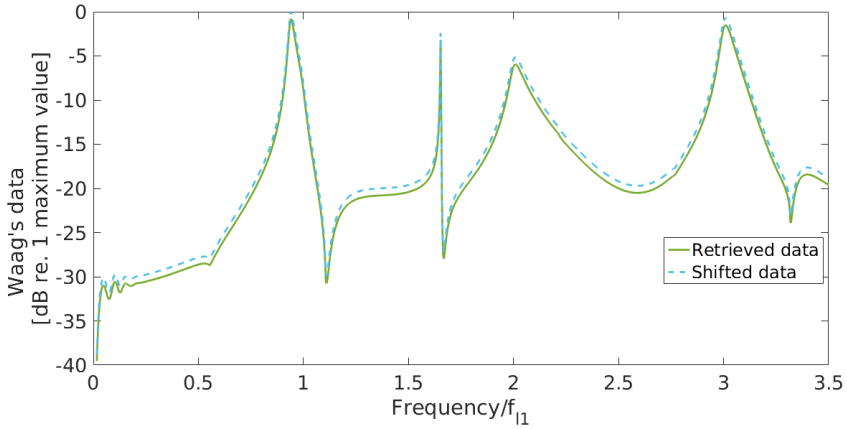

Figure 5.62: The retrieved data from Waag compared to the shifted data.

The original data does not go to zero, and is at a constant value below the shifted data. The shifted data will be used for further comparisons.

In Fig. 5.63., model 3 has been used for the same case in order to reproduce Waag's data.

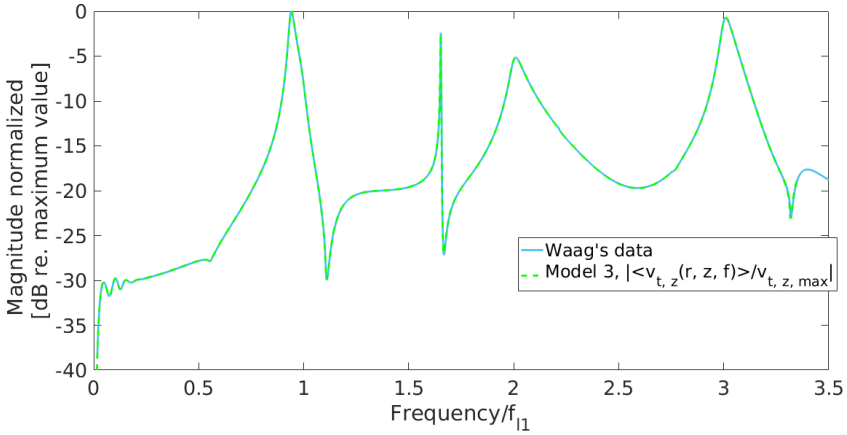

Figure 5.63: Waag's shifted data reproduced using model 3 compared to the shifted data retrieved from Waag.

The reproduced results match with Waag, which also adds validity to the simulations shown using model 3. In Fig. 5.64., a simulation using model 1 have been calculated with Waag's parameters.

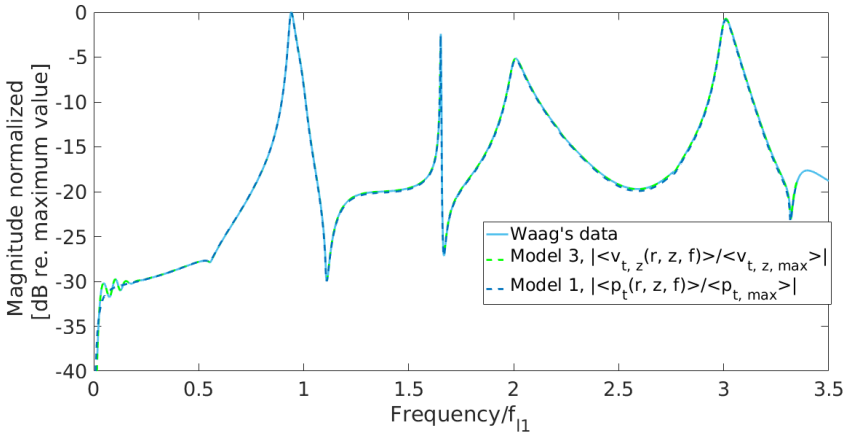

Figure 5.64: Waag's shifted data compared with model 3 and model 1.

Once again there are only very subtle differences between model 1 and 3 in the overall frequency range, with more deviance for very low frequencies. A closer look at the magnitude for the frequencies between $0 \leq Frequency/f_{l1} \leq 0.3$, which approximately corresponds to frequencies less than 90 kHz, are shown in Fig. 5.65.

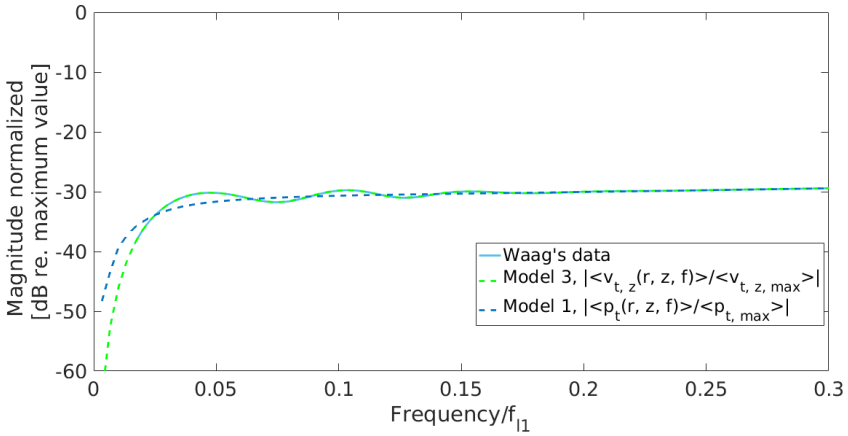

Figure 5.65: Zoomed in the lower frequency range of Fig. 5.64.

The difference between model 1 and 3 may be caused by the fact that model 1 represent pressure, while model 3 represent particle velocity. In Sec. 5.5., Fig. 5.59., it was however seen that the exclusion of evanescent waves in model 3 gives a different results to compared when evanescent waves are included. This may very well be the reason in

Fig. 5.65., so in Fig. 5.66. modified model 3 have been simulated with evanescent waves.

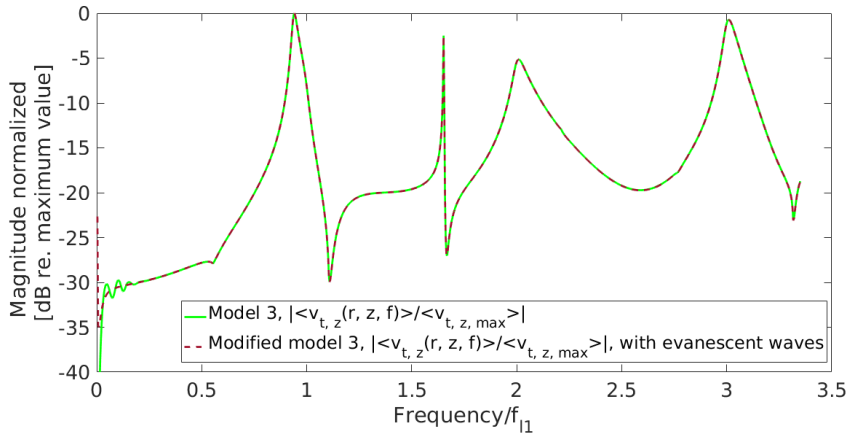

Figure 5.66: Model 3 compared to modified model 3 including evanescent waves for Waag's plate transmission setup.

The exclusion of evanescent waves are in general valid, but zooming in on lower frequencies, see Fig. 5.67., there is again a difference when including evanescent waves.

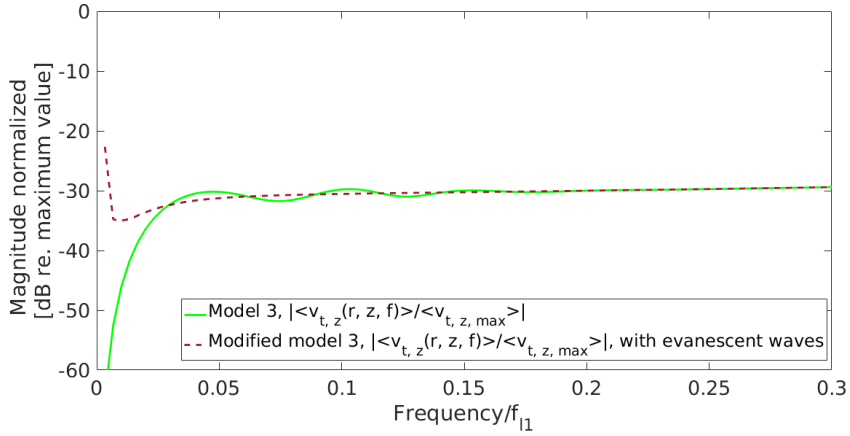

Figure 5.67: Zoomed in on the lower frequencies of Fig. 5.66. The frequencies below $Frequency/f_{l1} \leq 0.3$ corresponds to frequencies less than approximately 90 kHz.

In Sec. 5.5. it was seen that model 3 when including evanescent waves compared to when excluding evanescent waves gives different results for

frequencies less than approximately 15 kHz. The same is seen in Fig. 5.67., but for a wider range of frequencies, which is due to the plate being in the nearfield where the significance of the evanescent waves increases.

Modified model 3 including evanescent waves are compared with model 1 from in Fig. 5.68.

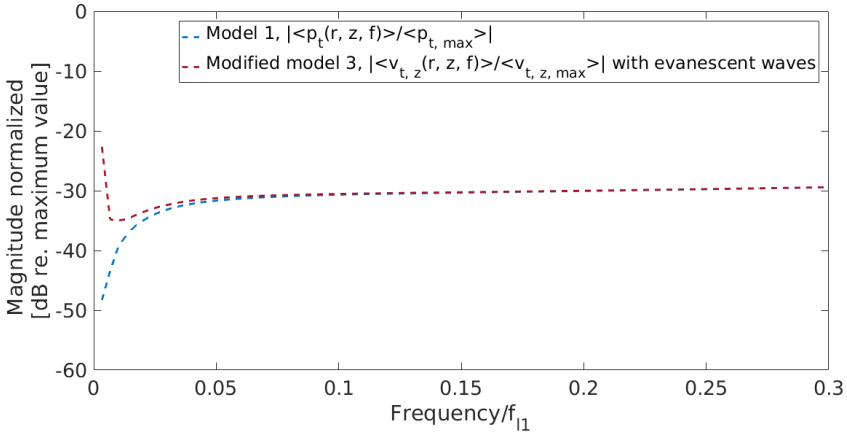

Figure 5.68: Modified model 3 compared to model 1 with Waag's transmission setup.

For frequencies less than $Frequency/f_{l1} = 0.05$ which corresponds approximately to to 15 kHz, there are some differences, which again may be because the pressure and particle velocity are more out of phase as $h_f a \to 0$ [30].

5.7 Finite receiver compared to point receiver

This section will show and discuss some differences when using a point receiver compared with a finite receiver, without and with plate.

5.7.1 Without plate

In Sec. 5.1.2., model 1 was validated through the comparison with Kinsler et al.'s model for the on-axis pressure with a point receiver,

and through the comparison with Williams' model for a finite receiver. Comparing then the simulations of model 1 without plate, using a point receiver and finite receiver for a frequency $f = 500\,\text{kHz}$ as a function of distance to $z = 120\,\text{mm}$, the results are given in Fig. 5.69.

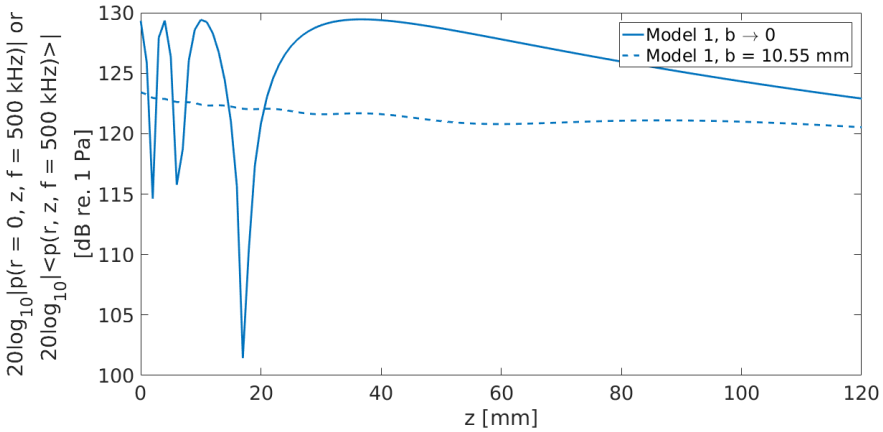

Figure 5.69: Model 1 with point receiver compared to model 1 with finite receiver as a function of distance to $z = 120\,\text{mm}$ with frequency $f = 500\,\text{kHz}$. $h_f a = 22$. $R_A = 110\,\text{mm}$.

The impact of the finite receiver compared to the point receiver is clearly seen, and while the pressure at the point receiver decays as $1/z$ at the Rayleigh distance, the pressure at the finite receiver does not. To see this, the relation

$$|pressure| \propto \frac{A}{z},$$
$$A \propto |pressure| \times z, \tag{5.2}$$

can be used. Multiplying the simulations in Fig. 5.69. with the distance z, the results are given in Fig. 5.70.

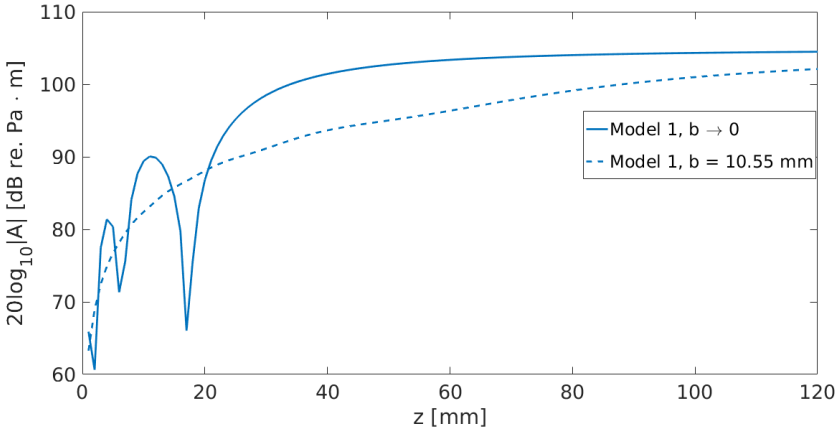

Figure 5.70: The calculations in Fig. 5.69 multiplied with the distance.

The constant A in the point-receiver case is constant at approximately $z = 100\,\text{mm}$ while the finite-receiver case is not constant for any distance in the figure. Extending the simulations to $z = 300\,\text{mm}$, A for the finite receiver is constant at approximately $z = 250\text{mm}$, and the pressure at the point receiver and finite receiver become approximately equal, see Fig. 5.71.

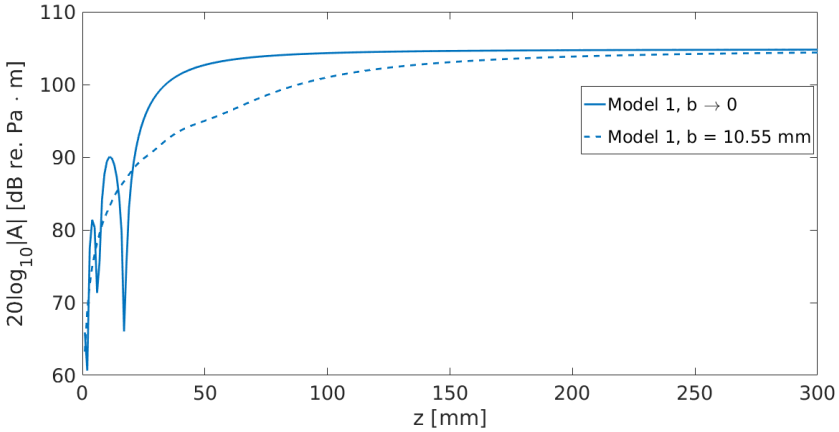

Figure 5.71: The calculations in Fig. 5.70. extended to 300 mm.

The Rayleigh distance is not a good approximation to when the pressure decays as $1/z$ for the finite receiver. The reason is that the wave need a bigger distance to diverge, in order for the wavefront to become approximately planar over the surface of the finite receiver. This can

be verified by looking at the spatial distribution of the spatial pressure, which can be done by using the expression derived without finite receiver, Eq. (2.22) with $T(\eta, d) = 1$. The spatial distribution at $z = 110\,\text{mm}$ and $z = 250\,\text{mm}$ at frequency $f = 500\,\text{kHz}$ to a radial distance $r = 100\,\text{mm}$ have been calculated and plotted in Fig. 5.72.

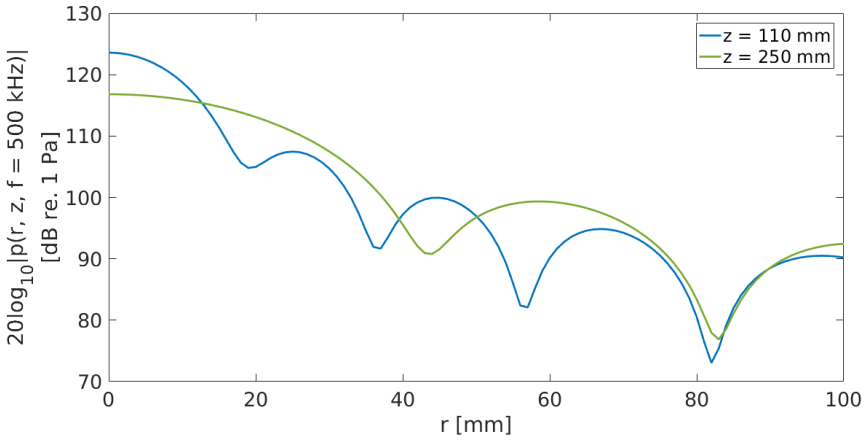

Figure 5.72: The spatial distribution of the pressure at a distance $z = 120\,\text{mm}$ and at $z = 250\,\text{mm}$ with frequency $f = 500\,\text{kHz}$.

Zooming in on the radial distance up to $r = 20\,\text{mm}$, because the radius of the receiver is $10.55\,\text{mm}$, reveals why the pressure with a finite receiver is different at the two distances, see Fig. 5.73.

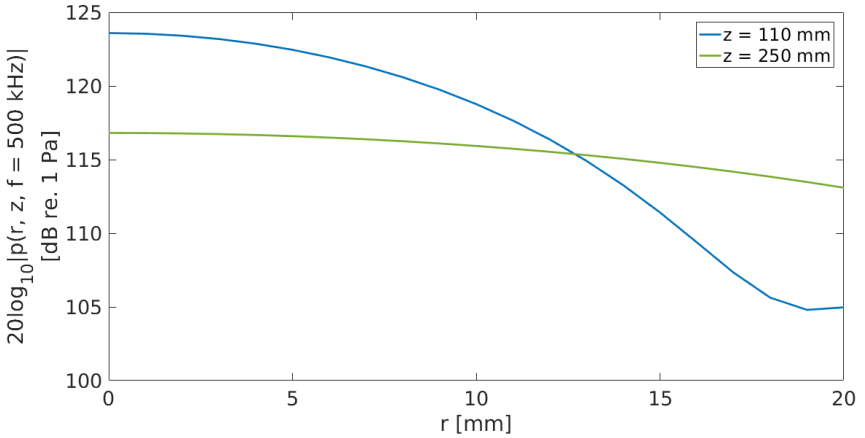

Figure 5.73: Zoomed in on the spatial distribution in Fig. 5.72. to a radial distance $r = 20\,\text{mm}$.

For $r \leq 10.55\,\text{mm}$ at $z = 250\,\text{mm}$ the pressure is more or less constant with increasing r. Averaging this with respect to r will therefore give an average value close to the pressure value of the on-axis component where $r = 0$. At $z = 110\,\text{mm}$ for $r \leq 10.55\,\text{mm}$, the pressure is far from constant, so the average pressure at the finite receiver will be less than the pressure value of the on-axis component.

In Fig. 5.74. model 1 with a point receiver compared to model 1 with finite receiver have again been plotted as a function of distance, but for a frequency of $f = 40\,\text{kHz}$.

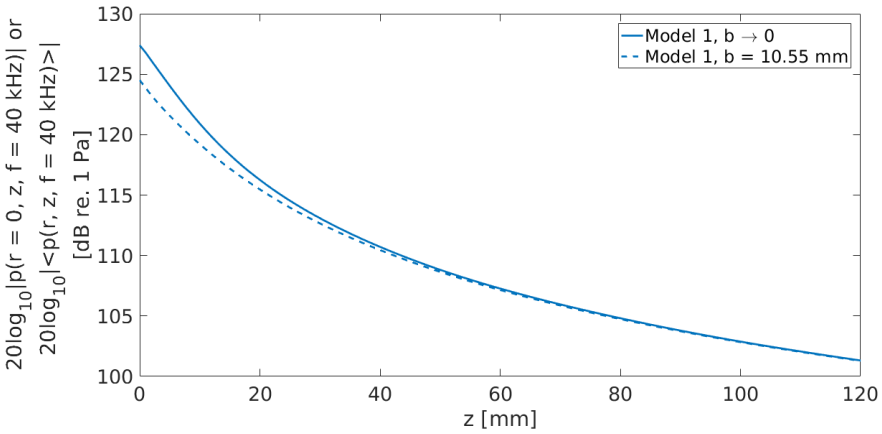

Figure 5.74: Model 1 with point receiver compared to model 1 with finite receiver as a function of distance to $z = 120\,\text{mm}$ with frequency $f = 40\,\text{kHz}$.

Again, the Rayleigh-distance, which is approximately 9 mm, is not a good measure for the farfield in finite receiver case. This can also be verified with a simulation at a frequency of $f = 1000\,\text{kHz}$, see Fig. 5.75. These results will come in handy for understanding the results of Sec. 5.7.2.

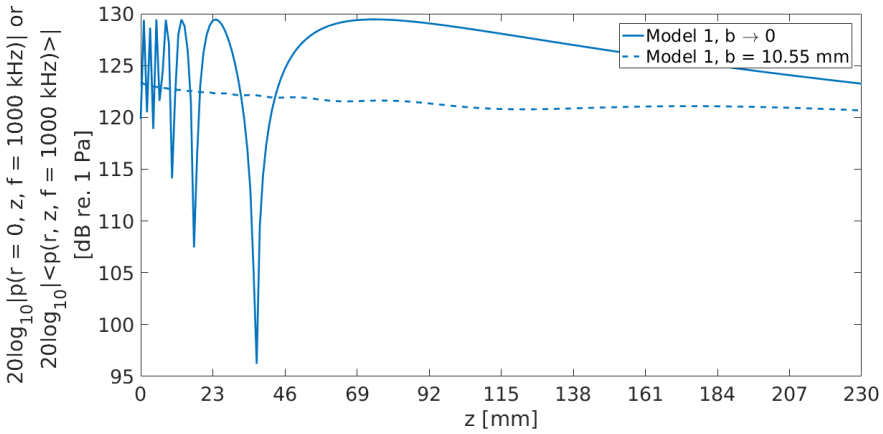

Figure 5.75: Model 1 with point receiver compared to model 1 with finite receiver as a function of distance to $z = 230\,\text{mm}$ with frequency $f = 1000\,\text{kHz}$. $R_A = 220\,\text{mm}$.

5.7.2 With plate

To study the influence of a finite receiver in plate transmission, the transfer function $\mathrm{H_{p<p>}}(f)$, defined in Sec. 2.7., Eq. (2.98), can be compared to the point receiver transfer function $\mathrm{H_{pp}}(f)$, Eq. (2.97). Using model 1, the two transfer function are calculated in Fig. 5.76.

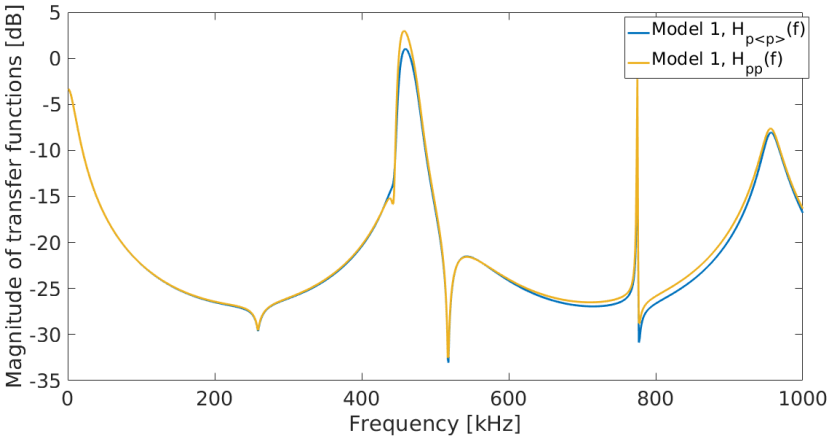

Figure 5.76: The transfer functions $\mathrm{H_{p<p>}}(f)$ and $\mathrm{H_{pp}}(f)$ calculated using model 1.

The frequencies of maximum and minimum transmisson are given in

Tab. 5.3.

Table 5.3: The different frequencies of maximum and minumum transmission of $H_{p<p>}(f)$ and $H_{pp}(f)$.

Label:	$H_{pp}(f)$ [kHz]	$H_{p<p>}(f)$ [kHz]
A_1	259	259
S_{-2}	458	460
S_2	517	518
A_2	775	775
A_3	956	957

In order to confirm that $H_{pp}(f)$ is calculated correctly, a comparison between measured and simulated $H_{pp}(f)$ are presented in Fig. 5.77.

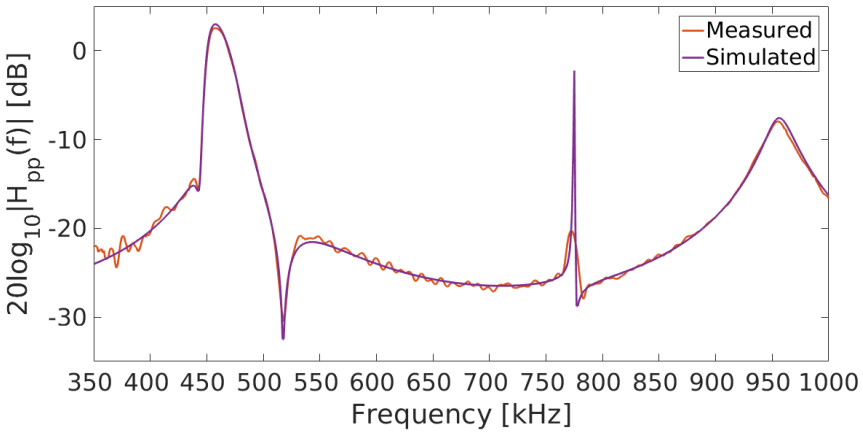

Figure 5.77: The transfer function $H_{pp}(f)$ calculated with model 1 compared with measurement.

The frequencies of maximum and minimum transmission of the simulated and measured $H_{pp}(f)$ are given in Tab. 5.4.

Table 5.4: The differences in frequencies of maximum and minumum transmission between simulated and measured $H_{pp}(f)$.

Label:	Simulated [kHz]	Measured [kHz]
S_{-2}	458	458
S_2	517	518
A_2	775	772
A_3	956	955

Looking at the results for low frequencies in Fig. 5.76., i.e., frequencies less than $f = 350\,\text{kHz}$, the two transfer functions are almost equal. This is because the transmitted beam is wide, and almost constant with respect to the radial direction, so the average pressure will be almost equal to the on-axis component. In Fig. 5.78. the transmitted pressure using model 1 without finite receiver, Eq. (2.22), have been calculated with $z = 376.05\,\text{mm}$ up to a radial distance of $r = 20\,\text{mm}$ for a frequency of $f = 200\,\text{kHz}$. The simulation have been normalized with the on-axis component to see the dynamics in magnitude with respect to r, a bit clearer.

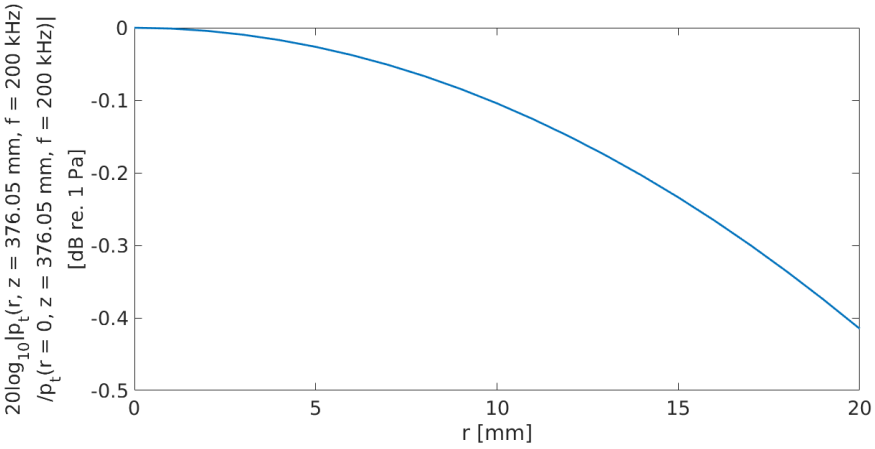

Figure 5.78: The spatial distribution of the pressure at $z = 270\,\text{mm}$ and $z = 376.05\,\text{mm}$ at frequency of $f = 200\,\text{kHz}$ normalized to the on-axis component.

The pressure at at $r = 10.55\,\text{mm}$ is approximately 0.1 dB less than the on-axis component. With such a small difference, the average transmitted pressure will be almost equal to the on-axis component, which

in turn gives almost equal transfer functions, because the denominator in both transfer functions are equal.

At the transfer functions' maximum magnitude, which is caused by exciting the S_{-2}-mode in the plate, there is a deviance in magnitude and a shift of frequency, where the point receiver transfer function $H_{pp}(f)$ has a higher magnitude compared to $H_{p<p>}(f)$, with maximum transmission at a lower frequency. The reason can again be explored by looking at the spatial dristribution of the pressure on the upper side of the plate, $z = 270\,\text{mm}$, and at $z = 376.05\,\text{mm}$ on the lower side of the plate, see Fig. 5.79.

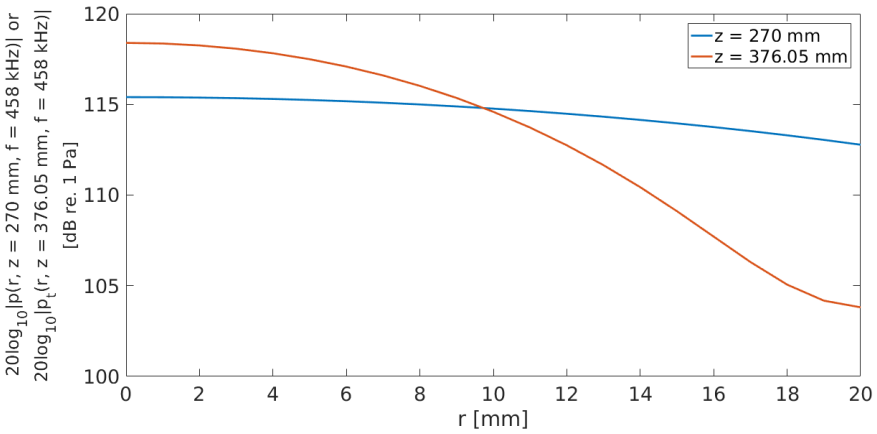

Figure 5.79: Spatial distribution of pressure at the distances $z = 270\,\text{mm}$ and $z = 376.05\,\text{mm}$ with frequency $f = 458\,\text{kHz}$.

The transmitted beam is narrower and less constant with increasing r, which means that the average pressure received by the finite receiver will be less than that of a point receiver.

The shift of frequency can also be explained by similar means. In Fig. 5.80., the spatial distribution at $z = 376.05\text{mm}$ for the frequencies $f = 458\,\text{kHz}$, $f = 459\,\text{kHz}$, and $f = 460\,\text{kHz}$ are plotted.

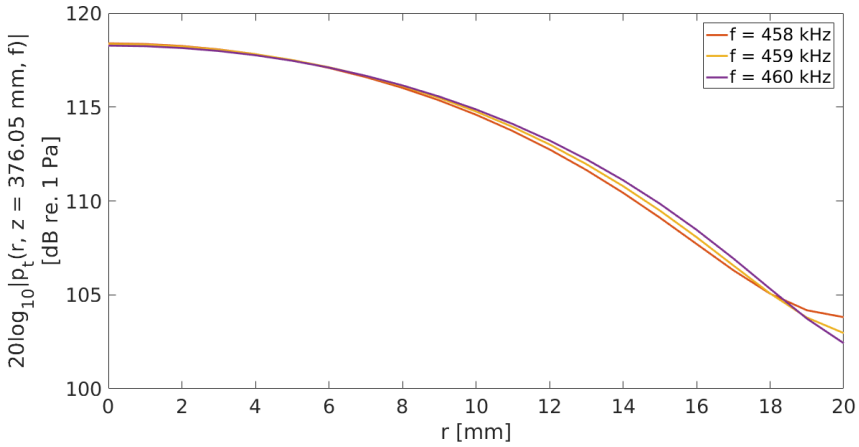

Figure 5.80: Spatial distribution of pressure at the distance $z = 376.05\,\text{mm}$ with frequencies $f = 458\,\text{kHz}$, $f = 459\,\text{kHz}$ and $f = 460\,\text{kHz}$.

The spatial distribution at the different frequencies are overall similar, but the pressure at $f = 460\,\text{kHz}$ is slightly bigger than the other frequencies with increasing r. This means that the average pressure at the receiver will be slightly higher at $f = 460\,\text{kHz}$ than the other frequencies.

The difference of magnitude at the A_3-mode between the two transfer functions is approximately $0.5\,\text{dB}$. The small difference is due to a widening of the beam at these frequencies [21]. This can further be explained by looking at the spatial distribution of the pressure at the frequencies $f = 956\,\text{kHz}$ and $f = 957\,\text{kHz}$. In Fig. 5.81. the spatial pressure have been calculated for a distance $z = 376.05\,\text{mm}$ for these frequencies.

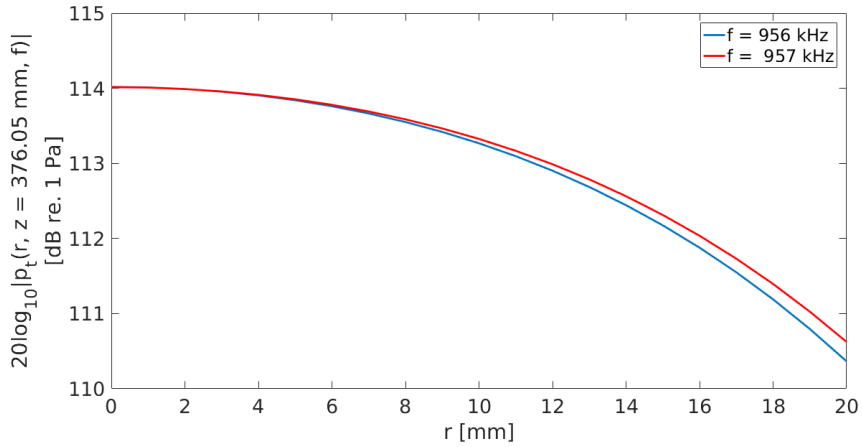

Figure 5.81: Spatial distribution of transmitted pressure at the distance $z = 376.05\,\text{mm}$ with frequencies $f = 956\,\text{kHz}$ and $f = 957\,\text{kHz}$.

The spatial pressure at $f = 957\,\text{kHz}$ is equal or higher than the pressure at $f = 956\,\text{kHz}$ when r is increasing. At approximately $r = 10.55\,\text{mm}$ the difference of the pressure at $f = 957\,\text{kHz}$ compared to the on-axis component is less than $1\,\text{dB}$, which again gives an almost equal average pressure to the on-axis component. Because the pressure at $f = 957\,\text{kHz}$ is generally higher with increasing r compared to the pressure at $f = 956\,\text{kHz}$, there is also a frequency shift of maximum when using a finite receiver.

Chapter 6

The receiver distance dependency of plate transmission effects

This chapter will introduce simulation results when increasing the distance between the plate and receiver. In Sec. 6.1. some of the previous work done on this will be discussed and reproduced with model 1, before the continuation of this work is presented in Sec. 6.2. The phenomena observed in this section, will be discussed in more detail in Sec. 6.3.

The simulation parameters are given in Sec. 3.1., though the frequency range from now on will be between 350 kHz to 1000 kHz which is the frequency range of excitation of the leaky Lamb modes of interest. The simulations are also lossless, because the Scholte-waves' significance in the spectrum disappear for high frequencies and large distances due to the fast decaying exponential term.

6.1 Comparisons with previous work

In the articles [25] and [28], the transfer function $\mathrm{H}_{\mathrm{pp}}^{\mathrm{plate}}(f)$ is used to compare with the single plane-wave transmission coefficient as a function of frequency. If $\mathrm{H}_{\mathrm{pp}}^{\mathrm{plate}}(f)$, and the plane-wave transmission coefficent with a single incident plane wave, $T(\eta = 0, d, f)$, are compared as a function of frequency, the differences can be seen in Fig. 6.1. using model 1 Eq. (2.29 with receiver radius $b \to 0$) to calculate $\mathrm{H}_{\mathrm{pp}}^{\mathrm{plate}}(f)$.

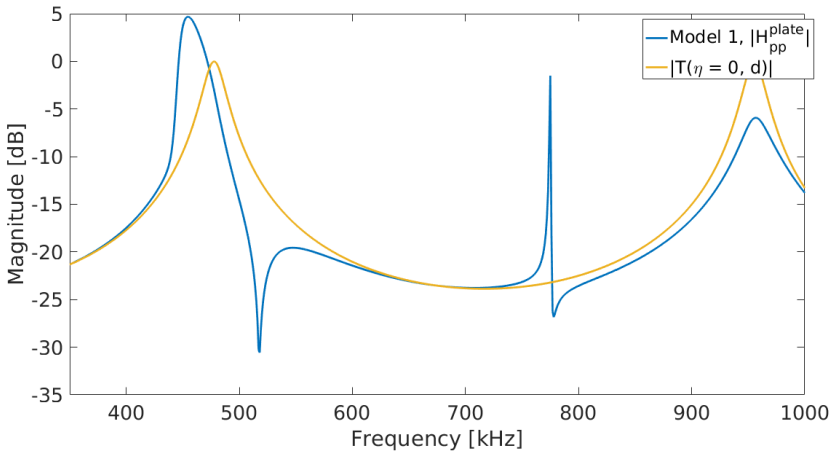

Figure 6.1: $|\mathrm{H}_{\mathrm{pp}}^{\mathrm{plate}}(f)|$ compared with the single plane-wave transmission coefficient, as a function of frequency.

The frequency of maximum transmission predicted by the transmission coefficient is $f = 477\,\mathrm{kHz}$, while the frequency of maximum transmission in $\mathrm{H}_{\mathrm{pp}}^{\mathrm{plate}}(f)$ is $f = 455\,\mathrm{kHz}$. The maximum caused by the A_3 mode in the plate, is $f = 955\,\mathrm{kHz}$ for the transmission coefficient, and $f = 957\,\mathrm{kHz}$ for $\mathrm{H}_{\mathrm{pp}}^{\mathrm{plate}}(f)$.

In the articles by Aanes et al. [27] and [28], some figures of the transmitted field as a function of distance are shown for certain frequencies. In [27][p. 4 Fig. 5], the on-axis pressure for $f = 457\,\mathrm{kHz}$ is shown. 457 kHz is the frequency of maximum transmission which Aanes et al. found with the Hybrid-ASM, when the point receiver is situated 100mm from the plate. This deviates slightly with the results given in section 5.7.2, but as the Hybrid FEM-ASM is based on the FEM and ASM, some differences may be introduced.

Using model 1, Eq. (2.29 with receiver radius $b \to 0$), the on-axis pressure at frequency $f = 457\,\mathrm{kHz}$ is plotted as a function of distance to $z = 800\,\mathrm{mm}$ in Fig. 6.2.

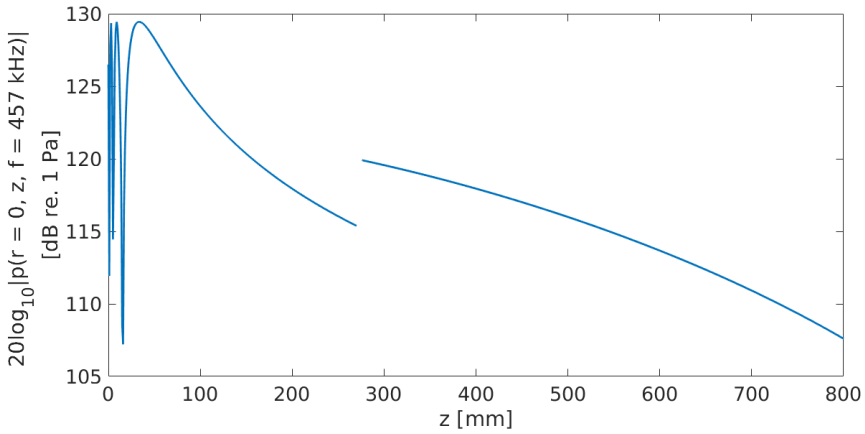

Figure 6.2: The on-axis pressure as a function of distance at $f = 457\,\text{kHz}$ to a distance of $z = 800\,\text{mm}$ with plate. $h_f a = 20$.

The empty space indicates the distance where the plate is situated. The incident pressure has a $1/z$ behavior while the transmitted pressure is clearly different. The behavior is also apparent in the results presented in [27].

In Fig. 6.3. the spatial distribution of the pressure as a function of radial and vertical distance is plotted, using Eq. (2.22), up to a radial distance of 100 mm and a vertical distance of 530 mm from the plate, and $z = 800\,\text{mm}$ from the source. Similarly, Aanes et al. shows this in both the articles [27] [28], though for a Cartesian coordinate system.

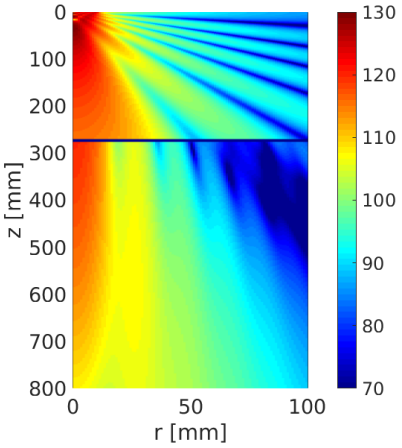

Figure 6.3: The spatial distribution of the pressure at $f = 457\,\text{kHz}$. $h_f a$ is approximately $h_f a = 20$.

The result is similar with Aanes et al., though the pressure magnitude is different. This is due to a different constant velocity chosen on the surface of the piston.

6.2 Nearfield and farfield after plate transmission

Using model 1 and a point receiver, Eq. (2.29 with receiver radius $b \to 0$), the on-axis transmitted pressure as function of distance and frequency is plotted in Fig. 6.4. for frequencies $350\,\text{kHz} \leq f \leq 1000\,\text{kHz}$ from the lower surface of the plate at $z = 276.05\,\text{mm}$, to a distance $z = 3996.05\,\text{mm}$.

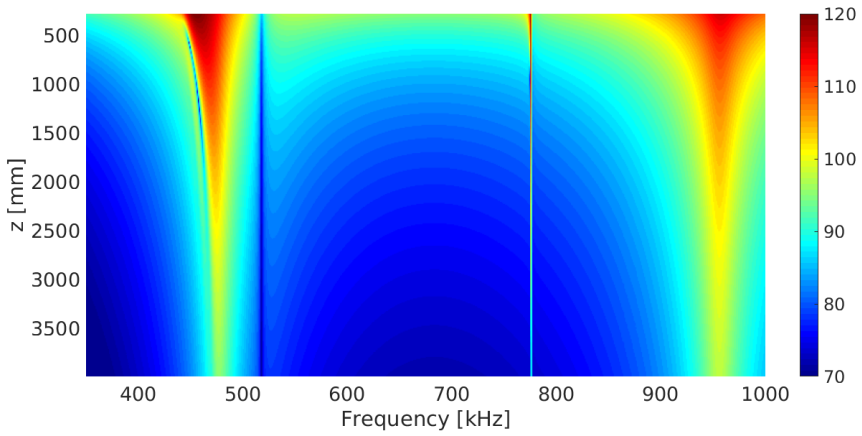

Figure 6.4: The on-axis transmittted pressure for frequencies between $350\,\text{kHz}$ to $1000\,\text{kHz}$ from the distance $z = 276.05\,\text{mm}$ to a distance $z = 3996.05\,\text{mm}$.

The maxima caused by the excitation of the S_{-2}-mode and A_3-mode in the plate, are changing with distance and frequency, which will be discussed in Sec. 6.3. The simulation in Fig. 6.2. can then be extended to $3996.05\,\text{mm}$, see Fig. 6.5.

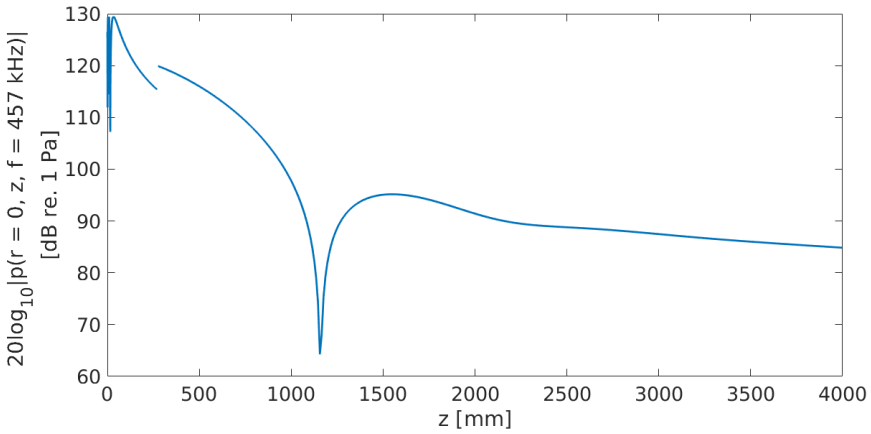

Figure 6.5: The on-axis pressure as a function of distance with frequency $f = 457\,\text{kHz}$ from a distance $z = 0$ to a distance $z = 3996.05\,\text{mm}$. $h_f a = 20$.

Notice that the minimum at approximately $z = 1200\,\text{mm}$ is also visible in Fig. 6.4., which changes with frequency and distance. The transmitted pressure at $z = 276.05\,\text{mm}$ is approximately $4\,\text{dB}$ higher than the incident at $z = 270\,\text{mm}$. Interestingly, the behavior with increasing distance is similar to that which is found in the nearfield of the piston source, with variation of negative and positive interference effects. At approximately $z = 3000\,\text{mm}$ the pressure decays as $1/z$, which is more clear if using the relation given in Eq. (5.2). The results are plotted in Fig. 6.6.

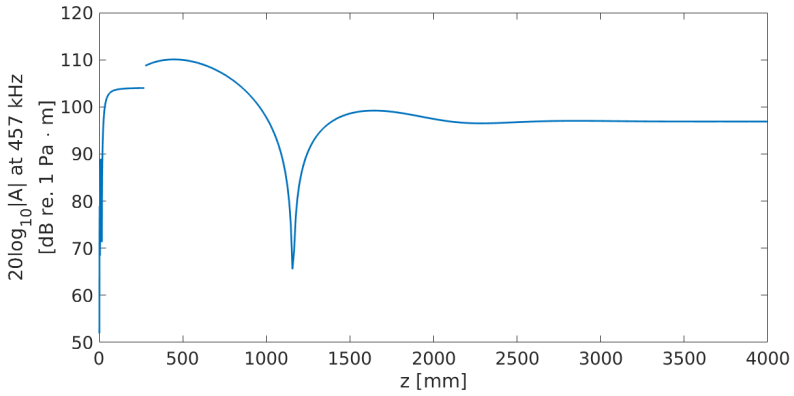

Figure 6.6: The constant A as a function of distance to $z = 3996.05\,\text{mm}$ at $f = 457\,\text{kHz}$. At approximately $z = 3000\,\text{mm}$ A is constant and the pressure decays as $1/z$.

In Fig. 6.4., at $f = 700\,\text{kHz}$, there is no excitation of any leaky Lamb modes in the plate or any significant plate transmission effects, except for a decreased magnitude of the transmitted pressure. The pressure at $f = 700\,\text{kHz}$ as a function of distance is plotted in Fig. 6.7.

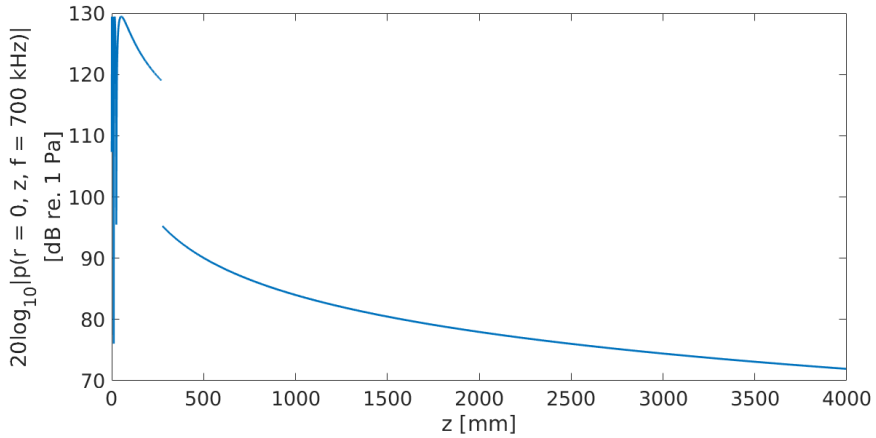

Figure 6.7: The on-axis pressure as a function of distance with frequency $f = 700\,\text{kHz}$ from a distance $z = 0$ to a distance $z = 3996.05\,\text{mm}$.

The transmitted pressure at $z = 276.05\,\text{mm}$ is approximately $25\,\text{dB}$ lower than the incident. The transmitted pressure also decay as $1/z$, see Fig. 6.8.

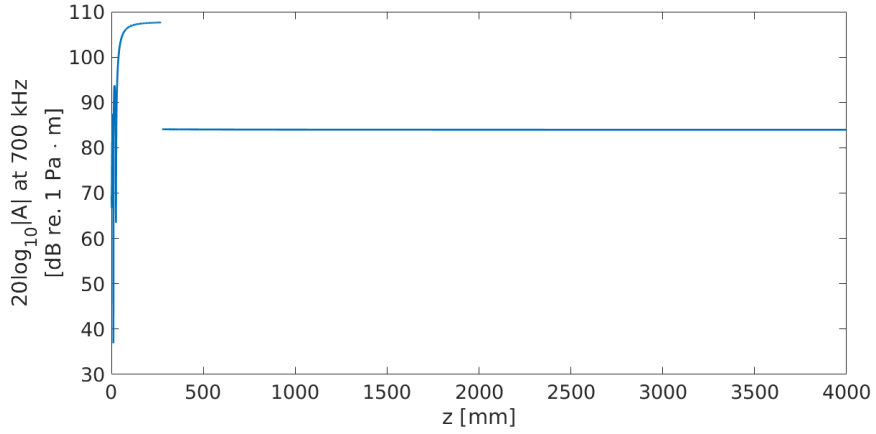

Figure 6.8: The constant A as a function of distance with frequency $f = 700\,\text{kHz}$ from a distance $z = 0$ to a distance $z = 3996.05\,\text{mm}$.

In Fig. 6.9., the pressure as a function of distance at $f = 956\,\text{kHz}$ have been plotted.

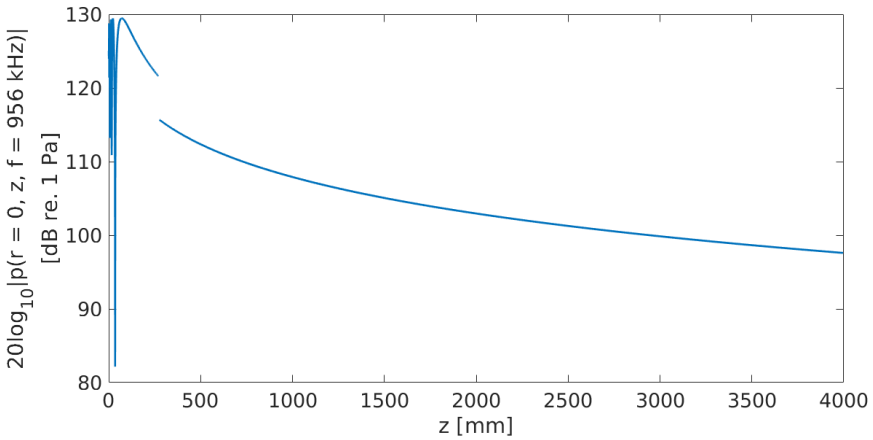

Figure 6.9: The on-axis pressure as a function of distance with frequency $f = 956\,\text{kHz}$ from a distance $z = 0$ to a distance $z = 3996.05\,\text{mm}$.

The transmitted pressure at $z = 276.05\,\text{mm}$ is approximately 6 dB lower than the incident, and there are minimal interference effects. Again the constant A is plotted in Fig. 6.10.

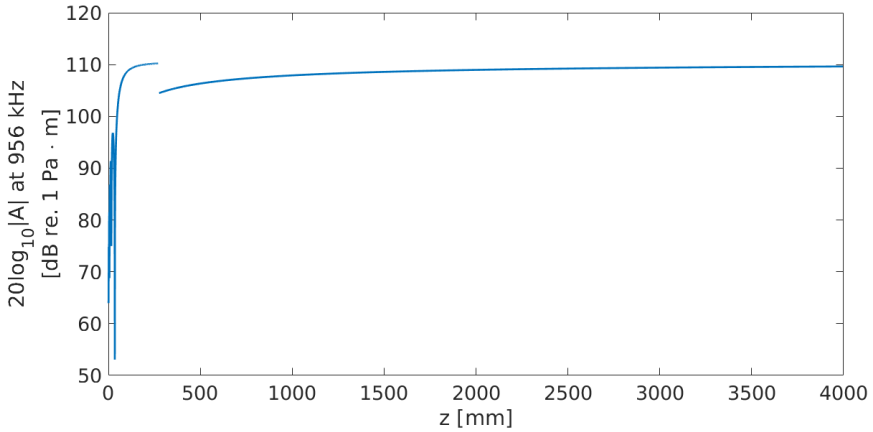

Figure 6.10: The constant A as a function of distance with frequency $f = 956\,\text{kHz}$ from a distance $z = 0$ to a distance $z = 3996.05\,\text{mm}$.

At approximately $z = 2000\,\text{mm}$, the pressure decay as $1/z$.

Quantitatively, Eq. (5.2) can also be used at all the distances and frequencies in Fig. 6.4., where the results are plotted in Fig. 6.11.

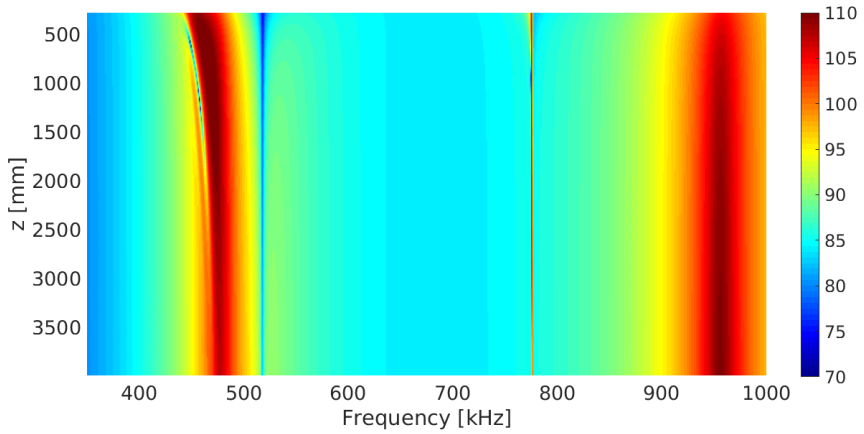

Figure 6.11: The amplitude of the pressure after plate transmission.

A constant color means that the pressure is decaying as $1/z$. The pressure for the range of frequencies associated with the S_{-2}-mode are in general not decaying as $1/z$ just after transmission, though for the pressure at the frequencies associated with the A_3-mode, does (almost) decay as $1/z$ after a relatively short distance. The pressure after transmission have also been simulated using a finite receiver, using Eq. (2.29), see Fig. 6.4.

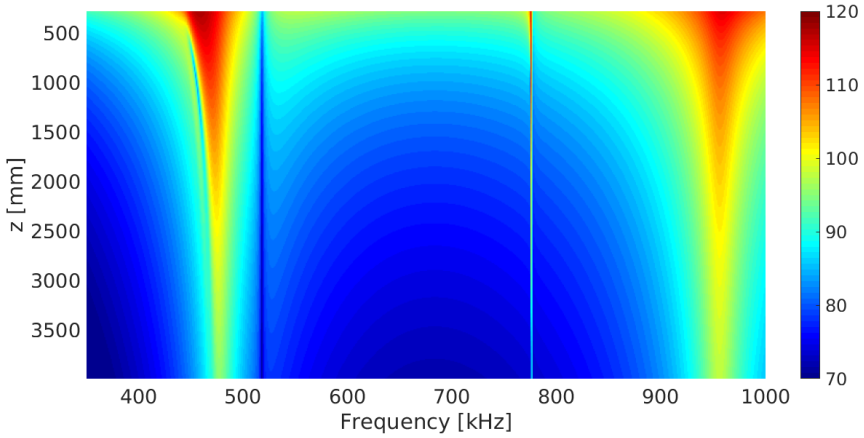

Figure 6.12: The transmittted pressure using a finite receiver for frequencies between 350 kHz to 1000 kHz from the distance $z = 276.05$ mm to a distance $z = 3996.05$ mm.

Again, the transmitted pressure maxima associated the S_{-2}-mode and A_3-mode are changing with distance and frequency. In Fig. 6.13., the pressure with a finite receiver as a function of distance with frequency $f = 457\,\text{kHz}$ is plotted.

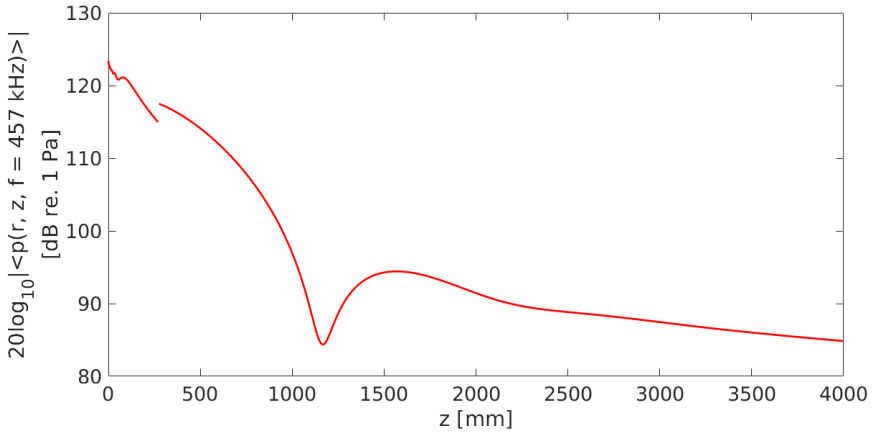

Figure 6.13: The pressure after plate transmission using a finite receiver.

The dynamics with distance is very similar to the point receiver case, which is confirmed if plotted against the point receiver for the same frequency and distances, see Fig. 6.14.

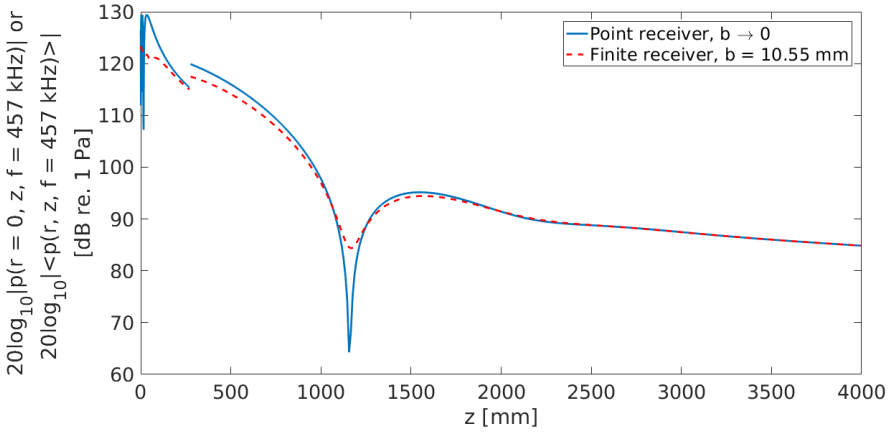

Figure 6.14: The pressure as a function of distance at $f = 457\,\text{kHz}$ using a finite receiver compared to when using a point receiver.

At $z = 270\,\text{mm}$ the pressure at the finite receiver is only approximately

0.5 dB less than the pressure at the point receiver, but because there is a narrowing of the lobe after transmission, as discussed in section 5.7.2, the transmitted pressure using a finite receiver is less, which is approximately 2 dB lower than the pressure at the point receiver. The minimum in Fig. 6.14, when using a finite receiver is interestingly higher than when using a point receiver, which is also apparent in the spatial distribution presented in Fig. 6.15., at the distance $z = 1166\,\text{mm}$ with the frequency $f = 457\,\text{kHz}$.

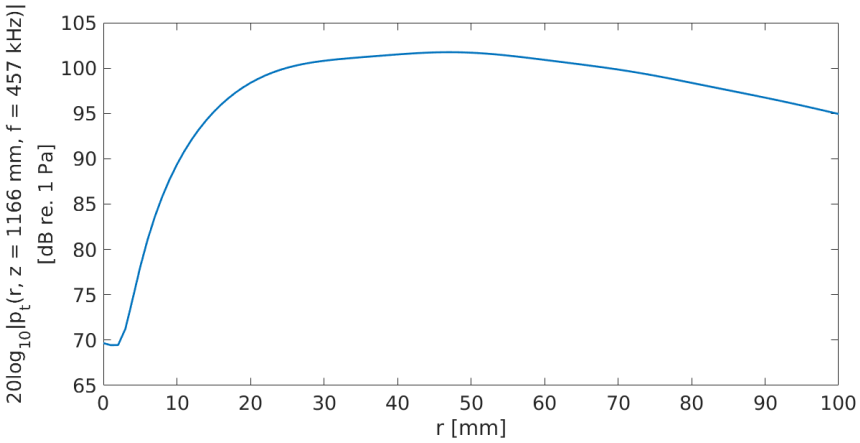

Figure 6.15: The pressure as a function of radial distance after plate transmission at $f = 457\,\text{kHz}$ at the distance $z = 1166\,\text{mm}$.

In Fig. 6.16. the pressures using a point receiver and a finite receiver as a function of distance at $f = 700\,\text{kHz}$ are compared. At $z = 270\,\text{mm}$ the pressure at the finite receiver is approximately 1 dB less than at the point receiver, and at $z = 276.05\,\text{mm}$ the transmitted pressure at the finite receiver is also approximately 1 dB lower than the pressure at the point receiver.

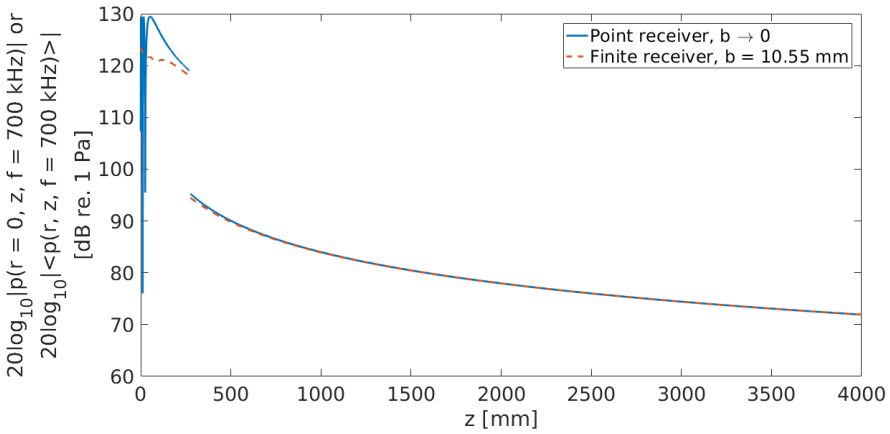

Figure 6.16: The pressure as a function of distance after plate transmission at $f = 700\,\text{kHz}$ using a finite receiver compared to when using a point receiver.

In Fig. 6.17. the pressures using a point receiver and a finite receiver as a function of distance at $f = 956\,\text{kHz}$ are compared.

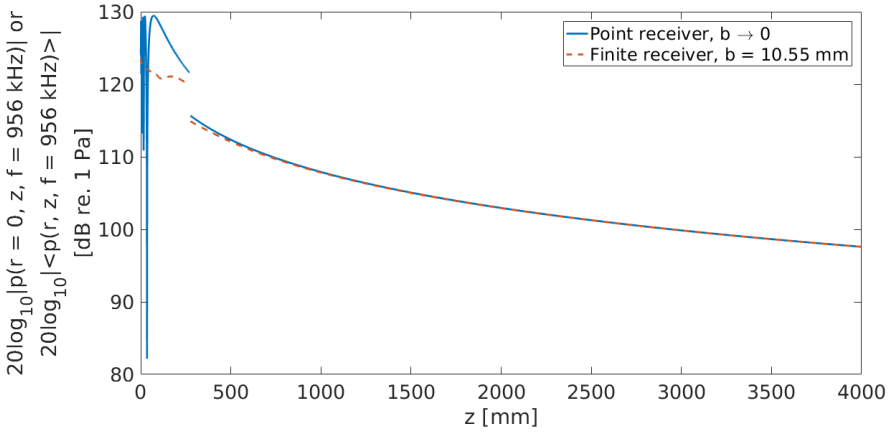

Figure 6.17: The pressure as a function of distance after plate transmission at $f = 956\,\text{kHz}$ using a finite receiver compared to when using a point receiver.

The incident pressure at $z = 270\,\text{mm}$ at the finite receiver is approximately 2 dB less than at the point receiver, while the pressure is only approximately 0.4 dB less at $z = 276.05\,\text{mm}$. This is due to the widening of the beam, as discussed in Sec. 5.7.

6.3 Frequency shift of maximum on in the transmitted pressure

In the previous section it was stated that the maximum of transmitted pressure changes with frequency and distance. This section will show this more clearly. The case when having a point receiver will be discussed in order to generalize the results.

In Fig. 6.18., the figure in the last section, Fig. 6.4., is again plotted, but with a tracing of the maxima on the respective modes.

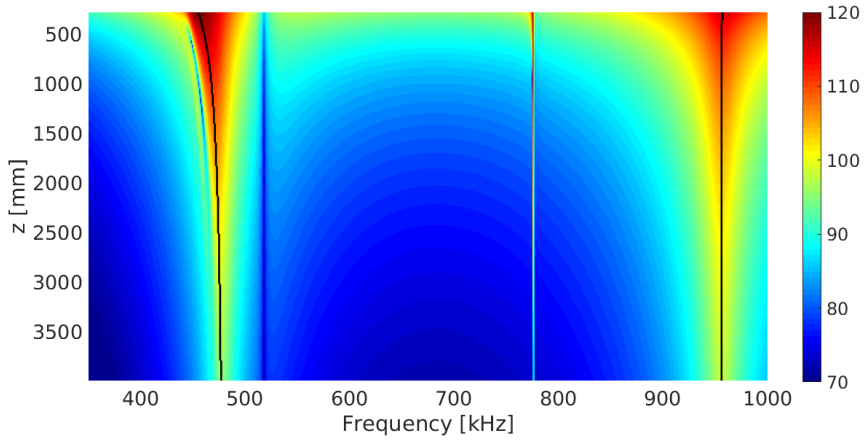

Figure 6.18: The pressure after transmission as a function of distance and frequency. The black lines represent the tracing of maxima.

The frequencies of maximum transmission at 276.05 mm and 3996.05 mm are given in Tab. 6.1.

Table 6.1: The frequencies of maximum transmission at the minimum and maximum distance of Fig. 6.18.

z [mm]	S_{-2} [kHz]	A_3 [kHz]
276.05	455	957
3996.05	477	955

The frequencies of maximum transmission at the their respective end-distances are the predicted frequencies of maximum transmission when

using the plane-wave approximation with the transmission coefficient, as seen in Sec. 6.1., Fig. 6.1.

The pressure at the two distances as function of frequency are plotted in Fig. 6.19. They have been normalized with their maximum pressure value in order to compare the two.

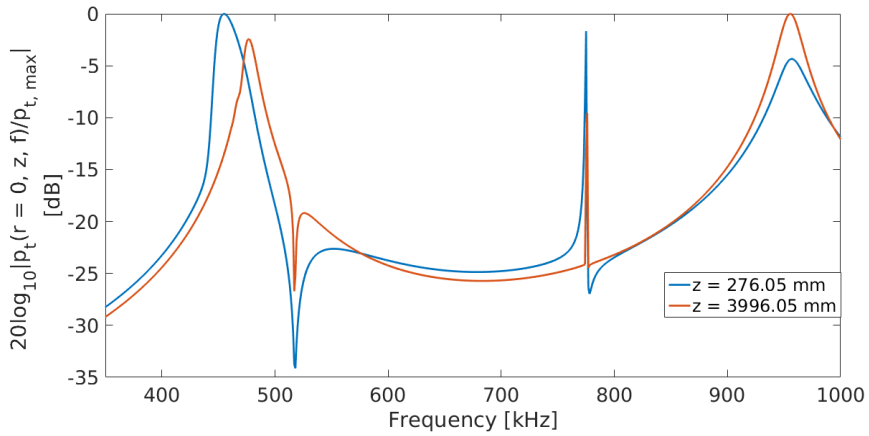

Figure 6.19: The pressure as a function of frequency at distances $z = 276.05\,\text{mm}$ and $z = 3996.05\,\text{mm}$.

The pressure as a function of distance for the two frequencies $f = 455\,\text{kHz}$ and $f = 477\,\text{kHz}$ are plotted in Fig. 6.20.

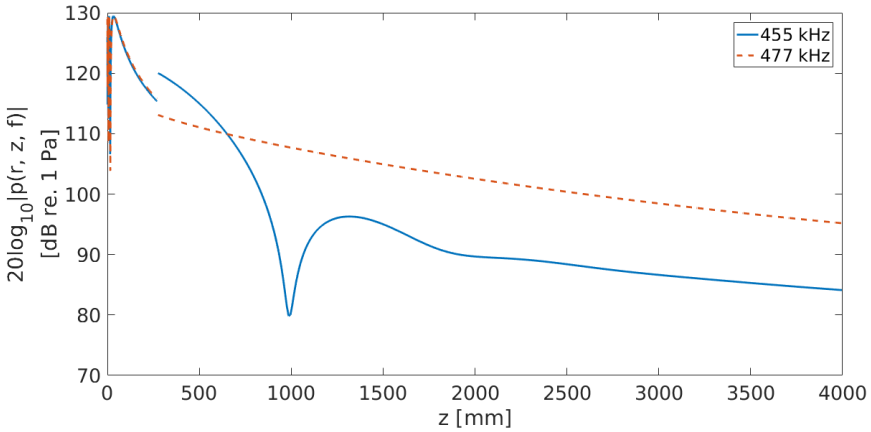

Figure 6.20: The pressure as a function of distance with frequencies $f = 455\,\text{kHz}$ and $f = 477\,\text{kHz}$.

Two measurements were performed in an attempt to confirm that the frequency change is a fact, though the current setup in the laboratory is not eligible for measurements at distances bigger than approximately 875 mm between the source and receiver. In Fig. 6.21. the transfer function $H_{pp}(f)$ was measured for a distance of 626 mm as a function of frequency and compared with simulations.

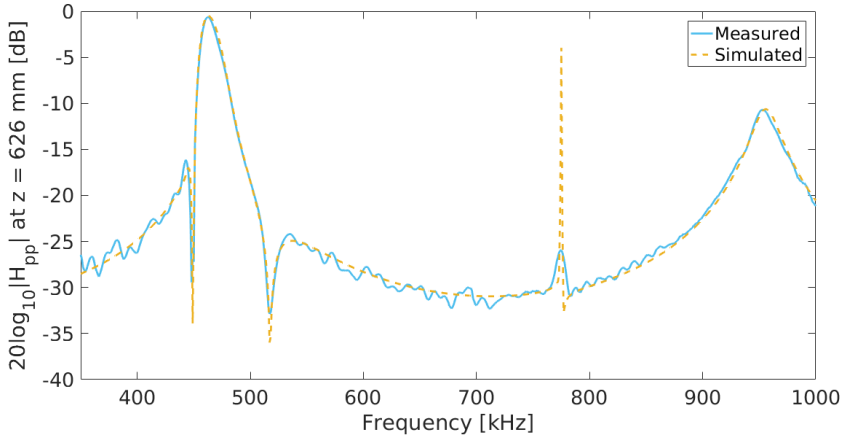

Figure 6.21: $|H_{pp}(f)|$ measured compared with simulation as a function of frequency with $z = d_T + d_R = 626$ mm.

The frequencies of maximum and minimum transmission are given in Tab. 6.2 for the measurement and simulation.

Table 6.2: The frequencies of maximum transmission for measured $H_{pp}(f)$ at $z = d_T + d_R = 626$ mm.

Label:	Simulated [kHz]	Measured [kHz]
S_{-2}	463	463
S_2	517	517
A_2	775	775
A_3	956	953

The transfer function with the receiver at $z = 875$ mm was also measured, and the resulting transfer function compared to simulations is given in Fig. 6.22.

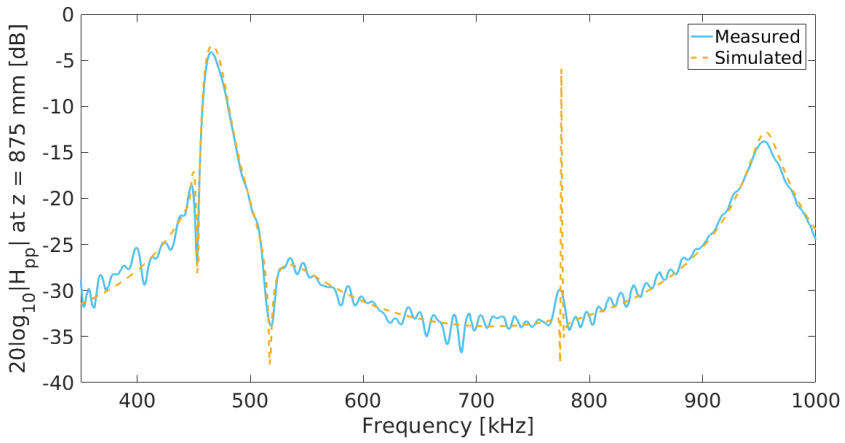

Figure 6.22: $|\mathrm{H_{pp}}(f)$ measured compared with simulation as a function of frequency with $z = d_T + d_R = 875\,\mathrm{mm}$.

The frequencies of minimum and maximum transmission are given in Tab. 6.3.

Table 6.3: The frequencies of maximum transmission for $\mathrm{H_{pp}}(f)$ at $z = d_T + d_R = 875\,\mathrm{mm}$.

Label:	Simulated [kHz]	Measured [kHz]
S_{-2}	465	466
S_2	519	517
A_2	773	775
A_3	955	955

Compared to the measurement with the receiver at $z = 626\,\mathrm{mm}$, the magnitudes are lower than the simulated magnitude. However, the measured magnitudes are less than 1 dB at S_{-2}-mode and A_3-mode. The trend in the measurements is that the frequencies of maximum transmission associated with the excitation of the these modes in the plate, change with increasing distance from the plate, though this should be confirmed for an even bigger distance, preferably at $z = 3996.05\,\mathrm{mm}$.

In the following sections, Sec. 6.3.1. and Sec. 6.3.2., an analysis that tries to explain why there is a frequency change of the maximum on S_{-2} will be performed. This is done by analysis of magnitude and phase of the angular spectrum, before a hypothesis on the physical interpretation is given.

6.3.1 Magnitude and phase at 455 kHz

As shown in Sec. 5.1.1., the angular spectrum does not change with distance, except for a faster decaying evanescent part. In Fig. 6.23., the magnitude of the angular spectra of the pressures at the distances 276.05 mm and 3996.05 mm with $f = 455$ kHz are plotted.

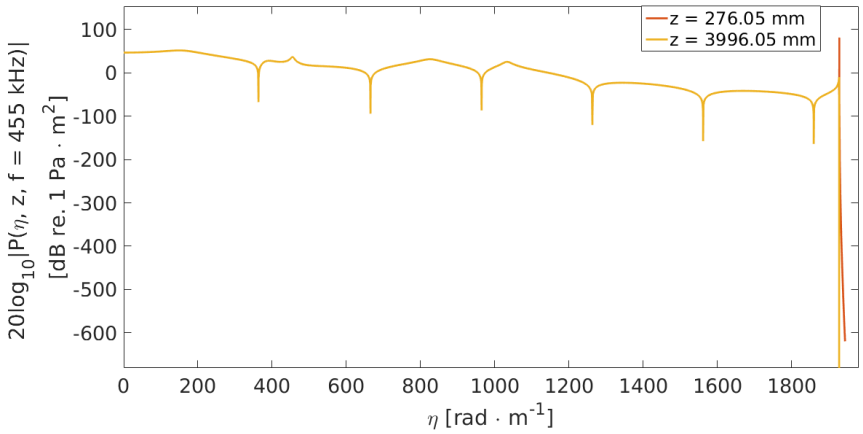

Figure 6.23: The magnitudes of angular spectra of pressure at the distances 276.05 mm and 3996.05 mm.

This means that in order to explain why the spatial pressure is different at this frequency at the two distances, besides the physical and obvious reason that the pressure decays as a function of distance, the answer lies within the phase of the respective distances.

Before going into the analysis of the phase, MATLAB® has a function that comes in handy as a tool of analysis. Additionally to their function *trapz()*, they also have a *cumtrapz()* function, which is an accumulated integration; it shows all the steps in the trapezoidal integration as function of the integration variable, in this case η. With this, it is possible to see exactly which parts of the magnitude and phase of the angular spectrum that contributes for the final integrated value. As an example, the results of this function can be seen in Fig. 6.24., where the function have been used for the integrand of Eq. (2.29 with $b \to 0$) at $f = 455$ kHz at distance $z = 276.05$ mm.

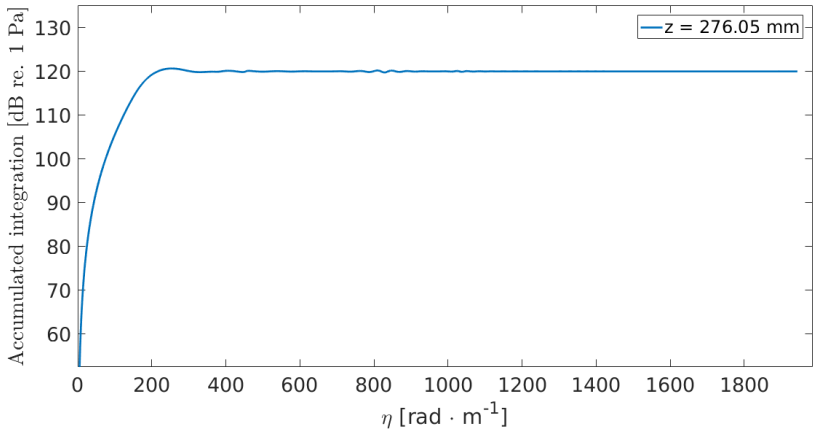

Figure 6.24: The magnitude of the accumulated integration of Eq. (2.29 with $b \to 0$) at $f = 455\,\mathrm{kHz}$ at the distance $z = 276.05\,\mathrm{mm}$.

From approximately $\eta = 300\,\mathrm{rad} \cdot \mathrm{m}^{-1}$ the magnitude and phase in the integration basically have negligible influence on the final value at $\eta_{max} \approx 1940\,\mathrm{rad} \cdot \mathrm{m}^{-1}$. In order to understand this, all the steps from the incident wave to the transmitted wave needs to be investigated, by looking at the magnitude and phase of the angular spectrum in the individual steps. The magnitude and phase of the angular spectrum of the incident wave at frequency $f = 455\,\mathrm{kHz}$ at $z = 270\,\mathrm{mm}$ is plotted in Fig. 6.25.

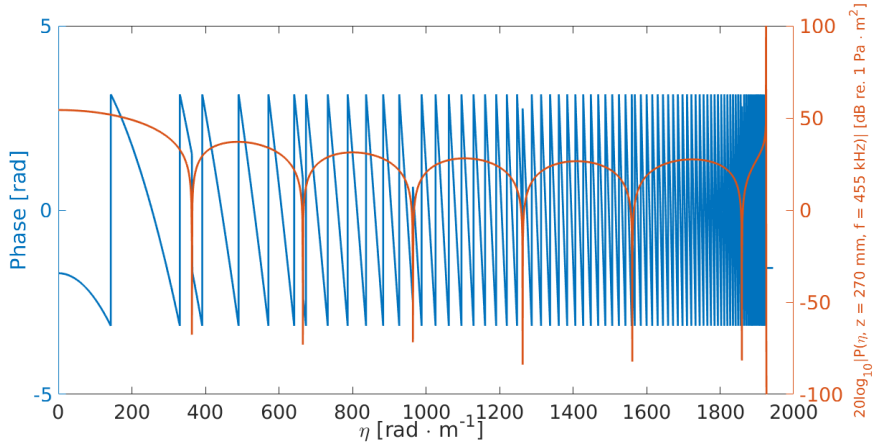

Figure 6.25: The magnitude and phase of $P_T(\eta, z = 270\,\mathrm{mm}, f = 455\,\mathrm{kHz})$ with $f = 455\,\mathrm{kHz}$ at the distance $z = 270\,\mathrm{mm}$. $h_f a = 20$.

Note that the phase for low η has a small rate of change until the phase is equal to the first $-\pi$, and that this is unique compared to the rest of the phase. This part of the phase between $\eta = 0$ and $\eta = \eta_{-\pi,1}$ where $\eta_{-\pi,1}$ is the wavenumber where the phase first equals $-\pi$, will therefore be termed as "the unique phase". In Fig. 6.26., the magnitude and phase of Fig. 6.25. are zoomed in for the wavenumbers between $\eta = 0$ and $\eta = 1400\,\mathrm{rad} \cdot \mathrm{m}^{-1}$ in order to compare with the transmission coefficient in the following.

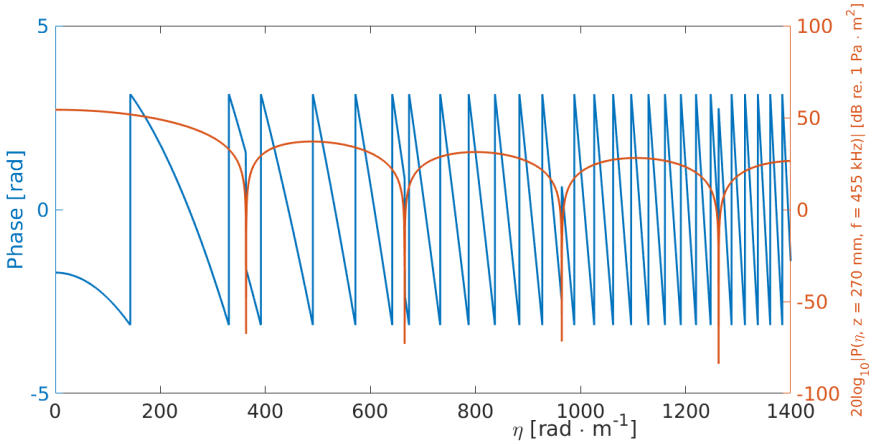

Figure 6.26: Zoomed in on Fig. 6.25.

The incident magnitude and phase, changes when multiplied with the transmission coefficient, where the magnitude and phase of the tranmission coefficient is given in Fig. 6.27, along with a labeling of the associated leaky Lamb modes of the different maxima in the spectrum. The transmission coefficient is relative, so the phase represents the phase-difference between the transmitted and incident pressure. It is the phase-difference which gives the characteristic increase of transmitted pressure, which will be explained. Notice that the phase of the transmission coefficient rises before exciting the S_{-2}-mode, while the phase of the incident angular spectra in Fig. 6.26. decreases almost within the same interval of η. Adding these two together will give an almost constant rate of change, because the rate of change to the phase in the transmission coefficient for $\eta \leq \eta_{S_{-2}}$ is approximately equal to the rate of change in the incident phase for $\eta \leq \eta_{-\pi,1}$, though with opposite signs.

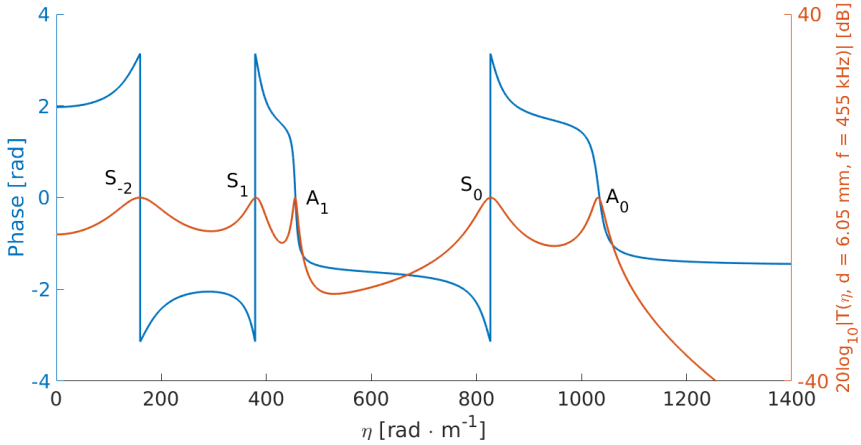

Figure 6.27: The magnitude and phase of the transmission coefficient at $f = 455\,\mathrm{kHz}$.

The sum of the rate of change in the phases are plotted in Fig. 6.28. for $\eta \leq 200\,\mathrm{rad \cdot m^{-1}}$.

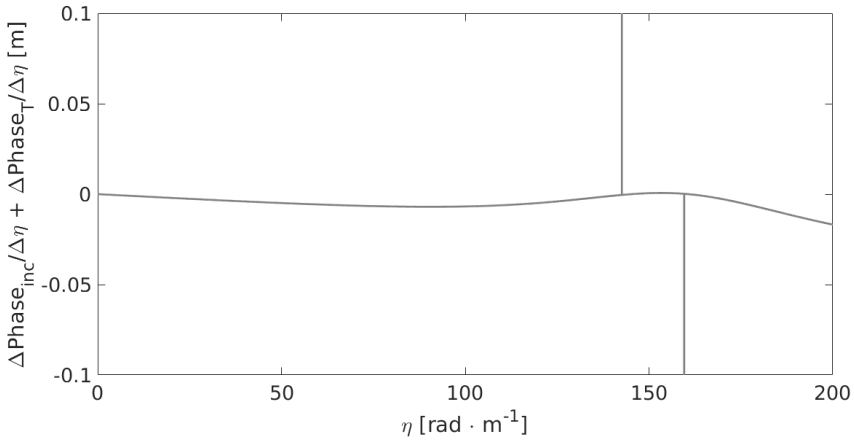

Figure 6.28: The sum of rate of change to the phases of the angular spectrum of the incoming wave at $z = 270\,\mathrm{mm}$ and the transmission coefficient at $f = 455\,\mathrm{kHz}$.

The spikes around $\eta \approx 150\,\mathrm{rad \cdot m^{-1}}$ are caused by the high rate of change as the phase jumps from $-\pi$ to π. When adding the phase-difference of the transmission coefficient to the phase of the angular spectrum, this will introduce an almost constant phase with respect to η in the transmitted angular spectrum, within this interval of η. In

Fig. 6.29. the magnitudes of the angular spectra at the upper and lower side of plate are plotted together at the frequency $f = 455\,\text{kHz}$.

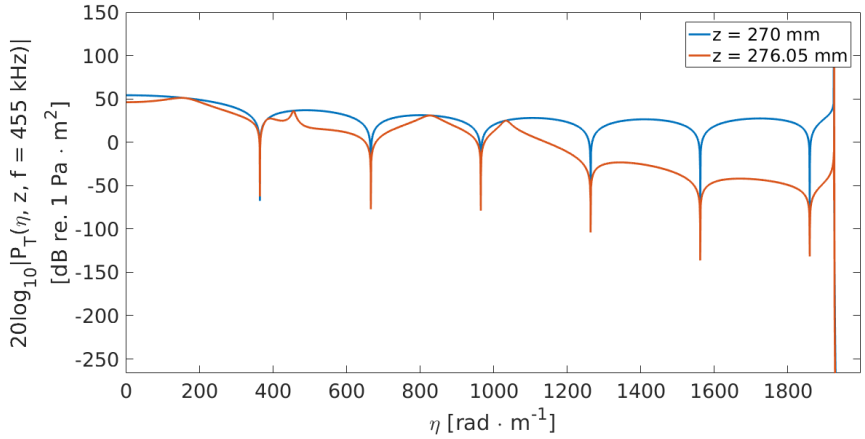

Figure 6.29: The magnitude and the angular spectrum at $f = 455\,\text{kHz}$ at the distances $z = 270\,\text{mm}$ and $z = 276.05\,\text{mm}$.

The magnitude of the spectrum at the lower side is generally less than the upper side. In Sec. 6.1., Fig. 6.1., it was seen that the transmitted pressure at $f = 455\,\text{kHz}$ was larger than the incident. This means that the increase of the pressure in space at the lower side, has to be due to the difference of phase in the angular spectrum, considering the magnitude of the transmitted angular spectrum is generally less than the incident angular spectrum. In Fig. 6.30., the phase and magnitude of the spectrum at the lower side of the plate is plotted. The unique phase has an even smaller rate of change compared to the unique phase at the upper side, which was predicted in Fig. 6.28. In Fig. 6.31 the rate of change for the two phases at $z = 270\,\text{mm}$ and $z = 276.05\,\text{mm}$ for $\eta \leq 200\,\text{rad} \cdot \text{m}^{-1}$ are plotted.

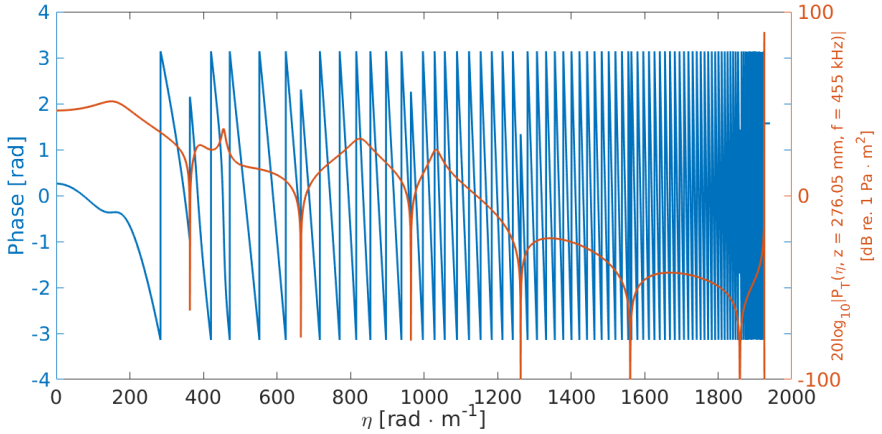

Figure 6.30: The magnitude and phase of the angular spectrum at $f = 455\,\text{kHz}$ at the distance $z = 276.05\,\text{mm}$.

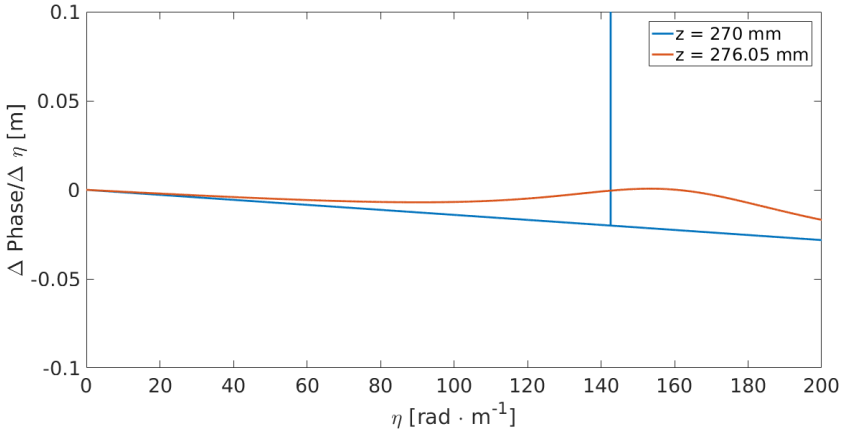

Figure 6.31: The rate of change of the phase of the angular spectra at $f = 455\,\text{kHz}$ at the distance $z = 270\,\text{mm}$ and $z = 276.05\,\text{mm}$.

The phase at the lower side stays approximately constant for a bigger interval of η compared to the upper side. Finally if the accumulated integration is compared for the two, the unique phase reveals its importance, see Fig. 6.32.

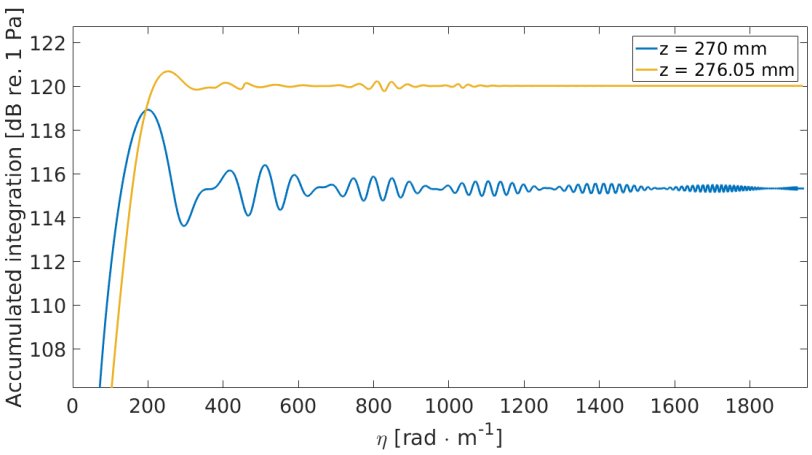

Figure 6.32: The accumulated integration at $f = 455\,\text{kHz}$ at the distance $z = 270\,\text{mm}$ and $z = 276.05\,\text{mm}$.

This, with the phase-differences in Fig. 6.31., suggests that the small rate of change for the unique phase at the lower side of the plate, introduces more constructive interference in the integration, compared to the integration on the upper side of the plate. Then as η becomes bigger, the rest of the phase introduces a periodic extinction of the magnitude-components in the integration, which effectively means that the unique phase is the determining factor for the spatial value of the pressure. The reason that there is less oscillations of the accumulated integration at the lower side as η becomes bigger and the phase becomes periodic, is because the accumulated value achieved for low η is high relative to the rest of the magnitude in the spectrum, so the periodicity of the phase affects the integration less.

Furthermore, if the spectrum and phase at $z = 3996.05\,\text{mm}$ is drawn into the comparisons, similar arguments can be used to understand why the pressure is less at this distance compared to $276.05\,\text{mm}$. The phase and magnitude at $z = 3996.05\,\text{mm}$ of frequency $f = 455\,\text{kHz}$ are shown in Fig. 6.33.

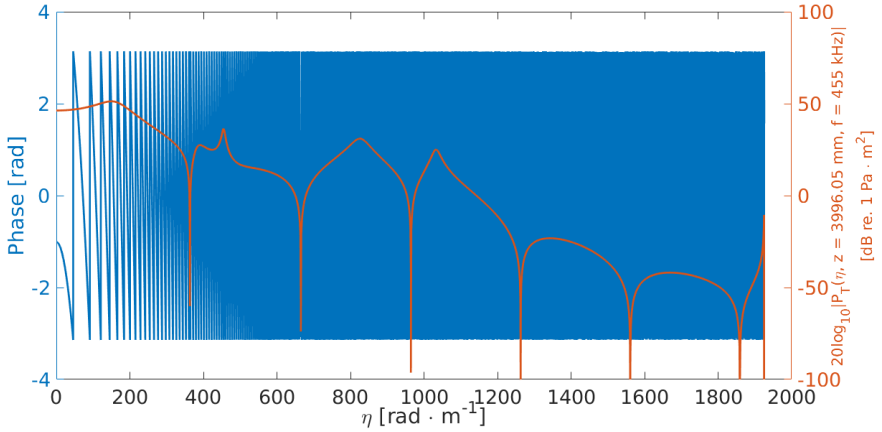

Figure 6.33: The magnitude and phase of the angular spectrum at $f = 455\,\text{kHz}$ at the distance $z = 3996.05\,\text{mm}$.

Note that the interval of η for the unique phase at $z = 3996.05\,\text{mm}$, does not include the S_{-2}-peak in the magnitude of the spectrum. The phase for low η from Fig. 6.33. is compared with the phase at 276.05 mm, in Fig. 6.34.

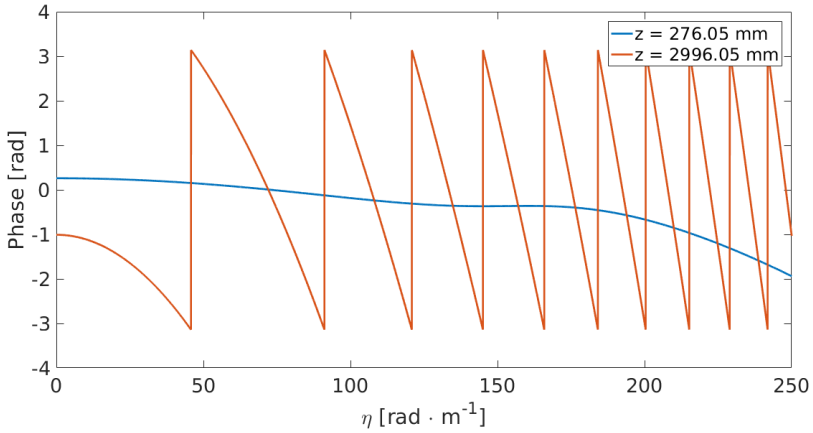

Figure 6.34: The phase for low η of the angular spectrum at $f = 455\,\text{kHz}$ at the distance $z = 276.05\,\text{mm}$ and $z = 3996.05\,\text{mm}$.

Once again, the phase at 276.05 mm has a low rate of change, compared to the rate of change of the phase at 3996.05 mm. The accumulated integration at these two distances are shown in Fig. 6.35.

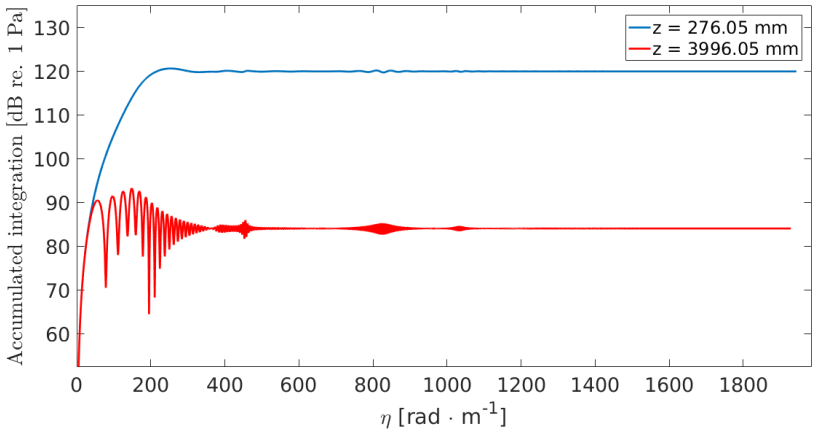

Figure 6.35: The magnitude of the accumulated integration of the integrand at $f = 455\,\text{kHz}$ at the distance $z = 276.05\,\text{mm}$ and $z = 3996.05\,\text{mm}$.

The results in Fig. 6.35. confirms that when the magnitude of the accumulated value for the unique phase is low relative to the rest of the magnitude of the angular spectrum, there are great interference and variation throughout the accumulated integration. The accumulated integrated value achieved for the distance $z = 3996.05\,\text{mm}$ for the interval for the unique phase (approximately for $\eta \leq 50\text{rad} \cdot \text{m}^{-1}$) is low relative to the magnitude of the spectrum. However, the main attribute to notice, is that as z increases, the unique phase has a faster rate of change, which means that the unique phase will exist for a smaller and smaller range of η. Then, as $\eta_{-\pi,1}$ becomes smaller and goes toward $\eta = 0$, the contribution of the S_{-2}-peak in the magnitude of the angular spectrum will disappear from the integration, and the pressure behaves as if there was a single, normally incident plane wave to the plate. Similar behavior is shown in Sec. 6.3.2.

6.3.2 Magnitude and phase at 477 kHz

This section will use the same arguments in Sec. 6.3.1. for the same distances, but at the frequency $f = 477\,\text{kHz}$.

In Fig. 6.36. the phase and magnitude of the angular spectrum on the upper side, $z = 270\,\text{mm}$ are plotted.

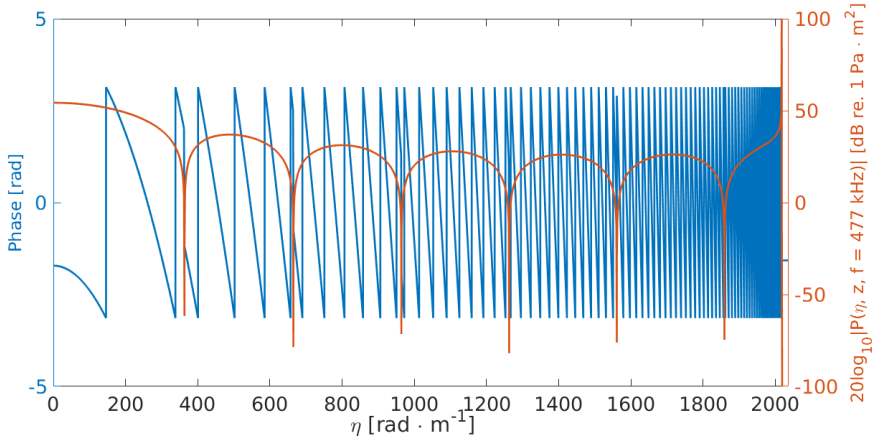

Figure 6.36: The phase and magnitude of the angular spectrum at $f = 477\,\text{kHz}$ at the distance $z = 270\,\text{mm}$. $h_f a = 21$.

This shows very similar results compared to the case at $f = 455\,\text{kHz}$ in Fig. 6.25. However, the transmitted angular spectrum will be different, where the phase and magnitude of the transmission coefficient at $f = 477\,\text{kHz}$ are plotted in Fig. 6.37.

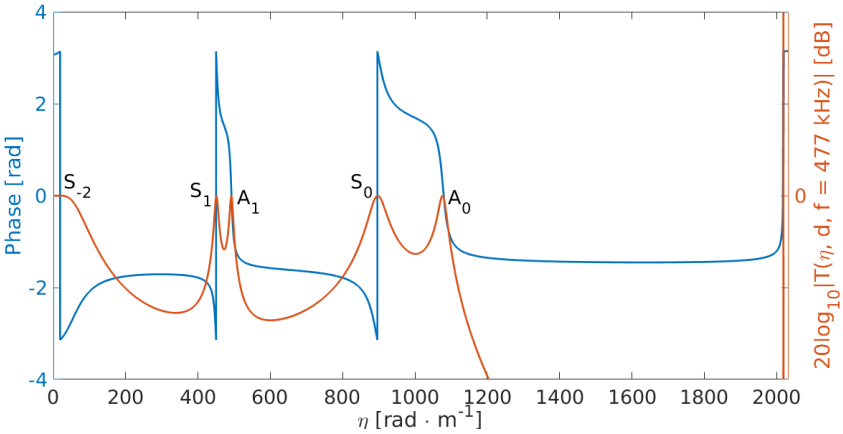

Figure 6.37: The phase and magnitude of the transmission coefficient at $f = 477\,\text{kHz}$

The S_{-2}-mode is now excited for a smaller wavenumber of the incident wave as compared with frequency $f = 455\,\text{kHz}$, which causes the maximum in the angular spectrum at the lower side of the plate to

change accordingly. This can be seen in Fig. 6.38., where the phase and magnitude of the angular spectrum at $z = 276.05\,\text{mm}$ are plotted.

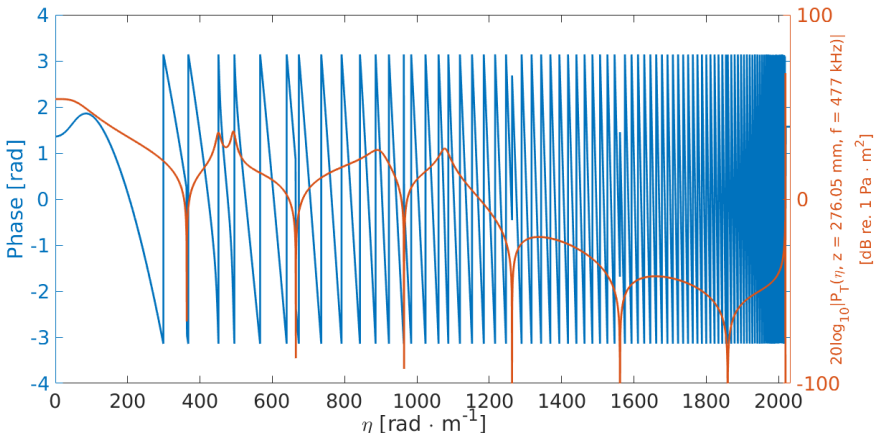

Figure 6.38: The phase and magnitude of the angular spectrum at $f = 477\,\text{kHz}$ at the distance $z = 276.05\,\text{mm}$.

The magnitude of maximum transmission is now for a interval starting at $\eta = 0$, with an almost constant magnitude up until $\eta \approx 50\,\text{rad}\cdot\text{m}^{-1}$. The phase, as opposed to the case at $f = 455\,\text{kHz}$, has a rate of change that is higher, when compared to the incident phase, in the interval of the unique phase, see Fig. 6.39.

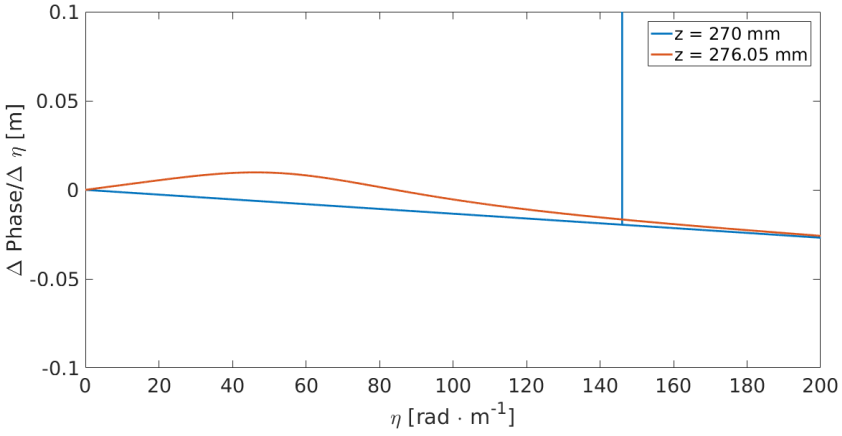

Figure 6.39: The rate of change of the phase at $f = 477\,\text{kHz}$ at the distance $z = 270\,\text{mm}$ and $z = 276.05\,\text{mm}$.

The magnitude of the incident angular spectra and the transmitted

angular spectrum for this interval of η are plotted in figure 6.40.

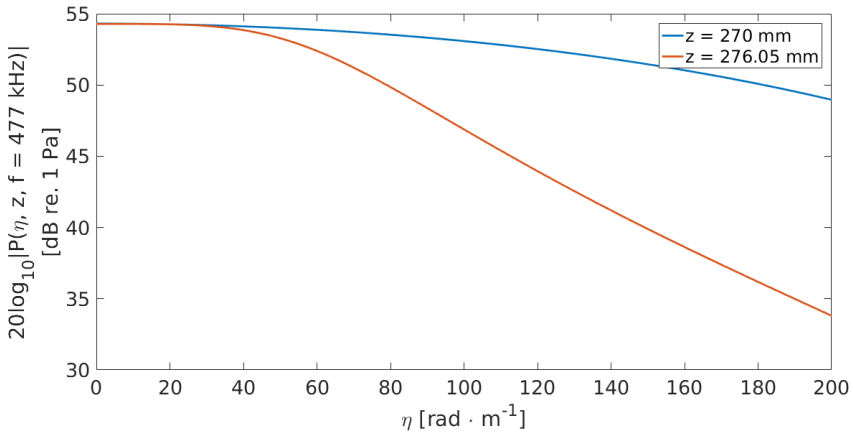

Figure 6.40: The magnitude of the angular spectrum at $f = 477\,\text{kHz}$ at the distance $z = 270\,\text{mm}$ and $z = 276.05\,\text{mm}$.

For the case at $f = 455\,\text{kHz}$, it was seen that the unique phase is the determining factor for the value of the spatial pressure. The spatial pressure was higher on the lower side, even though the magnitude of the angular spectrum in the interval of the unique phase was generally lower than the incident; the unique phase was more constant with respect to η than the incident phase, which introduced more constructive interference in the integration than at the incident side. Analogously at $f = 477\,\text{kHz}$, the magnitude of the angular spectrum in the interval of the unique phase on the lower side is generally lower than the incident; the unique phase however, is less constant than the incident side, which introduces more destructive interference in the integration than at the incident side. This gives a spatial pressure which is less on the lower side of the plate. The accumulated integration at $f = 477\,\text{kHz}$ for the two distances are plotted in Fig. 6.41., which also confirms this.

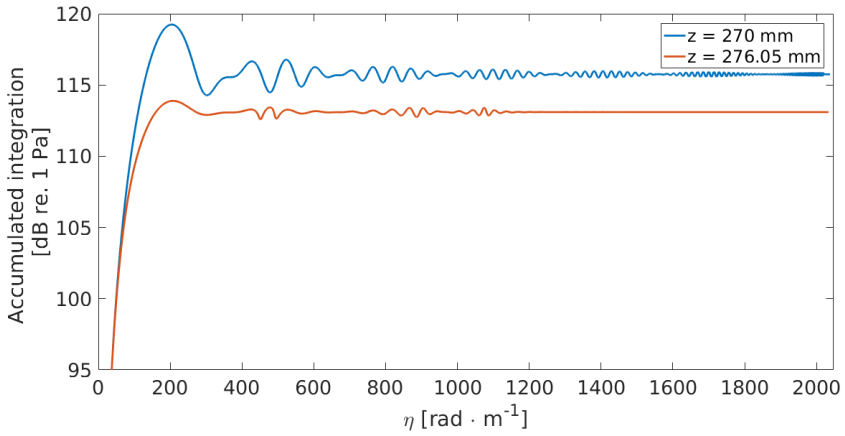

Figure 6.41: The magnitude of the accumulated integration at $f = 455\,\text{kHz}$ at the distance $z = 276.05\,\text{mm}$ and $z = 3996.05\,\text{mm}$.

It was stated in the last section that as z increases, the wavenumber $\eta_{-\pi,1}$ goes toward zero, i.e., towards the plane-wave component in the angular spectrum. With this, the reason to why there is a frequency shift of the maximum - why the pressure at the distance $z = 3996.05\,\text{mm}$ for the frequency $f = 477\,\text{kHz}$ is higher than the pressure at frequency $f = 455\,\text{kHz}$ at the same distance - can be explained. The magnitude and phase of the angular spectrum at $z = 3996.05\,\text{mm}$ for the frequency $f = 477\,\text{kHz}$ is plotted in Fig. 6.42.

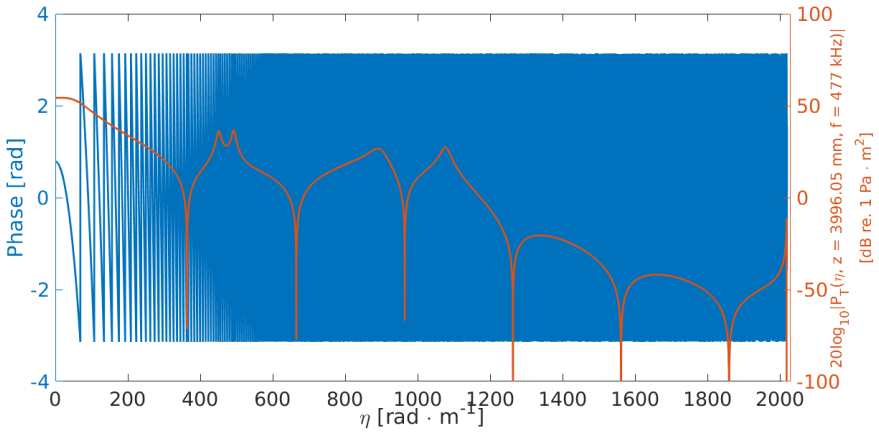

Figure 6.42: The magnitude of the accumulated integration at $f = 455\,\text{kHz}$ at the distance $z = 276.05\,\text{mm}$ and $z = 3996.05\,\text{mm}$.

The unique phase is close to $\eta = 0$, and in this case, as a opposed to the same distance with frequency $f = 455\,\text{kHz}$, the maximum due to excitation of the S_{-2}-mode is included within the interval of the unique phase. A comparison between the magnitude and phase of the angular spectrum at $z = 3996.05\,\text{mm}$ for the frequencies $f = 455\,\text{kHz}$ and $f = 477\,\text{kHz}$ for $\eta \leq 200\,\text{rad} \cdot \text{m}^{-1}$, is presented in Fig. 6.43. and Fig. 6.44, respectively

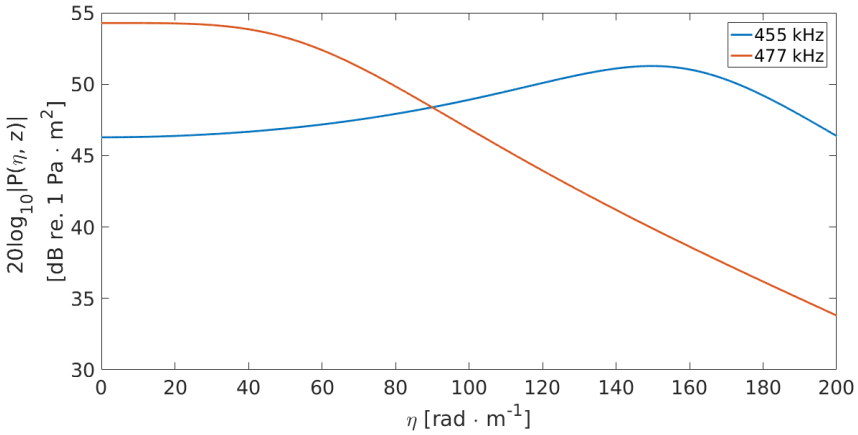

Figure 6.43: Zoomed in on the magnitude for small η of the angular spectrum at $f = 455\,\text{kHz}$ compared with the magnitude of the angular spectrum at $f = 477\,\text{kHz}$.

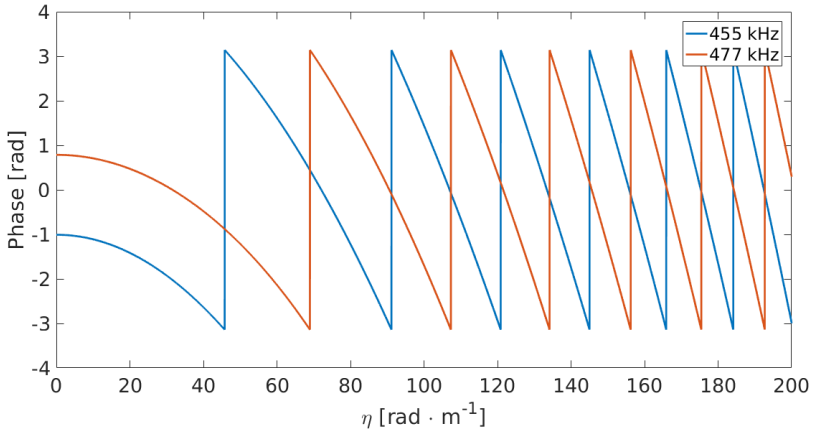

Figure 6.44: Zoomed in on the phase of the angular spectrum at $f = 455\,\text{kHz}$ compared with the magnitude of the angular spectrum at $f = 477\,\text{kHz}$.

In both cases, the unique phase will give a constructive interference for a short interval of η. The significant difference however, is that the maximum for the magnitude of the angular spectrum at $f = 455\,\text{kHz}$ is not included within this interval of η, while the maximum at $f = 477\,\text{kHz}$ is included within this interval. The result is a bigger spatial pressure, i.e. a shift of frequency for the maximum spatial pressure after transmission at the distance $z = 3996.05\,\text{mm}$.

To summarize, it was seen that when increasing the distance between the plate and point receiver, the unique phase, which is the determining factor for the value of the spatial pressure, goes towards $\eta = 0$. This means that the spatial value relies more and more on the magnitude of the angular spectrum close to $\eta = 0$, i.e., the magnitude of the normally incident plane wave. A physical interpretation of this, may be that when the receiver is close to the plate, the on-axis component is afflicted by interference effects because of the excitation of backward wave mode in the plate [28][29]. Then as the receiver moves further and further away from the plate, and thus the interference region, it is only receiving the on-axis component which was normally incident to the plate, which also had a plane-wave like condition on the wavefront because the plate is in the farfield of the source. In other words, the maximum transmission is at $f = 477\,\text{kHz}$ when the receiver is a great distance from the plate, but in the nearfield of the plate, the on-axis component received is afflicted by interference. This is however not confirmed and remains a hypothesis, and should be further investigated, e.g, by a similar study when exciting the A_3-mode of the plate.

Chapter 7

Conclusion and further work

A short summary and conclusions of the results in the thesis are given in Sec. 7.1., before some further work are proposed in Sec. 7.2.

7.1 Observations and conclusions

Three ASM-type of models based on the baffled piston model and developed for the case of plate transmission with a finite receiver, were derived and implemented in MATLAB® to use in simulations. The first model, model 1, which was developed for the thesis, used a constant velocity on the surface of the piston, which in turn were used to solve for the transmitted average pressure at the surface of a finite receiver in cylindrical coordinates. The second model, model 2, developed by Anderson and Martin, also used a constant velocity on the surface of the piston, and then solved for the average transmitted pressure at the surface of a finite receiver in Cartesian coordinates. The third and final model, model 3, developed by Orofino and Pedersen/Waag, used a constant pressure on the surface of the piston and then solved for the transmitted normal average particle velocity on the surface of a finite receiver. The models were compared, without plate, against models independent of the ASM, with an expression for the on-axis pressure using a point receiver, given by Kinsler et al. [30], and an expression for the average pressure on the surface of a finite receiver, given by Williams [38]. Discussions concerning differences when compared with the ASM independent models ensued, before model 1, model 2 and model 3 were compared against each other in the case of plate trans-

mission. Following this, a study on the influence of a finite receiver both with and without plate were performed, in comparison with a point receiver. Finally, the transmitted pressure when increasing the distance between the plate and receiver was simulated and presented, along with some discussions concerning the phenomenons observed.

When comparing model 1 with the models by Kinsler et al. and Williams without plate, it was shown overall good agreement in the comparisons. It was also shown that the exclusion of evanescent waves is not a good approximation for low frequencies, but gave better results for higher frequencies, especially in the farfield. This is because the evanescent waves decay faster with increasing distance and frequency, which means that they contribute less in the integration, and thus contribute less for the value of the spatial pressure. Model 2 was shown to miss some factors, and as a consequence, model 2 did not calculate the same magnitude as Williams' model. If multiplying model 2 with the missing factor however, there were good agreement when comparing with Williams' model, though with model 2 there are some challenges with computational efficiency versus the amount of samples due to model being a three-dimensional description. Model 3 was also compared with Williams' model with a normalization method, and it was seen that they converge towards the same value with increasing distance. There were differences in the nearfield, which may either be due to the fact that model 3 represents particle velocity or that the constant pressure boundary condition is seemingly not a valid boundary condition for the baffled piston model, as Younghouse and Tjotta stated. For model 3, the exclusion of evanescent waves introduced small differences compared to when they were included, it was though bigger differences for low frequencies. Still, the differences at low frequencies between when excluding evanescent waves and including them, were less than compared to model 1. This was due to the inverse normal impedance term, which was not of significant order in the magnitude of angular spectrum for the normal particle velocity, i.e., model 3.

When comparing the three models including plate, they gave very similar results, when using the transfer functions defined in Sec. 2.7., which also agreed with measurements. As the transfer functions are relative, the missing factors of model 2 and 3 does not matter, and because model 3 has the same dynamics as pressure in the farfield, this will give the same results as model 1 and 2. It was also seen with plate transmission, that the exclusion of evanescent waves in model 3 were a valid approach, except for low frequencies.

When introducing a finite receiver it was seen that the Rayleigh-distance is not a good approximation for when the pressure decays as $1/z$. This was due to the wave needing a bigger distance to diverge in order for the wavefront of the wave to become planar over the finite receiver surface. When this happens, the average pressure at the receiver surface becomes equal to the pressure at a point receiver, and they decay equally as $1/z$. When introducing a plate and exciting the S_{-2}-mode of the plate, the maximum pressure at a finite receiver was at a higher frequency compared to the frequency of maximum when using a point receiver. This was due to magnitude of the pressure being slightly higher in the radial direction for a larger frequency, so that the average pressure on the surface of the receiver was higher at this frequency. This effect was also seen when exciting A_3-mode in the plate, which introduced a bigger frequency upshift than that of the point receiver.

Concerning the behavior of the transmitted pressure when increasing the distance between plate and receiver (independent of the receiver being finite or point), it was shown that the frequencies of pressure maximum due to the excitation of the S_{-2}-mode and A_3-mode in the plate, shift toward the cut-off frequencies of the TE modes in the plate with increasing distance from the plate. In the angular spectrum for the S_{-2}-mode, this was due to the unique phase, which was seen to be the determining factor to the value of the spatial pressure, which goes towards the plane-wave component of the spectrum as the distance increases.

7.2 Further work

The program developed for thesis could be used for further investigations when varying other parameters, e.g., the distance between the source and plate, the radius of source or receiver, thickness of plate, Poisson's ratio of the plate, etc. This would contribute to the further investigations needed on the hypothesis of the physical interpretation proposed to why the frequency shift is dependent on distance. This also requires further measurements at longer distances than what is done in the thesis, ideally at approximately 3996.05 mm. A similar investigation of the frequency shift on the pressure due to the excitation of A_3-mode in the plate is necessary. Some further study on the impact of the finite receiver of the transmitted pressure with increasing distance could contribute to this as well. In Sec. 6.2., Fig. 6.14., there was

a minimum of pressure, which for the finite receiver was higher than with the point receiver. This reason, and why there is a dip in the first place, could contribute to a further understanding of the behavior of the transmitted field.

The Scholte-waves and its significance in measurements and in plate transmission should be investigated. Also the understanding of why the surface wave on the lower side of plate is seemingly tens of factors higher in magnitude than the surface wave on upper side, would be very interesting.

Bibliography

[1] H. Lamb, "On the flexure of an elastic plate," *London Mathematical Society*, pp. 70–91, 1889.

[2] H. Lamb, "On waves in an elastic plate," *Proceedings of the Royal Society A: Mathematical, Physical and Engineering Sciences*, vol. 93, no. 648, pp. 114–128, 1917.

[3] L. Rayleigh, "On the free vibrations of an infinite plate of homogeneous isotropic elastic matter," *London Mathematical Society*, pp. 225–234, 1888.

[4] H. Reissner, "Der senkrecthe und schäge durchtritt einer in einem flüssigen medium erzeugten ebenen dilatations welle durch eie in diesem medium befindliche plan-parallelle feste platte," *Helv. Phys. Acta*, vol. 11, pp. 408–431, 1938.

[5] M. F. M. Osborne and S. D. Hart, "Transmission, reflection and guiding of an exponential pulse by a steel plate in water," *The Journal of the Acoustical Society of America*, vol. 17, no. 1, pp. 1–18, 1945.

[6] Z. Su, L. Ye, and Y. Lu, "Guided Lamb waves for identification of damage in composite structures: A review," *Journal of Sound and Vibration*, vol. 295, no. 3, pp. 753–780, 2006.

[7] Y. Bouzidi and D. R. Schmitt, "Quantitative modeling of reflected ultrasonic bounded beams and a new estimate of the Schoch shift," *IEEE transactions on ultrasonics, ferroelectrics, and frequency control*, vol. 55, no. 12, pp. 2661–2673, 2008.

[8] B. Hosten and C. Biateau, "Finite element simulation of the generation and detection by air-coupled transducers of guided waves in viscoelastic and anisotropic materials," *The Journal of the Acoustical Society of America*, vol. 123, no. 4, pp. 1963–1971, 2008.

[9] W. Ke, M. Castaings, and C. Bacon, "3D finite element simulations of an air-coupled ultrasonic NDT system," *Ultrasonics*, vol. 42, no. 6, pp. 524–533, 2009.

[10] M. Masmoudi and M. Castaings, "Three-dimensional hybrid model for predicting air-coupled generation of guided waves in composite material plates," *Ultrasonics*, vol. 52, no. 1, pp. 81–92, 2012.

[11] S. Banerjee, T. Kundu, and N. A. Alnuaimi, "DPSM technique for ultrasonic field modelling near fluid-solid interface," *Ultrasonics*, vol. 46, no. 3, pp. 235–250, 2007.

[12] C. M. Dao, S. Das, S. Banerjee, and T. Kundu, "Wave propagation in a fluid wedge over a solid half-space – mesh-free analysis with experimental verification," *International Journal of Solids and Structures*, vol. 46, no. 11, pp. 2486–2492, 2009.

[13] R. K. Johnson and A. J. Devaney, "Transducer model for a plate thickness measurement," pp. 502–504, IEEE Ultrasonics symposium, U.S.A, San Diego, CA, October 1982.

[14] D. P. Orofino and P. C. Pedersen, "Evaluation of angle-dependent spectral distortion for infinite planar elastic media via angular spectrum decomposition," *The Journal of the Acoustical Society of America*, vol. 93, no. 3, pp. 1235–1248, 1993.

[15] M. J. Anderson and P. R. Martin, "Resonant transmission of a three-dimensional acoustic sound beam through a solid plate in air: theory and measurement," *The Journal of the Acoustical Society of America*, vol. 98, no. 5, pp. 2628–2638, 1995.

[16] S. J. Younghouse, *Irradiation of an elastic plate by a finite-amplitude sound beam with applications to nondestructive evaluation.* PhD thesis, U.S.A., Austin, TX, 2002.

[17] B. J. Landsberger and M. F. Hamilton, "Second-harmonic generation in sound beams reflected from, and transmitted through, immersed elastic solids," *The Journal of the Acoustical Society of America*, vol. 109, no. 2, pp. 488–500, 2001.

[18] K. D. Lohne, P. Lunde, and M. Vestrheim, "Measurements and 3D simulations of ultrasonic directive beam transmission through a water-immersed steel plate," Proceedings of the 34th Scandinavian

symposium on physical acoustics, Geilo, Norway, January/February 2011.

[19] G. Waag, *Air-coupled ultrasound for plate thickness measurements*. PhD thesis, Vestfold, Norway, 2017.

[20] J. Cheng, W. Lin, and Y. Qin, "Extension of the distributed point source method for ultrasonic field modeling," *Ultrasonics*, vol. 51, no. 5, pp. 571–580, 2011.

[21] M. Aanes, *Interaction of piezoelectric transducer excited ultrasonic pulsed beams with a fluid-embedded viscoelastic plate*. PhD thesis, University of Bergen, department of physics and technology, 2014.

[22] S. D. Holland and D. E. Chimenti, "Air-coupled acoustic imaging with zero-group velocity lamb modes," *Applied Physics Letter*, vol. 83, no. 13, pp. 957–960, 2003.

[23] A. Gibson and J. S. Popovics, "Lamb wave basis for impact-echo method analysis," *Journal of Engineering Mechanics*, vol. 131, no. 4, pp. 438–443, 2005.

[24] K. D. Lohne, M. Vestrheim, and P. Lunde, "Ultrasonic signal transmission in plates: Study of steel plate immersed in water," Proceedings of the 31th Scandinavian symposium on physical acoustics, Geilo, Norway, January 2008.

[25] M. Aanes, K. D. Lohne, P. Lunde, and M. Vestrheim, "Transducer beam diffraction effects in sound transmission near leaky lamb modes in elastic plates at normal incidence," pp. 1–4, IEEE Ultrasonics symposium, Taipei, Taiwan, October 2015.

[26] M. Aanes, K. D. Lohne, E. Storheim, P. Lunde, and M. Vestrheim, "Beam transmission of water-embedded steel plate at normal incidence. diffraction effects in the S_1 to A_3 region," Proceedings of the 38th Scandinavian symposium on physical acoustics, Geilo, Norway, February 2011.

[27] M. Aanes, K. D. Lohne, P. Lunde, and M. Vestrheim, "Finite aperture influence on energy concentration, frequency shift, and signal enhancement, for acoustic transmission in the negative group velocity region of the S_1 leaky Lamb mode," pp. 1–4, IEEE Ultrasonics symposium, Tours, France, September 2016.

[28] M. Aanes, K. D. Lohne, P. Lunde, and M. Vestrheim, "Beam diffraction effects in the backward wave regions of viscoelastic

leaky Lamb modes for plate tranmission at normal incidence," *IEEE Transactions on ultrasonics, ferroelectrics, and frequency control*, vol. 64, no. 10, pp. 1558–1572, 2017.

[29] E. V. Glushkov, N. V. Glushkova, and O. A. Miakisheva, "Resonance transmission and backward leaky waves in the coupled system: ultrasound transducer - acoustic fluid - immersed plate," pp. 134–140, Proceedings of the international conference Days on Diffraction 2017, 2017.

[30] L. E. Kinsler, A. R. Frey, A. B. Coppens, and J. V. Sanders, *Fundamentals of Acoustics: Fourth Edition*. U.S.A., Hoboken, NJ: John Wiley and Sons, 2000.

[31] A. H. Meitzler, "Backward-wave transmission of stress pulses in elastic cylinders and plates," *The Journal of the Acoustical Society of America*, no. 5, pp. 835–842, 1965.

[32] P. Lunde, *Selected topics in theoretical acoustics*. Bergen, Norway: University of Bergen, department of physics and technology, 2006.

[33] E. G. Williams, *Fourier Acoustics: Sound radiation and nearfield acoustical holography*. Washington D.C., U.S.A.: Naval Research Laboratory, 1999.

[34] M. Abramowitz and I. A. Stegun, *Handbook of Mathematical functions with formulas, graphs and mathematical tables*. U.S.A.: National Bureau of Standards, 1972.

[35] O. I. Lobkis and D. Chimenti, "Elastic guided waves in plates with surface roughness. II. experiments," *The Journal of the Acoustical Society of America*, vol. 102, no. 1, pp. 150–159, 1997.

[36] E. W. Weisstein, "Inverse sine." `http://mathworld.wolfram.com/InverseSine.html`, 2002.

[37] E. W. Weisstein, "Inverse tangent." `http://mathworld.wolfram.com/InverseTangent.html`, 2002.

[38] J. A. O. Williams, "The piston source at high frequencies," *The Journal of the Acoustical Society of America*, vol. 23, no. 1, pp. 1–6, 1951.

[39] ProofWiki, "Cosine of complex number." `https://proofwiki.org/wiki/Cosine_of_Complex_Number`, 2018.

[40] S. P. Dowson, "Precision acoustics PVDF needle hydrophone serial number 1820," certificate of calibration, National Physics Laboratory.

[41] J. N. Tjotta and S. Tjotta, "Nonlinear equations of acoustics, with application to parametric acoustic arrays," *The Journal of the Acoustical Society of America*, vol. 69, no. 6, pp. 1644–1652, 1981.

[42] J. G. Scholte, "The range of existence of Rayleigh and Stoneley waves," *Geophysical journal international*, vol. 5, no. s5, pp. 120–126, 1947.

[43] J. Sessarego, J. Sagéloli, C. Gazanhes, and H. Überall, "Two Scholte-Stoneley waves on doubly fluid-loaded plates and shells," *The Journal of the Acoustical Society of America*, vol. 101, no. 1, pp. 135–142, 1997.

[44] X. L. Bao, H. Franklin, P. K. Raju, and H. Überall, "The splitting of dispersion curves for plates fluid-loaded on both sides," *The Journal of the Acoustical Society of America*, vol. 102, no. 2, pp. 1246–1248, 1997.

[45] C. Glorieux, K. V. de Rostyne, K. Nelson, W. Gao, W. Lauriks, and J. Thoen, "On the character of acoustic waves at the interface between hard and soft solids and liquids," *The Journal of the Acoustical Society of America*, vol. 110, no. 3, pp. 1299–1306, 2001.

[46] "Waag, personal communication," 2018.

Appendices

Appendix A

Model 1

```
%%Implementation of model 1.
%Declares all constants and vectors,
%before starting the for-loops as
%described in Ch. 3.

%Author: Simen Midtbo, started 20.11.17.

clear;

% %Defining frequency range
f_min  = 350e3;
f_max  = 1000e3;
f_step = 1e3;
f_vector = [f_min:f_step:f_max];

%Medium properties
c_f = 1485;    %speed of sound
rho_f = 1000; %Freshwater density,


%Plate properties
rho_p = 8000; %density of plate
c_s = 3130;%.*(1 - (1i/500)); %transverse
                              %sound in plate
c_l = 5780;%.*(1 - (1i/1000)); %longitudinal ---
%
% %Transducer properties:
a = 10.55e-3; %effective radius of piston
b = 0;        %radius of receiver
```

```
v_0 = 0;

% %Distances and plate thickness
d = 6.05e-3; %thickness of plate
d_t = 270e-3; %sender to upper side of plate
d_r = 100e-3; %lower side of plate to receiver

% %Indexes.
idx = 1;
jdx = 1;
count = 1;

PFront_f = [];
PRec_f = [];

velocity = false; %Calculates velocity if true.
save_ = true;     %Saves if true.
loss = false;     %Includes loss if true.
incevsct = true;  %Includes evanescent waves if
                  %true.

cnt = 1;

%Distance-vector
dtvector = [875e-3];

%Iterates through the distance-vector
for z = dtvector
idx = 1; %Index.
PRec = 0;

%Iterates through the frequency-vector
for f = f_vector

%Set the angular frequency.
w = 2*pi*f;

%Set the fluid-wavenumber.
h_f = w/real(c_f);

%Calculates last maximum.
lambda = (2*pi)/h_f;
last_max = a*((a/lambda) - (lambda/(4*a)));
```

```
%This is to make the choice of N a bit dynamic,
%but N = 512*512 works in general
%for most types of calculations.
if incevsct == true && z > d_t
if f <= 100e3
N = 1024*1024;
else
N = 512*512;
end
elseif incevsct == true && z <= d_t
if f_step == 0.1e3
N = 512*512;
else
N = 512*512;
end
elseif incevsct == false && z <= d_t
N = 512*512;
else
N = 512*512;
end

%Calculates Rayleigh distance.
raydist(idx) = (h_f*a^2)/2;

%Sets the origin of the vectors.
Origo = 1;

%If not including evanescent waves => etamax = h_f.
if incevsct == false
etamax = h_f;
else
etamax = 0;
end

if etamax == 0

%Finds etamax
etamax = FindEtaMax(
last_max,
b, c_f, c_l, c_s, rho_p, d,
d_t, z, h_f, rho_f, w, a, v_0, velocity);
```

```
if z > d_t
%Sets a temporary eta-vector to find temporary
%etaS and
%etaA
etastep = etamax/N;
eta = [0:etastep:etamax - etastep];

%Iterates through the dispersion algorithm 3
%times to enhance accuracy for eta_S, eta_A,
%while simultaneously
%calculating the etavector.
for it = 1:3
[etaA, etaS] = OsbourneHartSholte(eta, w, c_l,
        c_s, rho_p, rho_f, c_f, d, h_f);
eta = FindEta(z, last_max, h_f, eta, etamax,
        etaA, etaS, N);
end
disp('Done with Scholte iterations.')
else
%If z less than d_t, do:
eta = 1; %dummy
etaS = 1;
etaA = 1;

eta = FindEta(z, last_max, h_f, eta, etamax,
        etaA, etaS, N);

end
else
%If excluding evanescent waves do:
etamaxstep = (etamax)/(N);
eta = [0:etamaxstep:etamax - etamaxstep];
etaS = 1;
etaA = 1;
eta = FindEta(z, last_max, h_f, eta, etamax,
                etaA, etaS, N);
end

%If loss = true, calculate the corresponding
%complex h_f
if loss == true
Qf = 0.5e5;
alphaf = 0.5*(h_f./Qf);
```

```
complex_k           = h_f + 1i*alphaf;
alphaflist(jdx)     = imag(complex_k);

else
%This is just to have some dummy values.
alphaflist = 1;
complex_k = h_f;
Qf = 1;
end

disp('Done with nonuniform sampling.')

%Defining the source aperture function
v_0 = 1;
DirHSender = (2.*besselj(1, a.*eta))./(a.*eta);
DirHSender(Origo) = 1;
AmpHSender = v_0*pi*a^2;
HSender = AmpHSender.*DirHSender;

%Defining the receiver aperture function H:
if b == 0
HRec = 1;
else
DirHRec = (2.*besselj(1, b.*eta))./(b.*eta);
DirHRec(Origo) = 1;
AmpHRec = pi*b^2;
HRec = AmpHRec.*DirHRec;
DirHRec = 0;
end

%Calculates the vertical wavenumbe for fluid.
kapf_z = ((complex_k)^2 - eta.^2).^0.5;


%If distance z greater than d_t = calculate
%transmission coefficient.
if z > d_t
T = GetTransmissionCoefficien(complex_k, w,
c_f, c_l, c_s, eta, rho_f, rho_p, d);
disp('Retrieved transmission coefficent.')
else
T = 1;
end
```

```
%Calculating the impedance:
if velocity == true
Zimp  = kapf_z./(rho_f*w);
else
Zimp = (rho_f.*w)./kapf_z;      %impedance
end

%Pressure at the surface of the piston.
PfkAmpl = Zimp.*HSender;

%Calculating the propagation term
PropTerm    = exp(1i.*(kapf_z).*z);

%Calculate the angular spectrums
if z <= d_t
PfkRec = PfkAmpl.*PropTerm;
else
PfkRec = PfkAmpl.*PropTerm...
        .*exp(1i.*(kapf_z).*(-d)).*T;
end


%Integrations.
if b == 0
%Integration if b = 0.
Integrand = PfkRec.*eta;
PrRec = ((1)/(2*pi))*trapz(eta, Integrand);
else
%Integration with finite receiver.
Integrand = PfkRec.*HRec.*eta;
PrRec = (1/(pi*b^2)).*((1)/(2*pi))...
        *trapz(eta, Integrand);
end

disp([20*log10(abs(PrRec)), z*1000, f])

PRec(idx) = PrRec;



idx = idx + 1;
```

```
end


disp([z*1000, f./1000])

PRec_f = [PRec_f PRec'];
%Concatenate values determined within the
%first for-loop. This method
%complex conjugates the complex values, which does
%not matter for magnitude, but for phase.
%Transpose back if phase is of interest.

PFront = [];
jdx = jdx + 1;


PrFrontPlateAvg = 0;
end
```

Appendix B

Model 2

```
%%Implementation of Anderson et. al article
%"Resonant transmission of a
%three-dimensional acoustic sound beam through
%a solid plate in air:
%theory and measurement"
%1995

%Author: Simen Midtbo, started 10.10.17.

%%NB: This program more or less is run exactly as
%model 1. Will only
%%comment the bigger changes.

clear;

% %Defining frequency range and vector
f_min  = 1000e3;
f_max  = 1000e3;
f_step = 1e3;
f_vector = [f_min:f_step:f_max];

%Medium properties
c_f   = 1485; %speed of sound
rho_f = 1000; %Freshwater density

%plate properties
rho_p = 8000; %density of plate
c_s = 3130;%.*(1 - (1i/500)); %transverse
                              %of sound in plate
```

```
c_l = 5780;%.*(1 - (1i/1000)); %longitudinal ---

% %transducer properties:
U_0 = 1; %Particle velocity over the transducer.
a = 10.55e-3; %effective radius of piston
b = a; %radius of receiver: 0 = pointreceiver
%
% %Distance
d = 6.05e-3;        %thickness of plate
d_t = 600e-3;       %sender to upper side of plate
d_r = 100e-3;       %upper side of plate to receiver

% %Indexes.
idx = 1;
jdx = 1;
count = 1;

PFront_f = [];
PRec_f = [];

save_ = true;
loss = false;
incevsct = true;

cnt = 1;

%Setting distance vector
dtvector = [120e-3:1e-3:500e-3];

jdx = 1;
for z = dtvector
idx = 1;

PRec = 0;
for f = f_vector
etamax = 0;
w = 2*pi*f;

k = w/real(c_f);

lambda = (2*pi)/k;
last_max = a*((a/lambda) - (lambda/(4*a)));
```

```
if z < last_max || f < 100e3
N = 1024;
else
N = 1024;
end

U_0 = 1;

raydist(idx) = (k*a^2)/2;

if etamax == 0
%Find etamax
etamax = FindEtaMax(b, c_f,
                                        c_l, c_s,
                                rho_p, d, d_t, z, k,
                                   rho_f, w, a, U_0);

if z > d_t
etamaxstep = (etamax)/(N*1024);
eta = [0:etamaxstep:etamax - etamaxstep];

for it = 1:3
[etaA, etaS] = OsbourneHartSholte_and(eta, w, c_l,
                                    c_s, rho_p, rho_f,
                                          c_f, d, k);
eta = FindEta_and2(k, eta, etamax, etaA, etaS,
                    (N/2));
end

disp('Done with Scholte iterations.')
else
etamaxstep = (etamax)/(N/2);
eta = [0:etamaxstep:etamax - etamaxstep];

etaS = 1;
etaA = 1;

eta = FindEta_and2(k, eta, etamax, etaA, etaS,
                    (N/2));
end
else
etamaxstep = (etamax)/(N/2);
eta = [0:etamaxstep:etamax - etamaxstep];
```

```
etaS = 1;
etaA = 1;
eta = FindEta_and2(k, eta, etamax, etaA, etaS,
                   (N/2));
end

%Setting the one-dimensional horizontal vector
%stretching from 0 to
%etamax
kxOI = eta;

%Flipping the temporary vector
kxOIrev = -fliplr(kxOI);

%Concatenating the flipped and original
kx = [kxOIrev(1:end-1) kxOI];
ky = kx;

%Setting the origin.
if mod(length(kx), 2) == 0
Origo = (length(kx)/2) + 1;
else
Origo = ceil(length(kx)/2);
end

%Creating matrices
[k_X, k_Y] = meshgrid(kx, -ky);

%Declaring the two-dimensional eta for further
%implementation
eta = (k_X.^2 + k_Y.^2).^0.5;
k_X = 0;
k_Y = 0;

if loss == true
Qf = 0.5e5;
alphaf = 0.5*(k./Qf);
complex_k          = k + 1i*alphaf;
alphaflist(idx)    = imag(complex_k);

else
alphaflist = 1;
complex_k = k;
```

```
Qf = 0;
end

disp('Done with nonuniform sampling.')

%Defining aperture function
DirHSender = (besselj(1, a.*eta))./(a.*eta);
DirHSender(Origo, Origo) = 0.5;
AmpHSender = U_0*pi*a^2;
Hsender = AmpHSender.*DirHSender;
DirHSender = 0;

%defining the aperture funcction H:
if b == 0
HRec = 1;
else
DirHRec = (besselj(1, b.*eta))./(b.*eta);
DirHRec(Origo, Origo) = 0.5;
AmpHRec = pi*b^2;
HRec = AmpHRec.*DirHRec;
DirHRec = 0;
end

kapf_z = ((complex_k)^2 - eta.^2).^0.5;


if z > d_t
T = GetTransmissionCoefficien_and(complex_k,
                                  w, c_f,
                          c_l, c_s, eta, rho_f,
                                  rho_p, d);
disp('Retrieved transmission coefficent.')
else
T = 1;
end



%finding the pressure in f-k domain:

Zimp = (rho_f.*w)./kapf_z;      %impedance
```

```
PfkAmpl = Zimp.*Hsender;   %pressure
Zimp = 0;
Hsender = 0;

%Propagating factors:

PropTerm    = exp(1i.*(kapf_z).*z);

%%%The integrands
if z <= d_t
Pfk     = PfkAmpl.*PropToPlate;
PfkRec = Pfk.*HRec;
else
PfkFront = PfkAmpl.*HRec.*PropTerm...
                .*exp(1i.*(kapf_z).*(-d));
PfkRec = PfkAmpl.*HRec.*PropTerm...
                .*exp(1i.*(kapf_z).*(-d)).*T;
end

PfkAmpl = 0;
PropTerm = 0;
HRec = 0;
kapf_z = 0;
T = 0;
Pfk = 0;
PfkFront = 0;

%%%Doing the two-dimensional discrete integration.
if b == 0
PrRec = ((1)/(4*pi^2))...
        *trapz(ky, trapz(kx, PfkRec, 2));
else
PrRec = ((1)/(4*pi^2))...
        *trapz(ky, trapz(kx, PfkRec, 2));
end

PfkRec = 0;

PRec(idx) = PrRec;

disp([z*1000, f./1000])

idx = idx + 1;
```

```
end


disp(z*1000)

PRec_f    = [PRec_f PRec'];

jdx = jdx + 1;


PrFrontPlateAvg = 0;
end
```

Appendix C

Model 3

```
%Implementation of Orofino/Pedersen article:
%Evaluation of angle-dependent
%spectral distortion for infinite planar elastic
%media via angular
%spectrum decomposition
%1993
%Author: Simen Midtbo, started 10.17.

%%NB: This program more or less is run exactly as
%model 1. Will only
%%comment the bigger changes.

clear;

N = 4096*4096;
f_vector = [1e3:1e3:1e3];

%Medium properties
c_f = 1485; %speed of sound
rho_f = 1000; %Freshwater density

%transducer properties:
a = 10.55e-3; %effective radius of piston
b = a;

%plate properties:
d = 6.05e-3; %thickness
rho_p = 8000; %density of plate
c_s = 3130; %transverse of sound in plate
```

```
c_l = 5780; %longitudinal --"---

%Distance
d_t = 501e-3;      %sender to upper side of plate
d_r = 100e-3;  %upper side of plate to receiver

%dtvector = [0:0.1e-3:100e-3];

%Indexes.
idx = 1;
jdx = 1;

UFront = [];
URec = [];

UFront_f = [];
URec_f = [];

t = 140e-6;

dtvector = [d_t + d_r + d];

save_ = false;
incl_evsct = true;
loss = true;

for f = f_vector
idx = 1;
disp(f)
for z = dtvector
disp(idx)
w = 2*pi*f;

Origo = 1;

k = w/c_f;

if incl_evsct == true;

etamax = FindEtaMax(b, c_f,
                                          c_l, c_s,
                                          rho_p, d,
                    d_t, z, k, rho_f, w, a, U_0);
```

```
if z > d_t

etamaxstep = (etamax)/(N);
eta = [0:etamaxstep:etamax - etamaxstep];

for it = 1:3
[etaA, etaS] = OsbourneHartSholte(eta, w, c_l,
                c_s, rho_p, rho_f, c_f, d, k);
eta = FindEta(k, eta, etamax, etaA, etaS, N);
end

disp('Done with Scholte iterations.')
else
etamaxstep = (etamax)/(N);
eta = [0:etamaxstep:etamax - etamaxstep];

etaS = 1;
etaA = 1;

eta = FindEta(k, eta, etamax, etaA, etaS, N);

end

%
else
etamax = k;
etamaxstep = k/N;
eta = [0:etamaxstep:etamax - etamaxstep];
etaS = 1;
etaA = 1;
eta = FindEta(k, eta, etamax, etaA, etaS, N);
end

thetaz = asin(eta./k);

if loss == true
Qf = 0.5e5;
alphaf = 0.5*(k./Qf);              %Qf = 0.5e5
complex_k          = k + 1i*alphaf;
alphaflist(idx)    = imag(complex_k);

else
```

```
alphaflist = 1;
complex_k = k;
Qf = 0;
end


%defining the aperture function H for the sender:
DirHTrans = (2.*besselj(1, a.*eta))./(a.*eta);
DirHTrans(1) = 1;
HTrans = DirHTrans;

DirHRec = (2.*besselj(1, b.*eta))./(b.*eta);
DirHRec(1) = 1;
HRec = DirHRec;

if z > d_t

%Defining the transmission coefficient
%for the plate:
k_z = (complex_k.^2 - eta.^2).^0.5;

kapf_z = (complex_k^2 - eta.^2).^0.5;
kapl_z = ((w/c_l)^2 - eta.^2).^0.5;
kaps_z = ((w/c_s)^2 - eta.^2).^0.5;

A = ((w./c_s).^2 - 2*(eta).^2).^2....
        .*tan(kapl_z.*(d./2))...
        + 4.*(w./c).^2.*kaps_z.*kapl_z...
        .*tan(kaps_z.*(d./2));

S = ((w./c_s).^2 - 2*(eta).^2).^2....
        .*cot(kapl_z.*(d./2))...
        + 4.*(eta).^2.*kaps_z.*kapl_z...
        .*cot(kaps_z.*(d./2));

Y = (rho_f./rho_p).*(kapl_z./kapf_z).*(w./c_s).^4;

T = (1i.*Y.*(S +d_t +  A))./((S - 1i.*Y)....
        .*(A + 1i.*Y));

R = (A.*S - Y.^2)./((S - 1i.*Y).*(A + 1i.*Y));

T(isnan(T)) = 0;
```

```
R(isnan(R)) = 0;
else
kapf_z = (complex_k^2 - eta.^2).^0.5;
T = 1;
end

ZimpInv = ((cos(thetaz))./(rho_f.*c_f));
UfkAmpl = ZimpInv.*HTrans;

%Propagating factors:
PropToPlate = exp(1i.*complex_k.*cos(thetaz).*z);

if z > d_t
PropTerm = exp(1i.*complex_k.*cos(thetaz)....
                .*(z - d));
end

%Integrating
if z <= d_t
Ufk = UfkAmpl.*PropToPlate;
Integrand = Ufk.*HRec.*complex_k.*sin(thetaz)...
.*complex_k.*cos(thetaz);
UrFrontPlateAvg = 2*pi*trapz(thetaz, Integrand);
UFront(idx) = UrFrontPlateAvg;
else
Ufk = UfkAmpl.*T.*PropTerm;
Integrand = Ufk.*HRec.*complex_k.*sin(thetaz)...
.*complex_k.*cos(thetaz);
UrRecAvg = 2*pi*trapz(thetaz, Integrand);
URec(idx) = UrRecAvg;
end

disp(20*log10(abs(URec(idx))))
idx = idx + 1;
end

jdx = jdx + 1;
if z <= d_t
UFront_f = [UFront_f UFront'];
else
URec_f = [URec_f URec'];
end
```

end

Appendix D

FindEtaMax

```
function etamax = FindEtaMax(last_max, b, c_f,
c_l, c_s, rho_p, d, d_t, z, k, rho_f, w, a,
U_0, velocity);

%If z = 0, the pressure will decay to slow,
%so the etamax will be huge.
%Etamax at z = 0 was therefore empirically
%determined instead, which gives
%decent values in general. Could perhaps be
%more accurate determined.
if z == 0
etamax = 10^4;
return
end

%Declares the "infinite" etamax, which is
%temporary.
InfEta = 20e3;
etamax = 0;

%Some values to use in search of etamax.
Origo = 1;
found = false;
start = k;
count = 1;

%%%%Find dB-threshold.
while found == false
if count == 1
```

```
%This is just in case the velocity
%is true. As stated in Ch. 3,
%the threshold for the velocity is a
%difference. This finds the
%value to compare so that the
%difference is bigger than 200 dB.
etatemp = [0:1:k-10e-6];
kz_temp = (k.^2 - etatemp.^2).^0.5;
else
%Finds the temporary eta-vector and
%temporary vertical
%wavenumber for the evanescent part.
etatemp = [start:1:InfEta];
kz_temp = 1j.*(etatemp.^2 - k.^2).^0.5;
end

%Gets transmission coefficient in case
%this is transmission.
if z > d_t
T = GetTransmissionCoefficien(k, w,
c_f, c_l, c_s, etatemp, rho_f, rho_p, d);
else
T = 1;
end

%Calculates the propagating term,
%or evanescent term.
expfunc = exp(1j.*kz_temp.*z);

%Calculates the impedance term,
%depending on if it's particle
%velocity or pressure.
if velocity == true
zterm = kz_temp./(rho_f.*w);
else
zterm = (rho_f*w)./kz_temp;
end

%defining the source aperture function:
DirHSender = (2.*besselj(1, a.*etatemp))...
./(a.*etatemp); %Directivity
DirHSender(Origo) = 1;
AmpHSender = U_0*pi*a^2;
```

```
HSender = AmpHSender.*DirHSender;

%Calculates the spectrum depending if
%it's transmission or not.
if z <= d_t
avgPfk = zterm.*HSender.*expfunc;
else
avgPfk = zterm.*T.*HSender.*expfunc....
.*exp(1j.*kz_temp.*(-d));
end

%Finds the Decibel values of the calculated vector.
avgPfk_log = 20*log10(abs(avgPfk));

%Sets the comparing-value to use for velocity.
if count == 1
compValue = max(avgPfk_log);
count = count + 1;
else
%Just to ensure that the values checked
%are bigger than h_f.
%This may though not be necessary, but
%haven't changed it at
%the present time.
indexstart = find(etatemp > start);
indexstart = indexstart(1);

%Iterates through the calculated Decibel values.
for i = indexstart:length(avgPfk_log)
if velocity == true
%Checks to find a difference bigger than 200 dB.
if abs(avgPfk_log(i)) - abs(compValue) > 200

%Sets etamax and breaks.
etamax = etatemp(i);
found = true;
break
end
else

%Finds when the pressure spectrum is below 200 dB.
if abs(avgPfk_log(i)) > 200
etamax = etatemp(i);
```

```
found = true;
break
end
end
end

%If etamax not found, increase infeta and
%repeat process. This
%may not be necessary but is just a precaution.
if etamax == 0
start = InfEta;
InfEta = InfEta + 20e4;
end
end
end
```

Appendix E

FindEta

```
%This is the non-uniform sampling method as
%described Ch. 3.
%Author: Simen Midtbo
function eta = FindEta(z, last_max, k, eta,
                       etamax, etaA, etaS, N)

%If etaA = 1 and etaS = 1 => no transmission.
if etaA == 1 && etaS == 1

%If excluding evanescent waves, do
if etamax == k
hfmin = k - (k/N);
hfmax = k;
hfstep = (hfmax - hfmin)/(N);
etahf = [hfmin:hfstep:hfmax - hfstep];

etapropmax = hfmin;
etapropmin = 0;
etapropstep = (etapropmax - etapropmin)/(N);
etaprop = [etapropmin:etapropstep:
        etapropmax - etapropstep];

eta = [etaprop etahf];
else
%If including evanescent waves
%without transmission:
hfmin = k - (k/N);
hfmax = k + (k/(N - 1));
hfstep = (hfmax - hfmin)/(N);
```

```
etahf = [hfmin:hfstep:hfmax - hfstep];

etapropmax = hfmin;
etapropmin = 0;
etapropstep = (etapropmax - etapropmin)/(N);
etaprop     = [etapropmin:etapropstep:
                etapropmax - etapropstep];

etaevsctmax = etamax;
etaevsctmin = hfmax;

%This is just to enhance the resolution if in
%nearfield. May not be
%important, but just a failsafe.
if z < last_max
etaevsctstep = (etaevsctmax - etaevsctmin)/(2*N);
etaevsct = [etaevsctmin:etaevsctstep:
                etamax - etaevsctstep];
else
etaevsctstep = (etaevsctmax - etaevsctmin)/(N);
etaevsct = [etaevsctmin:etaevsctstep:
                etamax - etaevsctstep];
end

%Concatenate the eta-vectors.
eta = [etaprop etahf etaevsct];

end


elseif etaA - etaS > 0.5
%For low frequencies.
hfmin = k - (k/N);
hfmax = etaS + (etaS/(N - 1));
hfstep = (hfmax - hfmin)/(2*N);
etahf = [hfmin:hfstep:hfmax - hfstep];

etapropmax = hfmin;
etapropmin = 0;
etapropstep = (etapropmax - etapropmin)/(N);
etaprop     = [etapropmin:etapropstep:
                etapropmax - etapropstep];
```

```
etaAmin = hfmax;
etaAmax = etaA + etaA/N;
etaAstep = (etaAmax - etaAmin)/N;
etaA = [etaAmin:etaAstep:etaAmax - etaAstep];

%samples the space between the two scholte waves
etahfSpaceAmin = hfmax;
etahfSpaceAmax = etaAmin;
etahfSpaceA     = [etahfSpaceAmin:etapropstep:etahfSpaceAmax - etaprop

etaevsctmax = etamax;
etaevsctmin = etaAmin;

if z < last_max
etaevsctstep = (etaevsctmax - etaevsctmin)/(2*N);
etaevsct = [etaevsctmin:etaevsctstep:
                etamax - etaevsctstep];

else
etaevsctstep = (etaevsctmax - etaevsctmin)/(N);
etaevsct = [etaevsctmin:etaevsctstep:
                etamax - etaevsctstep];
end

%Concatenate the eta-vectors.
eta = [etaprop etahf etaA etaevsct];

else
%For higher frequencies.
hfmin = k - (k/N);
hfmax = etaA + (etaA/(N - 1));
hfstep = (hfmax - hfmin)/(2*N);
etahf = [hfmin:hfstep:hfmax - hfstep];

etapropmax = hfmin;
etapropmin = 0;
etapropstep = (etapropmax - etapropmin)/(N);
etaprop     = [etapropmin:etapropstep:
                etapropmax - etapropstep];

etaevsctmax = etamax;
etaevsctmin = hfmax;
```

```
if z < last_max
etaevsctstep = (etaevsctmax - etaevsctmin)/(2*N);
etaevsct = [etaevsctmin:etaevsctstep:
                etamax - etaevsctstep];
else
etaevsctstep = (etaevsctmax - etaevsctmin)/(N);
etaevsct = [etaevsctmin:etaevsctstep:
                etamax - etaevsctstep];
end

%Concatenate the eta-vectors
eta = [etaprop etahf etaevsct];

end
```

Appendix F

GetTransmissionCoefficien

```
%Calculates the transmission coefficient.
%Input: All parameters to calculate transmission
%coefficient.
%Output: Transmission Coefficient
%Author: Simen Midtbo

function [T] = GetTransmissionCoefficien(k, w,
                c_f, c_l, c_s, eta, rho_f, rho_p, d)
kapf_z = ((k)^2 - eta.^2).^0.5;
kapl_z = ((w/c_l)^2 - eta.^2).^0.5;
kaps_z = ((w/c_s)^2 - eta.^2).^0.5;

%Defining the tan and cotan terms of the
%transmission coefficient as
%defined in Ch. 2.
tan_1 = sin(kapl_z.*(d./2))./cos(kapl_z.*(d./2));
tan_2 = sin(kaps_z.*(d./2))./cos(kaps_z.*(d./2));
cotan_1 = 1./tan_1;
cotan_2 = 1./tan_2;

%The antisymmetric term.
A = ((w./c_s).^2 - 2.*(eta).^2).^2.*tan_1...
        + 4.*(eta).^2.*kaps_z.*kapl_z.*tan_2;

%The symmetric term
S = ((w./c_s).^2 - 2.*(eta).^2).^2.*cotan_1...
       + 4.*(eta).^2.*kaps_z.*kapl_z.*cotan_2;

%This is just to not have any lingering unused
```

```
%vectors.
tan_1 = 0;
tan_2 = 0;
cotan_1 = 0;
cotan_2 = 0;

%The Y term.
Y = (rho_f./rho_p).*(kapl_z./kapf_z).*(w./c_s).^4;

%Again not to have any unused vectors lingering.
kapf_z = 0;
kapl_z = 0;
kaps_z = 0;

%The numerator of the transmission coefficient.
num = (1i.*Y.*(S + A));

%The denominator of the transmission coefficient.
den = ((S - 1i.*Y).*(A + 1i.*Y));

T = num./den;

dummyNaN = isnan(T); %To make sure that values are
                     %zero and not nan.

T(dummyNaN) = 0;
```

Appendix G

OsbourneHartScholte

```
%This routine finds the antisymmetrical and
%symmetrical Scholte-wave wavenumber by use of
%Osbourne and Harts equations given in Ch. 2.
%Input: All the required parameters do calculate
%Osbourne and Harts equations
%Output: EtaA and etaS
%Author: Simen Midtbo

function [etaA, etaS] = OsbourneHartSholte(eta,
        w, c_l, c_s, rho_p, rho_f, c_f, d, h_f);

%Declaring all relevant variables.
cp = w./eta;
c_d = c_l;
c_r = c_s;
rho_s = rho_p;
rho_w = rho_f;
c_w = c_f;

%Following Osbourne and Hart equation with
%f = half the thickness of plate.
f = d/2;

%Ensuring that minimum found is bigger than h_f
etasmin_index = find(eta > h_f);

%Because the equations decay with eta, this is
%to ensure that the minimum is within h_f + 0.1
etasmax_index = find(eta > h_f + 0.1);
```

```
%If eta does not have an element greater than
%h_f + 0.1, the endindex is
%simply the length of eta.
if isempty(etasmax_index) == true
    etasmax_index = length(eta);
end

%Setting up the eta to calculate the
%symmetrical equation.
etas     = eta(etasmin_index(1):etasmax_index(1));
%Setting up the phase velocity to calculate the
%symmetrical equation.
cps      = w./etas;

%Declaring terms of Osbourne and Harts equation
%given in Ch. 2.
%Symmetrical:
term1 = (1 - 0.5*(cps./c_r).^2).^2;
term2 = coth(etas.*f.*(1 - (cps./c_d).^2).^0.5);
term3 = (1 - (cps./c_d).^2).^0.5...
        .*(1 - (cps./c_r).^2).^0.5;
term4 = coth(etas.*f.*(1 - (cps./c_r).^2).^0.5);
term5 = (rho_w/rho_s).*(c_w./c_r).^2;
term6 = 1./(1 - (cps./c_w).^2).^0.5;
term7 = (cps.^4./(c_w.^2.*c_r.^2));
term8 = (1 - (cps./c_d).^2).^0.5;

S = 4.*(term1.*term2 - term3.*term4)...
        + term5.*term6.*term7.*term8;

%Antisymmetrical
term1 = (1 - 0.5*(cp./c_r).^2).^2;
term2 = tanh(eta.*f.*(1 - (cp./c_d).^2).^0.5);
term3 = (1 - (cp./c_d).^2).^0.5...
        .*(1 - (cp./c_r).^2).^0.5;
term4 = tanh(eta.*f.*(1 - (cp./c_r).^2).^0.5);
term5 = (rho_w/rho_s).*(c_w./c_r).^2;
term6 = 1./(1 - (cp./c_w).^2).^0.5;
term7 = (cp.^4./(c_w.^2.*c_r.^2));
term8 = (1 - (cp./c_d).^2).^0.5;

A = 4.*(term1.*term2 - term3.*term4)...
```

```
        + term5.*term6.*term7.*term8;

%Finds the minimum of the symmetrical equation.
index_S = find(20*log10(abs(S))...
          == min(20*log10(abs(S))));

%Finds the minimum of the antisymmetrical equation.
index_A =  find(20*log10(abs(A))...
          == min(20*log10(abs(A))));

%Declaring etaS and etaA
etaS = etas(index_S);
etaA = eta(index_A);

%Sometimes the accuracy is big, so find(min) etc.
%finds many minimum values equal
%to one another.
if length(etaA) > 1
    etaA = etaA(1);
end

if length(etaS) > 1
    etaS = etaS(1);
end
```

Appendix H

Spatial Distribution

```
%The spatial distribution calculation, using
%model 1.
%This is very similar to the program model 1,
%so only major steps will be
%commented.

%Author: Simen Midtbo, started 15.2.18.

clear;

% %Defining frequency range
f_min  = 458e3;
f_max  = 458e3;
f_step = 1e3;
f_vector = [f_min:f_step:f_max];

%Medium properties
c_f = 1485;   %speed of sound
rho_f = 1000; %Freshwater density


%Plate properties
rho_p = 8000; %density of plate
c_s = 3130;
c_l = 5780;
%
% %Transducer properties:
a = 10.55e-3; %effective radius of piston
```

```
b = 0;          %radius of receiver
v_0 = 0;

% %Distances and plate thickness
d = 6.05e-3; %thickness of plate
d_t = 270e-3; %sender to upper side of plate
d_r = 100e-3; %lower side of plate to receiver

% %Indexes.
idx = 1;
jdx = 1;
count = 1;

%Declares the empty vector to store pressure
%svalues in.
pr = [];

velocity = false; %Calculates velocity if true.
save_ = false;     %Saves if true.
loss = false;      %Includes loss if true.
incevsct = true;  %Includes evanescent waves if
%true.

cnt = 1;

%Distance-vector
dtvector = [276.05e-3];

%Iterates through the distance-vector
for z = dtvector
idx = 1; %Index.
PRec = 0;

%Iterates through the frequency-vector
for f = f_vector

%Set the angular frequency.
w = 2*pi*f;

%Set the fluid-wavenumber.
h_f = w/real(c_f);

%Calculates last maximum.
```

```
lambda = (2*pi)/h_f;
last_max = a*((a/lambda) - (lambda/(4*a)));

%This is to make the choice of N a bit dynamic,
%but N = 512*512
%works in general for most types of calculations.
if incevsct == true && z > d_t
if f <= 100e3
N = 1024*1024;
else
N = 512*512;
end
elseif incevsct == true && z <= d_t
if f_step == 0.1e3
N = 512*512;
else
N = 512*512;
end
elseif incevsct == false && z <= d_t
N = 512*512;
else
N = 512*512;
end

%Calculates Rayleigh distance.
raydist(idx) = (h_f*a^2)/2;

%Sets the origin of the vectors.
Origo = 1;

%If not including evanescent waves =>
%etamax = h_f.
if incevsct == false
etamax = h_f;
else
etamax = 0;
end

if etamax == 0

%Finds etamax
etamax = FindEtaMax(last_max, b, c_f, c_l, c_s,
rho_p, d, d_t, z, h_f, rho_f,
```

```
w, a, v_0, velocity);

if z > d_t
%Sets a temporary eta-vector to find temporary
%etaS and
%etaA
etastep = etamax/N;
eta = [0:etastep:etamax - etastep];

%Iterates through the dispersion algorithm 3
%times to
%enhance accuracy for eta_S, eta_A,
%while simultaneously
%calculating the etavector.
for it = 1:3
[etaA, etaS] = OsbourneHartSholte(eta, w, c_l,
c_s, rho_p, rho_f, c_f, d, h_f);
eta = FindEta(z, last_max, h_f, eta, etamax,
etaA, etaS, N);
end
disp('Done with Scholte iterations.')
else
%If z less than d_t, do:
eta = 1; %dummy
etaS = 1;
etaA = 1;

eta = FindEta(z, last_max, h_f, eta, etamax,
etaA, etaS, N);

end
else
%If excluding evanescent waves do:
etamaxstep = (etamax)/(N);
eta = [0:etamaxstep:etamax - etamaxstep];
etaS = 1;
etaA = 1;
eta = FindEta(z, last_max, h_f, eta, etamax,
etaA, etaS, N);
end

%If loss = true, calculate the corresponding
%complex h_f
```

```
if loss == true
Qf = 0.5e5;
alphaf = 0.5*(h_f./Qf);
complex_k           = h_f + 1i*alphaf;
alphaflist(jdx)     = imag(complex_k);

else
%Just to have some dummy values.
alphaflist = 1;
complex_k = h_f;
Qf = 1;
end

disp('Done with nonuniform sampling.')

%Defining the source aperture function
v_0 = 1;
DirHSender = (2.*besselj(1, a.*eta))./(a.*eta);
DirHSender(Origo) = 1;
AmpHSender = v_0*pi*a^2;
HSender = AmpHSender.*DirHSender;

%Calculates the vertical wavenumbe for fluid.
kapf_z = ((complex_k)^2 - eta.^2).^0.5;

%If distance z greater than d_t
%= calculate transmission coefficient.
if z > d_t
T = GetTransmissionCoefficien(complex_k, w, c_f,
        c_l, c_s, eta, rho_f, rho_p, d);
disp('Retrieved transmission coefficent.')
else
T = 1;
end

%Calculating the impedance:
if velocity == true
Zimp  = kapf_z./(rho_f*w);
else
Zimp = (rho_f.*w)./kapf_z;     %impedance
end

%Pressure at the surface of the piston.
```

```
PfkAmpl = Zimp.*HSender;

%Calculating the propagation term
PropTerm    = exp(1i.*(kapf_z).*z);

%Calculates the spectrums.
if z <= d_t
PfkASM = PfkAmpl.*PropTerm;
else
PfkASM = PfkAmpl.*PropTerm...
.*exp(1i.*(kapf_z).*(-d)).*T;
end

%%%Finding the spatial distribution of pressure.
[pr_i, r]              = FourierBessel(PfkASM, eta);
pr_i = (1/(2*pi)).*pr_i;
pr = [pr pr_i'];
disp([idx, f])

idx = idx + 1;

end

disp([z*1000, f./1000])
jdx = jdx + 1;


PrFrontPlateAvg = 0;
end
```

Appendix I

FourierBessel

```
%Runs a FourierBessel transformation
%(HankelTransform)
%Author: Simen Midtbo
function [pr, r] = FourierBessel(PfkASM, eta)

%Defines the radial direction vector
r = [0e-3:1e-3:20e-3];

pr = PfkASM(1:length(r));
for i = 1:length(r)
disp([num2str(i), '  FourierBessel'])

%Sets up the integrand per. r-value
integrand = PfkASM...
.*besselj(0, (r(i).*eta)).*eta;

%Integrates per. r-value to get the spatial
%pressure.
pr(i) = trapz(eta, integrand);
end
```